Performance, Analysis and Implementation of Broadband Analog Fiber-Optic link for GMRT

SOMAK BHATTACHARYYA
Third Semester, M.Tech,
Institute of Radiophysics & Electronics.
University of Calcutta, Kolkata-700009,
West Bengal.
E-mail: somak31@ieee.org

Under the guidances of:

Dr. Ashik Paul (Internal Guide)
Lecturer, Institute of Radiophysics And Electronics.
University of Calcutta, Kolkata-700009, West Bengal.
E-mail: ashik_paul@rediffmail.com

Mr. S.Sureshkumar (External Guide)
Engineer-E, Fiber Optics Group
Giant Meterwave Radio Telescope (GMRT)
National Centre for Radio Astrophysics (NCRA)
Tata Institute of Fundamental Research (TIFR)
Post Bag No. 6, Narayangoan, Tal - Junnar,
Dist – Pune, State – Maharashtra, Pin - 410 504.
Phone: +91-2132-252113/6/7, Fax: +91-2132-252120.
E-mail: skumar.tifr@gmail.com

ACKNOWLEDGEMENT

The entire project had been a learning process and it would have been difficult for me without the guidance of my Project Guides Mr. S.Sureshkumar & Dr. Ashik Paul. Their cordial mannerisms and incessant support served as a great boost all the time.

I would like to thank Dr. Yashwant Gupta, the Chief Scientist of GMRT, NCRA, TIFR for his care and my thanks also to Dr. Rajaram Nityananda, the Director, GMRT, NCRA, TIFR for the belief that he had shown upon me and making all the necessary accommodations for me to stay at GMRT & NCRA. I want to thank Mr. T.L.Venkatsubramani when I was at GMRT during 2007 October since he made the systems of GMRT to clarify to me. I want to record my thanks to Mr. Alexander Praveenkumar, the group co-coordinator of the RF and Fiber-Optic Group.

I like to thank Mr. Suresh Sabhapathy, who has guided me whenever I have faced in any difficulty throughout the project. I also like to thank Dr. Sabyasachi Pal, Visiting Fellow of NCRA, who explained me the basic physics behind my project work. I wish to thank the members of the fiber-optic lab, Mr. M.Gopinathan, Mr. S.K.Lokhande, Mr. Pravin Raybole, Mr. Amit Sawant, Miss Dipali Atkari and Mr. Milind Thorat, who have helped me a lot in the lab. Dr. Shubhendu Joardar helped me a lot regarding my study about MATLAB programming. Also, I like to thank the STP students, Mr. Mukesh Bhongade, Miss Pallavi Roychoudhary, Mr. Pranjal Borah, Mr. Manish Kumar, Mr. Ram Krishna, Mr. Avinaba Dutta and Mr. Soumava Mukherjee for helping me regarding a number of aspects. Also, Mr. Naresh Sisodiya, Mr. Hanumanth Rao Bandari, Mr. Satpal Gole, Mr. Mahadeb Mishal and Mr. Vishal Temkar helped me whenever I require them. The persons in GMRT Control room, Mr. Sachin Sherkar, Mr. Sanjay Kudale, Mr. Nilesh Ruskar, Mr. Jitendra Kopikar, Mr. Rupsing Vasave and Miss Shilpa Dubal have helped me while taking the images at different frequency band is GMRT.

I am thankful to Mr. Popat Dhomne, Mr. Ganesh Thorat, Mr. Gulab Chavan, Mr. Milind Thorat and Mr. Nachiket Thorat in GMRT, while making my stay at GMRT joyful. Also, my thanks will go to Mr. J.K.Solanki, to make my stay cheerful. Mr. Sanjay Dungre at Library helped me a lot in the library. I thank all the staffs of GMRT and NCRA.

While I have worked in the Institute of Radiophysics & Electronics, I want to record my thanks to Prof. Asish Kumar Dasgupta, Mrs. Sarbani Pal, Mrs. Aditi Da, Mr. Anup Kumar Bose and Mr. Tanmoy Das for providing me the help whenever I have faced any sort of difficulty. Also, Mr. Dhruba Jyoti Bhaumick helped me in the laboratory whenever I am in trouble.

Last, but not the least, I am indebted to my family members for providing me the option to carry out my project at GMRT, Khodad.

DATE: 25 AUGUST, 2008

(SOMAK BHATTACHARYYA)

CONTENTS

Chapter 1

An Introduction To Radio Astronomy

1.1. An Introduction to Radio waves:

Radio waves are electromagnetic waves occurring on the radio frequency portion of the electromagnetic spectrum. A common use of the radio wave is to transport information through the atmosphere or outer space without wires. Radio waves are distinguished from other kinds of electromagnetic waves by their relatively long wavelength in the electromagnetic spectrum.

Radio waves were first predicted by mathematical work done in 1865 by James Clerk Maxwell. Maxwell noticed wave-like properties of light and similarities in electrical and magnetic observations and proposed equations that described light waves and radio waves as waves of electromagnetism that travel in space. In 1887 Heinrich Hertz demonstrated the reality of Maxwell's electromagnetic waves by experimentally generating radio waves in his laboratory. Many inventions followed, making practical use of radio waves to transfer information through space. The communications using radio waves were first demonstrated independently by Sir J.C.Bose and Guglielmo Marconi respectively.

In free space, all electromagnetic waves (radio, light, X-rays, etc) obey the inverse-square law which states that the power density of an electromagnetic wave is proportional to the inverse of the square of *r* (where *r* is the distance [radius] from the source) or:

$$\rho_P \propto \frac{1}{r^2} \tag{1.1}$$

Doubling the distance from a transmitter means that the power density of the radiated wave at that new location is reduced to one-quarter of its previous value.

The far-field magnitudes of the electric and magnetic field components of electromagnetic radiation are equal, and their field strengths are inversely proportional to distance. The power density per surface unit is proportional to the product of the two field strengths, which are expressed in linear units. Thus, doubling the propagation path distance from the transmitter reduces their received field strengths over a free-space path by one-half.

Electromagnetic wave propagation is also affected by several other factors determined by its path from point to point. This path can be a direct line of sight path or an over-the-horizon path aided by refraction in the ionosphere. Factors influencing ionospheric radio signal propagation can include sporadic-E, spread-F, solar flares, geomagnetic storms, ionospheric layer tilts, and solar proton events.

Lower frequencies (between 30 and 3,000 kHz) have the property of following the curvature of the earth via groundwave propagation in the majority of occurrences. The interaction of radio waves with the ionized regions of the atmosphere makes radio propagation more complex to predict and analyse than in free space (see image at right). Ionospheric radio propagation has a strong connection to space weather.

Since radio propagation is somewhat unpredictable, such services as emergency locator transmitters, in-flight communication with ocean-crossing aircraft, and some television broadcasting have been moved to satellite transmitters. A satellite link, though expensive, can offer highly predictable and stable line of sight coverage of a given area.

A sudden ionospheric disturbance or shortwave fadeout is observed when the x-rays associated with a solar flare ionize the ionospheric D-region. Enhanced ionization in that region increases the absorption of radio signals passing through it. During the strongest solar x-ray flares, complete absorption of virtually all ionospheric propagated radio signals in the sunlit hemisphere can occur. These solar flares can disrupt HF radio propagation and affect GPS accuracy. Table 1.1 describes the different types of Radio waves and their applications.

Table 1.1

Frequency Domain	Range (Hz)	Applications
Extremely Low Frequency (ELF)	3-30	Audio Frequency, Submarine Communications
Super Low Frequency (SLF)	30-300	Audio Frequency, AC Power Grids
Ultra Low Frequency (ULF)	300-3000	Audio Frequency, Mine Communications
Very Low Frequency (VLF)	3K - 30K	Audio Frequency, Long Distance Communications
Low Frequency (LF)	30K - 300K	Navigation, International Broadcasting
Medium Frequency (MF)	300K - 3000K	AM Radio Broadcasting, Maritime Communications
High Frequency (HF)	3M - 30M	Walkie-Talkie, Shortwave Communications
Very High Frequency (VHF)	30M - 300M	FM Broadcasting, TV Broadcasting
Ultra High Frequency (UHF)	300M - 3000M	Radar Communications, Mobile Communications
Super High Frequency (SHF)	3G - 30G	Microwave Links, Satellite Links
Extremely High Frequency (EHF)	30G - 300G	Radio Astronomy, Defence Radar
Optical Frequency	1000G and Above	Scanning, Military Purposes, Radiation Detection

There are different modes of propagation of the radio waves. These are Surface Modes, Direct Modes and Ionospheric Modes. Surface mode propagation is basically groundwave propagation. It is mainly used for VLF and LF ranges, since attenuation is proportional to the frequency for this kind of mode propagation. Direct mode propagation is basically line-of-sight propagation. This sort of communication occurs at VHF and higher frequencies, where the antennas responsible for direct propagation are visible to each other. Ionospheric mode or skywave propagation occurs via refraction of radio waves in the ionosphere, made up of one or more ionized layers in upper ionosphere. This mode of propagation is used upto HF domain.

The whole Electromagnetic Spectrum is shown below in figure 1.1.

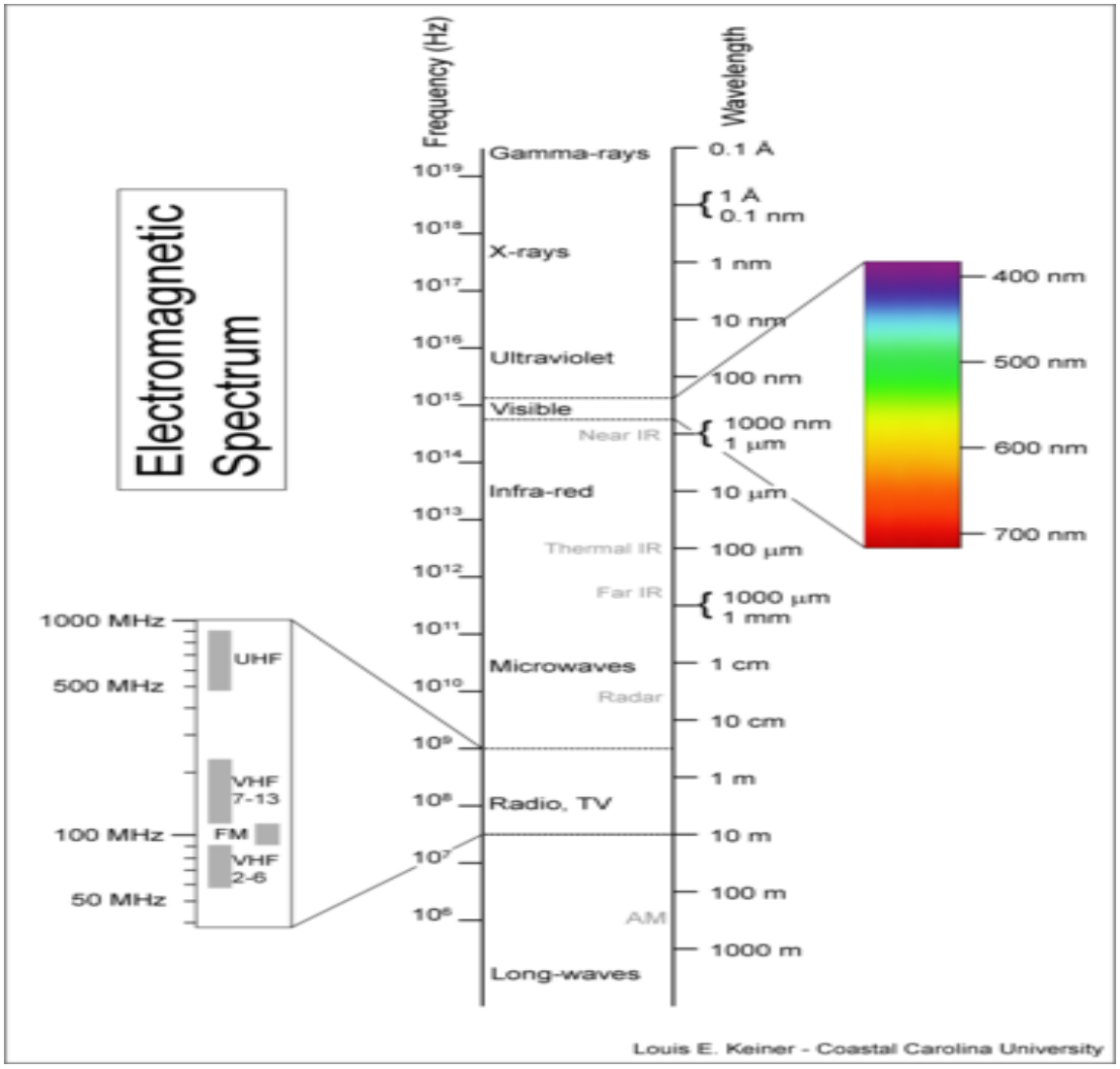

Figure 1.1: The Electromagnetic Spectrum

1.2. Different domains of Astronomy:

For proper detection of radiation from sky, there are different means of getting the signals by using large modern telescopes. To have greater resolution, the aperture size has to be made large. Signals are received by telescopes of progressively larger aperture. As far as placing of telescopes, there are atmospheric effects, which should be taken into account. To get rid of these, there are two possibilities. Firstly, they can be placed at high mountain sites or secondly, they can be placed at space. In 1990, Hubble Space Telescope has placed in the orbit at a height of 600 km. It has an aperture of 2.4 metre, giving rise to a resolution of 0.05 arc-secs. In ground-based telescopes, used in Adaptive Optics, light from primary mirror is directed onto a smaller flexible mirror behind which a larger number of actuators are located. The distortions in incoming light wave fronts caused due to the atmospheric perturbations are cancelled out by the actuators. Wave front distortions are sensed by monitoring a suitable bright star in the field of

view, or by monitoring an artificial star generated by shining a powerful laser beam into upper atmosphere. For having high resolution images generated by the telescopes, signals from two or more well-separated telescopes are combined.

The study of the universal phenomenon takes place at different frequencies of the Electromagnetic Spectrum. There are different windows in the whole Spectrum, giving rise to different types of Astronomy. There are windows in different transparent bands of radio frequency, as shown in figure 1.2, giving rise to different domains of astronomy. In fact, observing same object in different frequency band requires different technology as well as new sciences will be revealed.

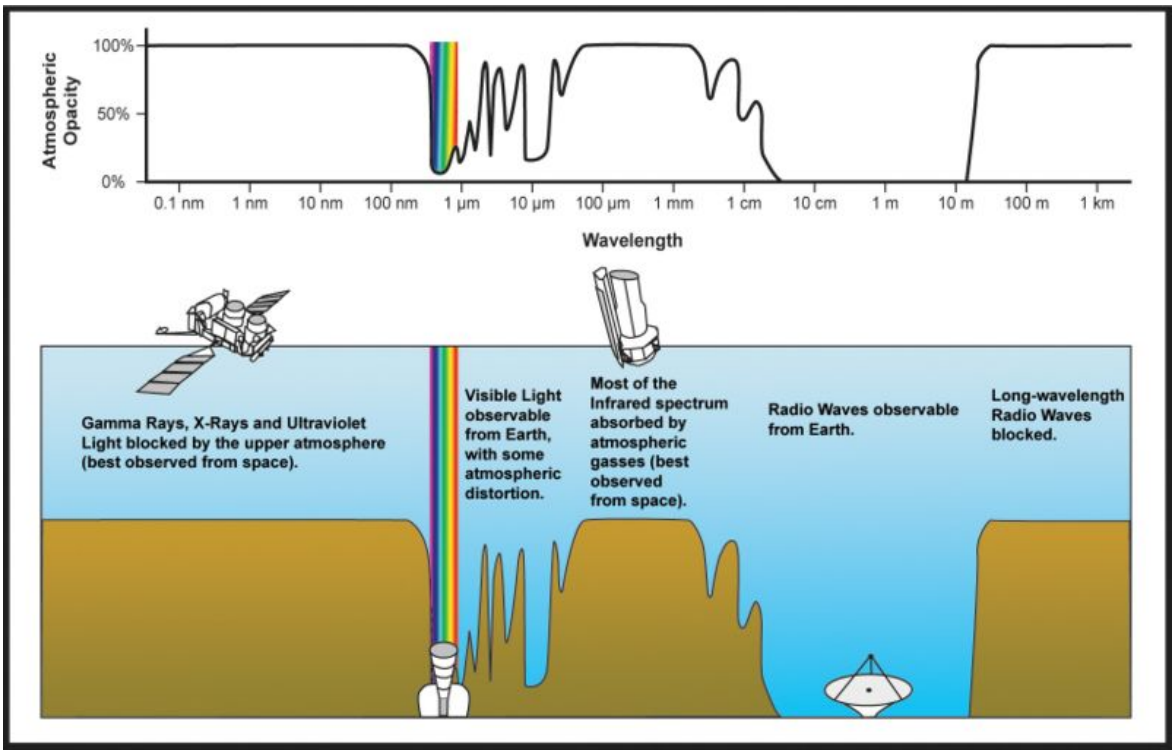

Figure 1.2: Electromagnetic Spectrum showing atmospheric opacity

From figure 1.2, it is seen that the atmosphere is transparent to wavelengths from about 300 nm (near UV) to 1.1 µm, which is broader compared to the visible spectrum ranging from 400 nm to 700 nm. This is called optical window. Most of the infrared radiation (700 nm – 350 µm) is absorbed in the atmosphere, but a small proportion in certain wavelength ranges penetrates down to observations at high-altitude sites. At a temperatures below 3000 Kelvin, all the radiations are in form of Infrared e.g., at a temperature of 300 Kelvin, the emission occurs at 10 µm, and at 30 Kelvin, the characteristic emission occurs at 100 µm. The Infrared radiation also occurs from absorbed radiation by atmosphere and water vapour and also by telescope with other instrumentations. In practice, sophisticated electronic detectors and techniques together with cool detectors can extract faint signal from star in a bright sky, keeping the noise down. The 3.8-metre UK IRT are in use from 1978 and the 8.3-metre Subaru Telescope at Mauna Kea, Hawaii are used as Infrared radiation detector. In 1983, a satellite has launched in space for detection of Infrared radiation, named Infrared Astronomical Satellite (IRAS).

At wavelengths between 390 nm and 10 nm, the Astronomy belongs to UV region. At wavelengths below 91 nm, the region is Extreme Ultra Violet (EUV). Here, the radiation comes from cosmic sources. In 10 nm – 0.01 nm region, incoming rays from gaseous bodies with temperatures between 1 mil K – 10 mil K are absorbed, which can be studied only in space, giving rise to X-ray astronomy. The radiations below the wavelength of 0.01 nm are strongly absorbed in atmosphere which cannot be focused by reflections. This is Gamma ray region. Here, scintillators are used which convert gamma rays into visible photons which are easily detected and analyzed. High energy Gamma rays i.e., having very short wavelengths can be detected from the ground level due to light flash generations. The sources of Gamma radiation are different Milky Way, Pulsars and Quasars.

The radio window is opaque for wavelengths between 2 cm to 30 m. In radio astronomy, the sky is studied at this wavelength range. This relatively young branch of science was first put into light by Karl G Jansky in 1931. The unit of flux is measured in Jansky ($1Jy \sim 10^{-26} Wm^{-2} Hz^{-1}$), to honour him. The use of radio frequency band of the electromagnetic spectrum is regulated by an international body, called International Telecommunication Union (ITU). ITU allocates radio frequency domains to different services. Radio astronomy is one of the services among these, but passive in nature, where no man-made transmission is involved along with the reception of the naturally occurring radio waves.

The Milky Way, which is the source of radio emission, was first observed by Jansky, who found that it is a complex assembly of stars of widely varying ages, embedded in an interstellar medium (ISM), of ionized and neutral gas, which displays a great diversity and complexity throughout the electromagnetic spectrum. The composition of ISM is interstellar dust particles, which absorbs radiation in visible domain of the spectrum. Thermal radiations from 21 cm line of neutral hydrogen can be studied in a wide variety of thermal regimes by radio astronomy techniques. Also, the thermal radiation from a wide variety of molecular lines, coming from dense, extremely cold gas concentrations are found in ISM. The radio noise discovered by Jansky belongs to the radiation from charged particles with very high energies and motion at relativistic velocities in the magnetic fields of ISM. This Synchrotron radiation regime accounts for intense quasars and other objects from universe radio emission. Synchrotron radiation is generated in X-band and is prominent in large-wavelength region also, making the study of energetic objects in the universe possible.

1.3. Characteristics of Radio Astronomy:

The spectrum of celestial radio waves reaching earth has a broad continuum, covering the whole frequency range penetrating the earth's atmosphere together with a large number of atomic and molecular spectral lines, each of which is confined to a quite narrow frequency range.

1.3.1. Continuum Emission:

The radio continuum is mainly due to two principles:

- Thermal emission, whose intensity is proportional to temperature produced in an ionized gas of unbound electrons and protons.
- Most of the radio sources have a characteristic nonthermal spectrum. This is high-energy relativistic particles generated radiation in presence of magnetic fields, called synchrotron emission. This produces a radio spectrum with a negative slope ~ 0.8 in a log-frequency

vs. log flux density plane. So, these sources have higher radio fluxes at lower radio frequencies. However, at sufficiently low frequencies, decrease of flux density occurs due to self-absorption.

In galaxy, both these thermal and non-thermal diffuse radiation plays a significant role in low-frequency domain observations. Such galactic observations give information on high-energy particles in the Galaxy and their distribution, together with the hot ionized plasma in Galaxy plane. The ionized interstellar clouds can be studied particularly at lower frequencies, where their spectra are identical with that of a blackbody. At frequencies below 100 MHz, several hundreds of such galactic clouds appear approximately as blackbody. These spectral line observations reveal information regarding physical parameters of radiating clouds, especially their temperatures.

1.3.2. Line Emission:

The most widely used spectral line occurs at 21 cm wavelength due to the neutral atomic (non-ionized) hydrogen in interstellar gas. Several other lines from different atoms and their isotopes have been detected. This gives the information regarding the chemistry and kinematics within the radio sources and their structure. From study of spectral lines from different molecules tell about the complexity of them. The development of chain of compounds can be traced out by searching appropriate spectral lines from study of Astrochemistry. The physical conditions inside a molecular cloud can be realized by comparison of relative strengths of lines from different molecules or intra-molecular transition.

1.4. Receivers for Radio Astronomy:

The radio telescopes are in different forms; it may be steerable, or fixed. In steerable dish, the concave reflector brings the waves to focus which may be incident in any direction. The largest steerable dish is situated at present in Bonn, Germany having a diameter of 100 metre. Among the fixed dish, there is a 305 metre diameter dish built into a natural bowl-shaped hollow at Arecibo on the Caribbean Island of Puerto Rico.

For a radio astronomical receiver, the resolution has a diffraction limit ~ λ/d, and the resolving power is given in equation 1.2, where R is the resolving power, λ is the operating wavelength and d is the aperture size.

$$R = \frac{1.22\lambda}{d} \tag{1.2}$$

To achieve the same resolution as in optical telescope, the physical aperture of the radio telescope should be very large (~ 1 km). If the two telescopes, separated by a known distance, known as the baseline are used to study the same source, then depending on the angle of arrival to horizontal at which the source is located, the wave fronts arriving at two dishes may be in phase in which they will add together, or out of phase; if a crest arrives at one when there is a trough at the other, the two waves get cancelled. The resulting interference pattern reveals the position or finer details of the source. In Very Large Baseline Interferrometry (VLBI), the resolution power ~ 0.001 arc-sec. Usually, antenna arrays are used instead of a single antenna to have a greater resolution and sensitivity. Also, it is very difficult to build a single dish of diameter more than 100 metre. Signals from a radio source are combined and processed in such a way that the imaging of the source can be generated successfully.

The radio telescope is used mainly to detect and measure the radiation of the radio emission of very low average power levels (~1 mJy to 1 μJy), but the system noise power

are higher than this level. The output fluctuations from the receiver can be reduced by measuring them over a large integration time and bandwidth; decreasing the fluctuations by square root of integration time and bandwidth over average power. This increases the sensitivity also (European Science Foundation [19]). Also, the receivers should possess high dynamic range for observations with highly varying solar bursts or giant pulses from pulsars.

There are different types of receivers available in radio astronomy. A common arrangement of a radio astronomical receiver is shown in figure 1.3 (Ajith Kumar [2]). The most common radio receiver is the total power receiver, whose block diagram is shown in figure 1.4. Here, the total noise power is measured from the antenna and the receiver system, unlike some receiver which measure power difference from antenna and the receiver. Here, the receiver gain, in practice, varies due to supply voltage and ambient temperature variations. By frequency calibrations, this has been overcome by Ryle, Volberg and Dicke. Here, the receiver input is switched between antenna and comparison noise source at a frequency high enough so that the gain will not change during the one cycle (vide figure 1.5). So, antenna and the comparison load are connected alternatively to the receiver half the time at a switching frequency ranging from 10 Hz to 1 MHz. In spectral line measurements, the signal antenna also serves as the reference load by switching receiver frequency during reference period outside the spectral line part of the spectrum.

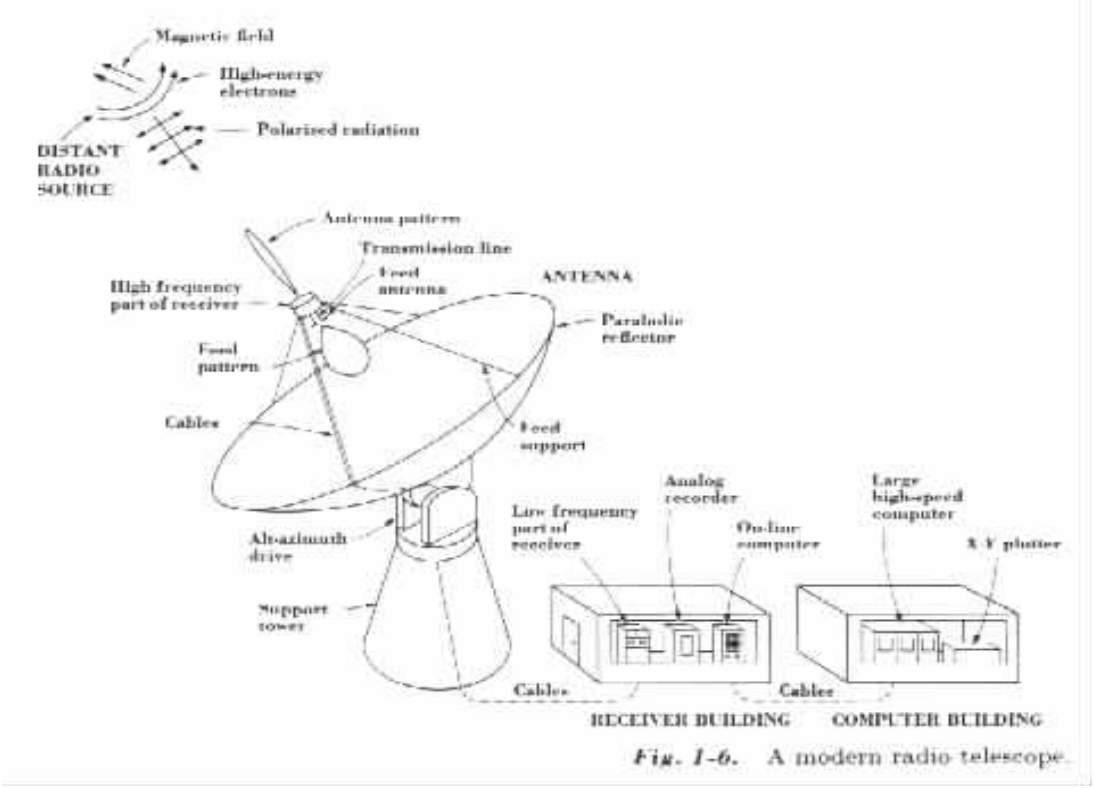

Figure 1.3: A General Radio Astronomical Receiver

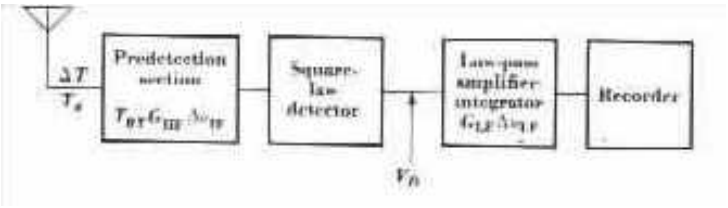

Figure 1.4: Total Power Receiver

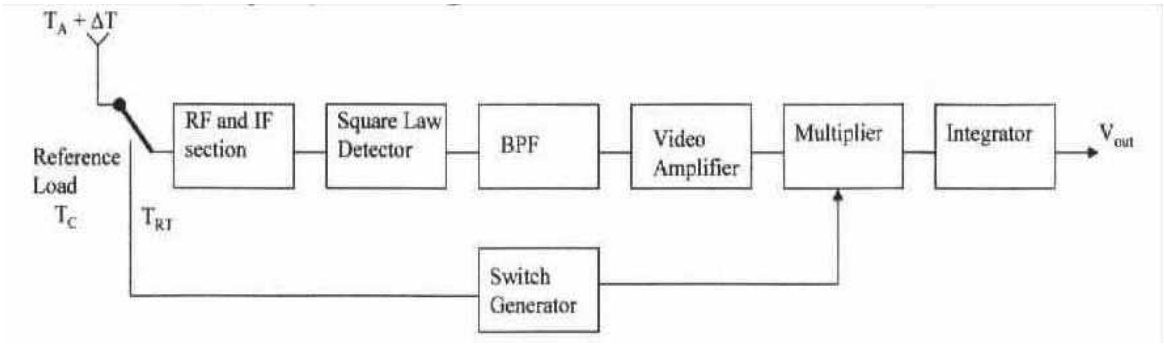

Figure 1.5: Dicke Receiver

A radio interferometer receiver (vide figure 1.6) consists of two or more antennas separated from each other by several wavelengths. Each of them is equipped with its own preamplifiers and entire pre-detection sections with identical electrical characteristics. While the same source is tracked, equal signal voltages are induced with phase difference depending on the source direction. The IF signals are added and then fed to a square law detector. Two antennas and two receivers increase the maximum sensitivity in interferometer receiver to twice as that of a total power system with same system temperature. But, here also, the problem of gain instability creeps in, which is removed by the use of correlation receiver (vide figure 1.7), where the IF signals are multiplied so that uncorrelated noise voltages are mutually cancelled and correlated ones give rise to a dc output to remove the instabilities.

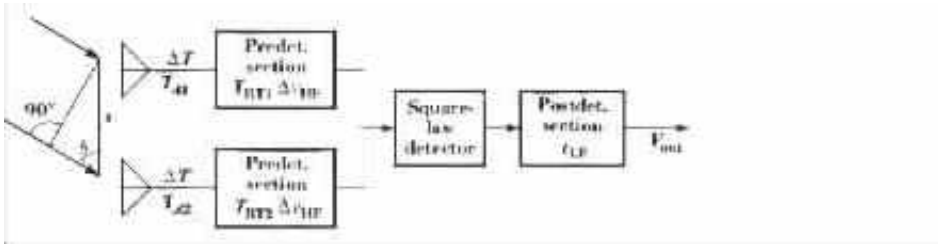

Figure 1.6: Interferometer Receiver

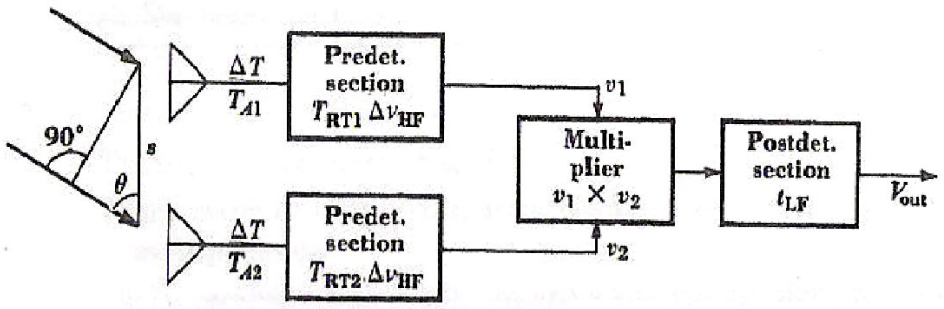

Figure 1.7: Correlation Receiver

The first stage of a radio astronomical receiver is antenna, which is also present at the repeater and terminal station. Also, due to the non-linearity of the system, intermodulation occurs. There are different forms of non-linearity. Firstly, amplitude nonlinearity is present in modulation, discrimination and amplifiers handling baseband signals. Secondly, there are nonlinearities in phase and frequency in tuned circuit handling RF and IF signals.

For a radio astronomical antenna, the situation is identical to the system that the antenna is enclosed by a blackbody at temperature T. From second law of Thermodynamics, if it is completely isolated from the outside world, the equilibrium temperature is also T. Moreover, same power density at radio frequency domain for any narrow band flow in both directions. The radiation density u_f within an infinitesimal spectral domain df is given in equation 1.3.

$$u_f df = \frac{8\pi h f^3}{c^3} \frac{1}{(e^{\frac{hf}{kT}} - 1)} df \tag{1.3}$$

For an extended source, the source strength is characterized by sky brightness $B(f)$ which is the energy flux at earth per unit area per unit time per unit solid angle, expressed in the unit $Wm^{-2}Hz^{-1}sr^{-1}$. The mode density within a cavity of spectral region of f and $f + df$ is expressed in spectral radiance N_f, which is expressed in equation 1.4.

$$N_f = \frac{2hf^3}{c^2} \frac{1}{(e^{\frac{hf}{kT}} - 1)} \tag{1.4}$$

For low frequency, this expression is converted into Rayleigh-Jeans approximation. The modified expression is given by equation 1.5, and the equivalent sky brightness of the source is given by equation 1.5.

$$N_f = \frac{2kTf^2}{c^2} = \frac{2kT}{\lambda^2} \tag{1.5}$$

$$T = \frac{\lambda^2}{2k} B(f) \tag{1.6}$$

1.5. Some Important Radio Telescopes:

There are a number of radio telescopes exist all over the world. Some of these are single-dish; while others are antenna array. The resolution of an antenna depends upon the physical aperture of the antenna, where resolution varies inversely with the physical aperture of the antenna. In an array telescope, the physical aperture is the distance between the two farthest antennas. So, the resolution is more in array antennas. Also, due to practical limits, it is very difficult to construct a telescope of aperture greater than 100 meter. Signals from the array telescopes are combined and then processed in such a fashion that the source map can be constructed. Some of the important Radio Telescopes in the world are Westerbork Synthesis Radio Telescope (WSRT) in Netherlands (vide figure 1.8(a)), Very Large Array (VLA) in USA, having 27 antennas (vide figure 1.8(b)), eMerlin in UK (vide figure 1.8(c)) having 5 antennas, spreading over 230 km, GMRT in India (vide figure 1.8(d)).

Figure 1.8(a): Astron, WSRT, Netherlands

Figure 1.8(b): VLA, NRAO, USA

Figure 1.8(c): eMerlin, Manchester, UK

Figure 1.8(d): GMRT, TIFR, India

Chapter 2

GMRT and Its Receiver System

2.1. An Introduction to GMRT:

India offers unique advantages for radio astronomical observations at meter wavelengths. These are:

- A much lower degree of man-made radio frequency interference than that exists in the developed countries.
- The labour intensive nature of meter-wave radio telescopes.
- Coverage of both northern and the southern skies from a location in the southern India.

Due to these, the Giant Metrewave Radio Telescope (GMRT), the largest research facility of the world in meter and decimeter band, has been set up. It consists of an array of 30 antennas; each of diameter 45 meter. GMRT observatory is run by National Centre for Radio Astrophysics (NCRA), Pune, of Tata Institute of Fundamental Research. GMRT is located at a site about 90 km north of Pune, near a village named Khodad. GMRT consists of 30 fully steerable gigantic parabolic dishes of 45m diameter each spread over distances of upto 25 km. It is one of the most challenging experimental programmes in basic sciences undertaken by Indian scientists and engineers. The site for GMRT, about 10 km east of Narayangaon town on the Pune-Nasik highway, was selected after an extensive search in many parts of India, considering several important criteria such as low man-made radio noise, availability of good communication, vicinity of industrial, educational and other infrastructure and, a geographical latitude sufficiently north of the geomagnetic equator in order to have a reasonably quiet ionosphere and yet be able to observe a good part of the southern sky as well. The meter wavelength part of the radio spectrum has been particularly chosen for study with GMRT because man-made radio interference is considerably lower in this part of the spectrum in India. Although there are many outstanding astrophysics problems which are best studied at meter wavelengths, there has, so far, been no large facility anywhere in the world to exploit this part of the spectrum for astrophysical research (Chaudhari, Sandeep C., 2005 [10]).

Currently, GMRT operates at five frequency bands, centered at 150 MHz, 233 MHz, 327 MHz, 610 MHz and L-band covering 1000 to 1450 MHz. The antennas in GMRT are constructed using a novel technique, called SMART (Stretched Mesh Attached to Rope Trusses) and their reflecting surface consists of panels of wire mesh. These panels are attached to rope trusses, and by appropriate tensioning of the wires used for attachment, the desired parabolic shape can be achieved. The dish has been made light-weight and of low solidity by replacing the conventional back-up structure by a series of rope trusses (made of thin stainless steel wire ropes) stretched between 16 parabolic frames made of tubular steel. The wire ropes are tensioned suitably to make a mosaic of plane facets approximating a parabolic surface. A light-weight thin wire mesh (made of 0.55 mm diameter stainless steel wire) with a grid size varying from 10 X 10 mm in the central part of the dish to 20 x 20 mm in the outer parts, stretched over the rope truss facets forms the reflecting surface of the dish. The low-solidity design cuts down the wind forces by a large factor and is particularly suited to Indian conditions where there is no snowfall in the plains. The overall wind forces and the resulting torques for a 45-m GMRT dish are similar to those for only a 22-m dish of conventional design, thus resulting in substantial savings in cost (Chengalur, Jayaram N., 2003 [11]).

Although GMRT is a very versatile instrument for investigating a variety of radio astrophysical problems ranging from our nearby Solar system to the edge of the observable Universe, two of its most important astrophysical objectives are:

- To detect the highly redshifted spectral line of neutral Hydrogen expected from protoclusters or protogalaxies before they condensed to form galaxies in the early phase

of the Universe and

- To search and study rapidly-rotating Pulsars in our galaxy (Chengalur, Jayaram N., 2003 [11]).

Apart from these, GMRT has a number of scientific goals. These are:

- **Epoch of Galaxy Formation**: Theories of the formation of structure in the Big-Bang Universe predict the presence of proto galaxies or proto clusters of galaxies made up of clouds of neutral Hydrogen gas before their gravitational condensation into galaxies. It should in principle be possible to detect these through the well known radio line emitted by neutral Hydrogen at a frequency of 1420 MHz. The line is however expected to be very weak and redshifted to meter wavelengths because of the expansion of the Universe between emission, billions of years ago, and detection at the present epoch. For clouds of Hydrogen between redshifts 3 and 10 (corresponding to epochs when the Universe had attained only a few percent of its present age), the line should be observable between frequencies of about 350 and 130 MHz. Detection of such neutral Hydrogen clouds is of fundamental astrophysical importance and can provide very important constraints to the theories of formation of galaxies and clusters.
- **Pulsars and neutron stars:** GMRT is an ideal instrument to study the effects of Pulsars which are rapidly rotating neutron stars of extremely high densities of 200 million tons/cm^3. Its large collecting area can lead to a 3 to 4-fold increase in the number of Pulsars known in our Galaxy. A particularly important programme in Pulsar research will be the search for extremely rapidly rotating pulsars with periods in the range of only milli-seconds and for pulsars in binary systems. Because of the strong gravitational fields associated with them, such systems form excellent laboratories for testing gravitational theories such as Einstein's General Theory of Relativity. Accurate timing measurements to detect extremely minute changes in the pulse arrival times from a group of pulsars could also lead to the detection of a weak background of gravitational radiation believed to have been generated by asymmetries in the very early Universe when it was less than a billionth of a billionth of a billionth of a second old!
- **Galactic and extragalactic radio sources:** Due to the large collecting area and wide frequency coverage, GMRT will be an invaluable and highly versatile instrument for studying many other problems at the frontiers of astrophysics. These include studies of Solar and planetary radio emissions; relationship between Solar activity and disturbances in the interplanetary medium; surveys of the Galactic plane to investigate the physics and evolution of clouds of ionized hydrogen associated with young stars as well as no thermal emission from planetary nebulae and supernova remnants associated with late stages of stellar evolution; exotic types of stars and stellar systems whose radio emission could be hundreds of times more intense than that of the Sun; monitoring the variability of extragalactic radio sources, supernovae in external galaxies and transient sources in the Galactic plane; detection of the Deuterium line and Hydrogen recombination lines in the interstellar medium; halos and large-scale structure in spiral galaxies; structures and spectra of quasars and radio galaxies and their use in cosmological tests; studies of Hydrogen gas in external galaxies and streaming motions in the nearby universe.

2.2. Array Configuration of GMRT:

The number and configuration of the dishes was optimized to meet the principal astrophysical objectives which require sensitivity at high angular resolution as well as ability to image radio emission from diffuse extended regions. Fourteen of the thirty dishes are located

more or less randomly in a compact central array in a region of about 1 km^2. The remaining sixteen dishes are spread out along the 3 arms of an approximately `Y'-shaped configuration over a much larger region, with the longest interferometric baseline of about 25 km. The multiplication or correlation of radio signals from all the 435 possible pairs of antennas or interferometers over several hours will thus enable radio images of celestial objects to be synthesized with a resolution equivalent to that obtainable with a single gigantic dish 25 kilometer in diameter! The array will operate in five frequency bands centered on 153, 233, 325, 610 and 1420 MHz. All these feeds provide dual polarization outputs. In some configurations, dual-frequency observations are also possible. The highest angular resolution achievable will range from about 60 arcsec at the lowest frequencies to about 2 arcsec at 1.4 GHz.

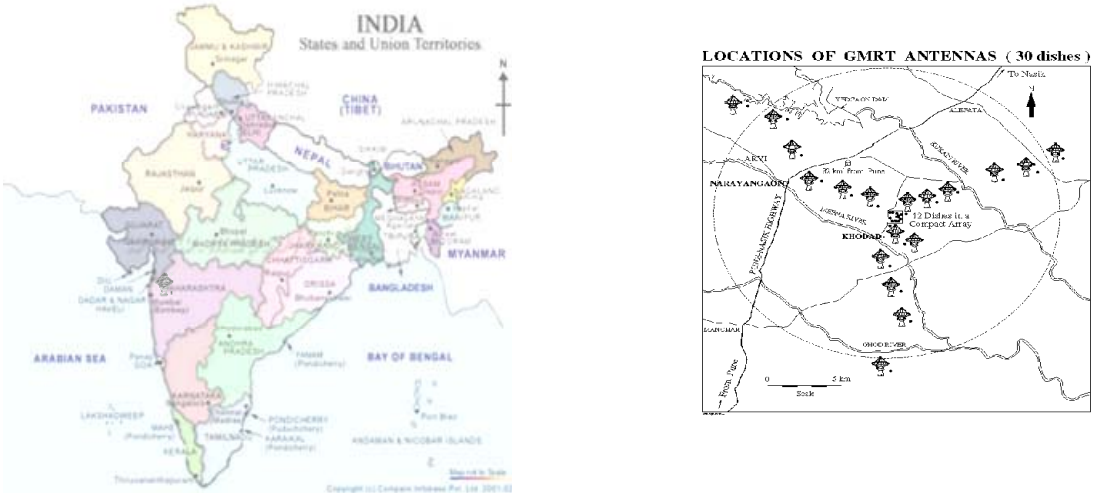

Figure 2.1: Locations of GMRT Arrays

The large size of the parabolic dishes implies that GMRT has three times the collecting area of the Very Large Array (VLA) in New Mexico, USA which consists of 27 antennas of 25 m diameter and is presently the world's largest aperture synthesis telescope operating at centimetre wavelengths. At 327 MHz, GMRT is about 8 times more sensitive than VLA because of the larger collecting area, higher efficiency of the antennas and a substantially wider usable bandwidth because of the low level of man-made radio interference in India.

2.3. Equatorial Anomaly in GMRT:

Regarding the location of GMRT within equatorial region of ionosphere, operating frequencies at 150, 233, and 327 MHz and sometimes even at 610 MHz and 1420 MHz is subjected to serious limitations. These are:

2.3.1. Zone Reception:

While passing through the ionosphere, a signal undergoes reflection and refraction and there is a maximum plasma frequency (or, critical frequency) of the layer beyond which the wave penetrates through it. For oblique propagation, the frequency is modified by the Secant Law. From available models of ionosphere, it can be shown that no signal reception would be possible at 38 MHz around 90^o and 270^o azimuthal angle even at an elevation angle of

45^{o} in the afternoon hours of high solar activity years.

2.3.2. Ray Bending:

Due to the high density, radio waves propagating through the ionosphere in equatorial region are likely to undergo deviations even at 150 and 233 MHz, introducing error in the angle of arrival and hence, the true direction of the source will be different from the apparent direction. Within the equatorial region, there is a large electron density distribution gradient both in horizontal and vertical directions. Thus, angular errors will vary with the look angle.

2.3.3. Group Delay:

Radio waves travel through ionosphere with a velocity different from that of light. Thus, the signal received at 1420 MHz may suffer a large group delay. Moreover, different group delays at different look angles are source of serious errors in long baseline interferrometry.

2.3.4. Faraday Rotation:

The Magnetic Field of Earth permeates the ionosphere, making it birefringent for radio waves. Thans-ionospheric signals with linear polarization come out of ionosphere with a rotation of the plane of polarization. This is called Faraday rotation. A high-ambient ionization which is normally obtained in equatorial region introduces a differential Faraday rotation over large signal bandwidth used for radio astronomical observations (Paul, Ashik, 1996 [1]). From the viewpoint of large ionization gradient in equatorial region, due to equatorial anomaly, there may be differential polarization rotation across antenna beam.

2.3.5. Scintillation:

The ionosphere at equator has most of the irregularities. The density irregularities produce phase perturbations, developing into scintillations of amplitude and phase of a trans-ionospheric signal. Due to the irregularities in the ionosphere drift, the pattern is reflected into the antennas. In the equatorial region, during major part of night of certain seasons, fading occurs in excess of 10 dB, even at 1420 MHz when the ray passes through the anomaly crest. Thus, when the signal is received after it is passed through the ionosphere, saturated scintillation may extend after the VHF through the microwave bands for several hours after sunset. During this period, scintillation may not be so intense in UHF and other microwave bands. So, a proper planning of look angles and frequency may be useful in selecting suitable antenna direction during scintillation period. The possibility of differential phase perturbations over the frequency band and across antenna bandwidth may be significant due to latitudinal dependence of equatorial scintillation and high-density deviation. In certain regions of equatorial ionosphere, particularly around anomaly crest, the signal polarization often exhibits fast fluctuations during periods of severe amplitude scintillations, called Fast Polarization Fluctuations (FPF).

2.3.6. Large Scale Structure:

Large scale structures, tilts, periodic variations may produce significant perturbations over received radio signal wavefront causing contamination of some of the observations.

2.4. Overview of GMRT Receiver System:

The GMRT receiver chain is shown schematically in figure 2.2. It operates at five frequency bands centered at 150 MHz, 233 MHz, 327 MHz, 610 MHz and 1420 MHz with sub-bands of 1060 MHz, 1170 MHz, 1280 MHz and 1390 MHz in the L-band (Basu *et al.*, 2006 [4]).

The feeds at these frequencies provide dual-polarization output. There are two channels in the receiver, through which the RF signal is passed, each of which has a bandwidth of 32 MHz.

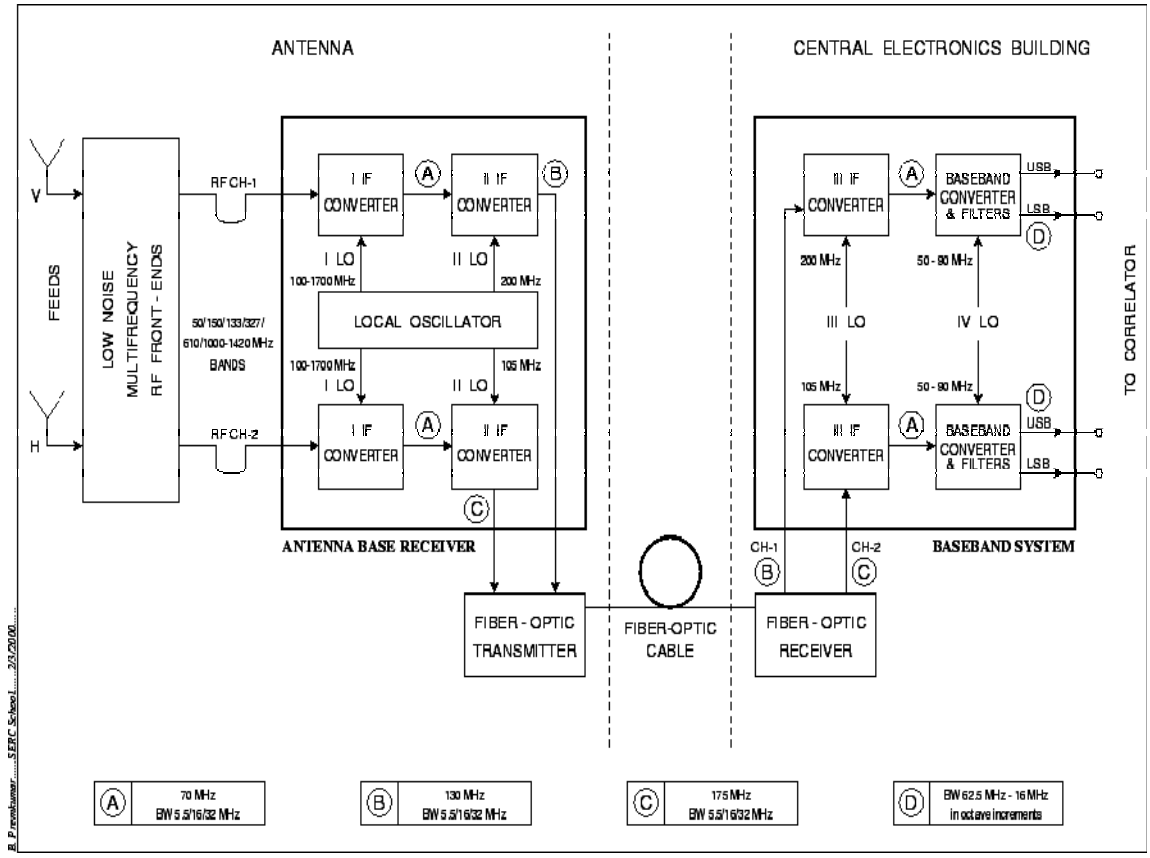

Figure 2.2: Block Diagram of GMRT Receiver Chain

The first local oscillator (I LO, situated at the base of the antenna, inside a shielded room) converts the RF band to an IF band centered at 70 MHz. After passing the signal through a bandpass filter of selectable bandwidth, the IF at 70 MHz is then translated (using II LO) to a second IF at 130 MHz and 175 MHz for CH1 and CH2, respectively. The maximum bandwidth available at this stage is 32 MHz for each channel. This frequency translation is done so that signals for both polarizations can be frequency division multiplexed onto the same fiber for transmission to the CEB.

At the CEB, these signals are received by the Fiber-Optic Receiver and the 130 and 175 MHz signals are then separated out and sent for base band conversion. The baseband converter section converts the 130 and 175 MHz IF signals first to 70 MHz IF (using III LO), these are then converted to upper and lower side bands (each at most 16 MHz wide) at 0 MHz using a tunable IV LO. There are also two Automatic Level Controllers (ALCs) in the receiver chain (not shown in Figure 2.2 but discussed in more detail below). The first is just before the Fiber Optic transmitter and the second is at the output of the baseband unit (Praveenkumar, A., 2003 [28]).

2.5. Receiver Design Considerations:

The various blocks of the receiver chain has some gain (or loss) associated with it. The receiver chain possesses distributed gain. The gain consideration is used to distribute the gain across the RF, IF and BB electronics, viz,

1. The response of the entire system must remain linear over a wide range of noise temperatures from cold sky to the high antenna temperatures anticipated when observing strong sources like the Sun.
2. The entire receiver system should remain linear even in the presence of strong interference signals. In particular the inter-modulation distortion (IMD) products should be below a critical threshold. Also the receiver should have a high desensitization dynamic range so that a single dominant out of band interfering signal does not reduce the receiver SNR by saturating the subsystems in the receiver.
3. The RF Front End gain should be such that no more than 1 K noise is added to the Low Noise Amplifier (LNA) input noise temperature by the rest of the receiver chain.
4. The gain should be so distributed that no more than 1% gain compression should occur at any stage of the receiver chain.
5. The level of signals at the input of the cables that run from antenna turret to the base of antenna should be sufficiently high compared to any extraneous interference signals that might be picked by these cables.
6. Components whose contribution to the signal phase needs to be kept constant should preferably be located at the antenna base room where the temperatures are relatively stable compared to that at the prime focus.
7. Internally-generated spurious products (if any) in the receiver, must be very low compared to the receiver noise floor.
8. The Antenna Base Receiver (ABR) input (which receives the RF signals from the front end through long lengths (about 100 m of cable) should be well matched for the full RF band i.e. 10 MHz to 1600 MHz. A poor match would result in pass band ripples.
9. The receiver should have a good image rejection (at least 25 dB). Further since the RF pass band in the common box electronics (see below) has 10 MHz - 2000 MHz coverage, a 70 MHz signal may find a path past the amplifiers and mixer and be coupled into the 70 MHz IF circuitry. The units have to be optimally configured such that a good IF rejection is achieved.
10. The ALCs should be active over a large signal amplitude range.

2.6. Fiber-Optic Link of GMRT:

Figure 2.3 shows the schematic block diagram of the fiber-optic forward link. The link consists of a laser diode (which converts the input electrical signal into an optical signal), the optical fiber itself, a photo diode (which converts the optical signal back into an electrical signal) followed by an amplifier and a 2 way divider which separates out the monitoring data as well as the two polarizations of the astronomical signal.

The Local Oscillator signal meant for locking the antennae and the telemetry signals for controlling the antenna are sent from the Central Electronics Building (CEB), after combining them using a power combiner of gain 3.5 db and passed to the optical transmitter

having a directly modulated Fabry Perot Laser module that converts this incoming signal to optical domain and transfers it to the antennae bases through the optical fibers. This optical signal at the receiver end causes the receiver pin-photodiode to produce a photocurrent and hence the optical signal gets reconverted back to electrical signal. This signal is then passed through a pre-amplifier of gain of 31 dB, a 3dB attenuator and a post amplifier of gain of 31 dB. The final signal is then again splitted back to its original contents and provided to the antenna.

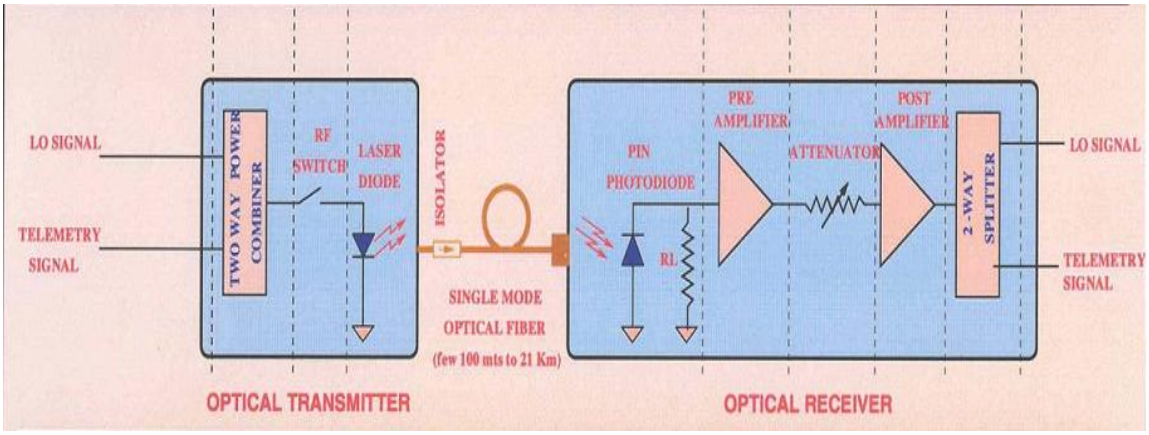

Figure 2.3: Block Diagram of Fiber Optic Link (Forward Link)

The return link is shown in figure 2.4. Here, the link is similar to the forward link except for the 5 way splitter used at the receiver end based at the CEB. This 5-way splitter splits the incoming signal to five different signals which are then forwarded to different concerned departments as shown. The fiber-optic receiver also contains 32 MHz SAW filters centered at 130 and 175 MHz to separate out the 130 and the 175 MHz IF signals for routing to the base band converter subsystem. The level of the signal at this point is nominally -49 dBm.

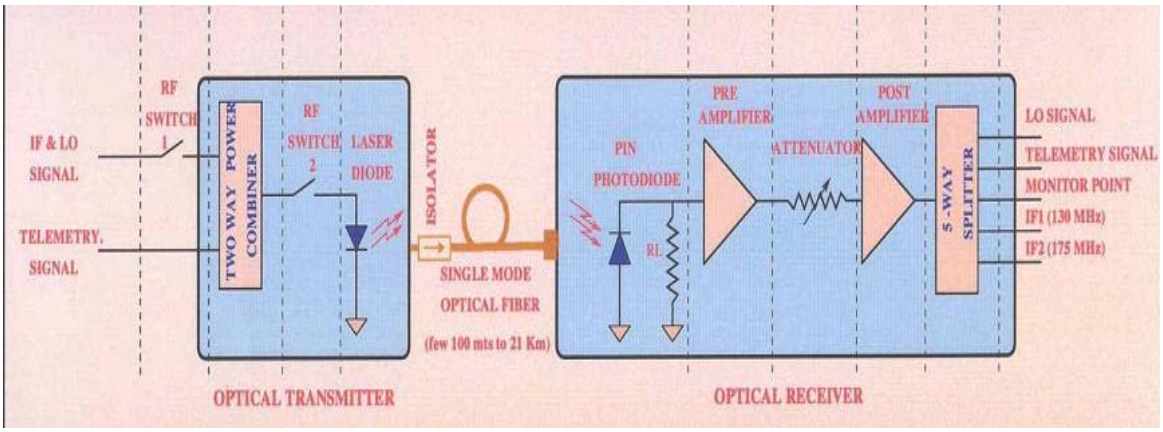

Figure 2.4: Block Diagram of Fiber Optic Link (Return Link)

In the GMRT fiber-optic link, there are non idealities including the laser intensity noise, shot noise and thermal noise of the laser diode, loss and reflections in the optical fiber, as well as shot noise and thermal noise in the photo-diode. The specification of optical transmitter and optical receiver of existing GMRT fiber-optic link is given in tables 2.1 and 2.2 respectively.

Table 2.1 (Transmitter)

RF Parameters:

Laser Diode: Lasertron, part No. QLM3S860SPEC

Modulation Bandwidth	60KHz - 1GHz
Frequency Response	+/- 2.0 dB
Input Impedance	50 Ohm
Input 1dB compression point [Measured with 32MHz wide , noise source centered at 70MHz]	> +10 dBm
Input 3rd order intercept point	> +18 dBm
Equivalent input noise	<= -135 dBm

DC Parameters:

Slope Efficiency [slope of Power Vs Current curve]	>= 0.04mW/mA
Optical Output Power	>= 0.5mW
Peak Optical Wavelength	1300 +- 10 nm
Spectral Width (rms)	<1.5 nm
Maximum DC power Requirement	+5V @ 1 A [T_{amb} = 65^o C] -5 V @ 80 mA [T_{amb} = 25^o C] +12V @ 80 mA

Table 2.2 (Receiver)

RF Parameters:

Photo Diode: Epitax make, part No; ETX75FJ-SLR

Modulation Bandwidth	7MHz - 870 MHz (min)
Frequency Response	+-2.0 dB
Input Impedance	50 Ohm

DC Parameters:

Responsivity	>= 0.8 mA/mW
Operating Wavelength	1100 - 1600 nm
Optical Return Loss	> 45 dB
Maximum DC Power Requirement	+12V @ 90 mA

Chapter 3

A Fibre-Optic Link

3.1. Laser Sources:

A fiber-optic transmission link is shown in figure 3.1. Here, Light Emitting Diode (LED) or Light Amplification by Stimulated Emission of Radiation (LASER) is used as transmitter. A basic block diagram of a fiber-optic link is shown below in figure 3.1.

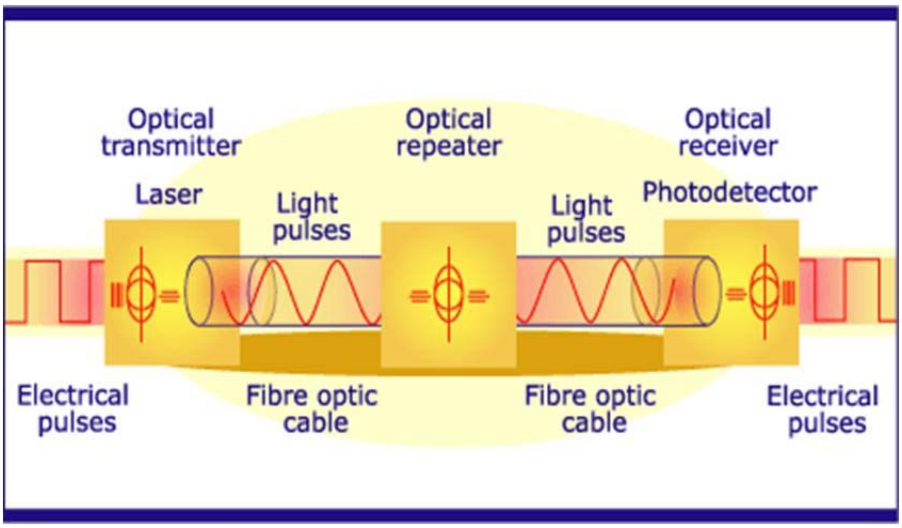

Figure 3.1: A Basic Fiber-Optic Link

Here, the source i.e., the laser converts the input electrical signal into the optical signal which is travelling via the optical fiber and there are optical repeaters along the link which regenerate the optical signal after it becomes attenuated via the synchronization bit sent along with it. At the receiver end, there is photodetector which reconverting the optical signal back to its electrical form. Compared to LED, Lasers possess some unique advantages.

- **Coherent:** In laser light each photon moves in step with others i.e. the all the photons contained in this light have similar wavelength and similar phase. But in a flashlight, the photons may have different wavelengths and different phases. Hence they cannot be called as coherent.

- **Monochromatic:** The Laser has only one wavelength and hence one colour only. The wavelength of the emitted photon in a Laser depends on the energy lost by the Photon. A flashlight on the other hand comprises of more than one wavelength and hence they are not monochromatic.

- **Unidirectional:** Laser is unidirectional, a tight beam, strong and concentrated. A flashlight on the other hand has photons moving in different directions.

- **Emission:** In a flashlight almost all the particles undergo spontaneous emission and hence the photons emitted are not coherent. But in a Laser the particles undergo stimulated emissions hence all the released photons have same wavelength and phase and thus are coherent.

- **Action:** In flashlight or LEDs, as the current rises from 0 level, their Light output also increases linearly. But in Lasers the light output begins to rise only after a certain level of current called threshold.

A laser usually comprises an optical resonator (laser resonator, laser cavity) in which light can circulate (e.g. between two mirrors), and within this resonator a gain medium (e.g. a laser crystal), which is used to amplify the light. Without the gain medium, the circulating light would become weaker and weaker in each resonator round trip, because it experiences some losses, e.g. upon reflection at mirrors. However, the gain medium can amplify the circulating light, thus compensating the losses if the gain is high enough. The gain medium requires some external supply of energy – it needs to be "pumped", e.g. by injecting light (optical pumping) or an electric current (electrical pumping), as shown in figure 3.2. The main principle of laser amplification is stimulated emission.

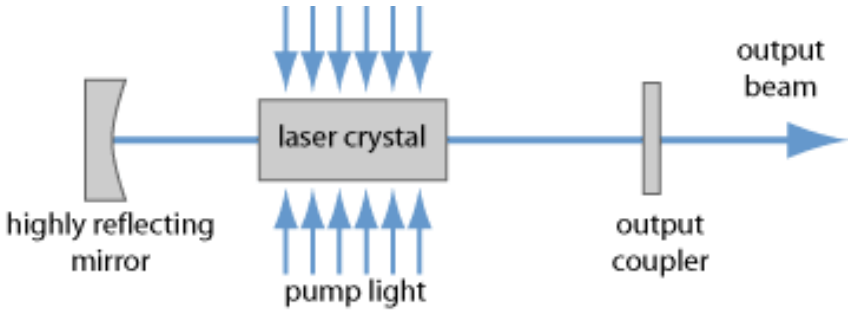

Figure 3.2: Principle of Operation of Laser

A laser cannot operate if the gain is smaller than the resonator losses; the device is then below the so-called laser threshold and only emits some luminescence light. Significant power output is achieved only for pump powers above the laser threshold, where the gain can exceed the resonator losses. If the gain is larger than the losses, the power of the light in the laser resonator quickly rises, starting e.g. with low levels of light from fluorescence. As high laser powers saturate the gain, the laser power will in the steady state reach a level so that the saturated gain just equals the resonator losses (gain clamping). Before reaching this steady state, a laser usually undergoes some relaxation oscillations. The threshold pump power is the pump power where the small-signal gain is just sufficient for lasing. Some fraction of the light power circulating in the resonator is usually transmitted by a partially transparent mirror, the so-called output coupler mirror. The resulting beam constitutes the useful output of the laser. The transmission of the output coupler mirror can be optimized for maximum output power.

Some lasers are operated in a continuous fashion, whereas others generate pulses, which can be particularly intense. There are various methods for pulse generation with lasers, allowing the generation of pulses with durations of microseconds, nanoseconds, picoseconds, or even down a few femtoseconds (ultrashort pulses from mode-locked lasers).

The optical bandwidth (or line width) of a continuously operating laser may be very small when only a single resonator mode can oscillate (Single-mode laser). In other cases, particularly for mode-locked lasers, the bandwidth can be very large – in extreme cases, it can span about a full octave. The centre frequency of the laser radiation is typically near the frequency of maximum gain, but if the resonator losses are made frequency-dependent, the laser wavelength can be tuned within the range where sufficient gain is available. Some broadband gain media such as Ti: sapphire and Cr: ZnSe allow wavelength tuning over hundreds of nanometres.

In the earlier days, Solid-State lasers are of most use. Two important lasers among them are Ruby Laser and Helium-Neon Laser. Ruby Laser, discovered by Maiman in 1960, is able to produce pulses of visible light at 694.3 nm, which is deep red in colour. Their pulses are generated at milliseconds. The Helium-Neon laser is a gas laser, which can generate pulses at 632.8 nm, was discovered in 1961 by Ali Javan et al. Their transition spectra are shown in figure 3.3 and 3.4 respectively.

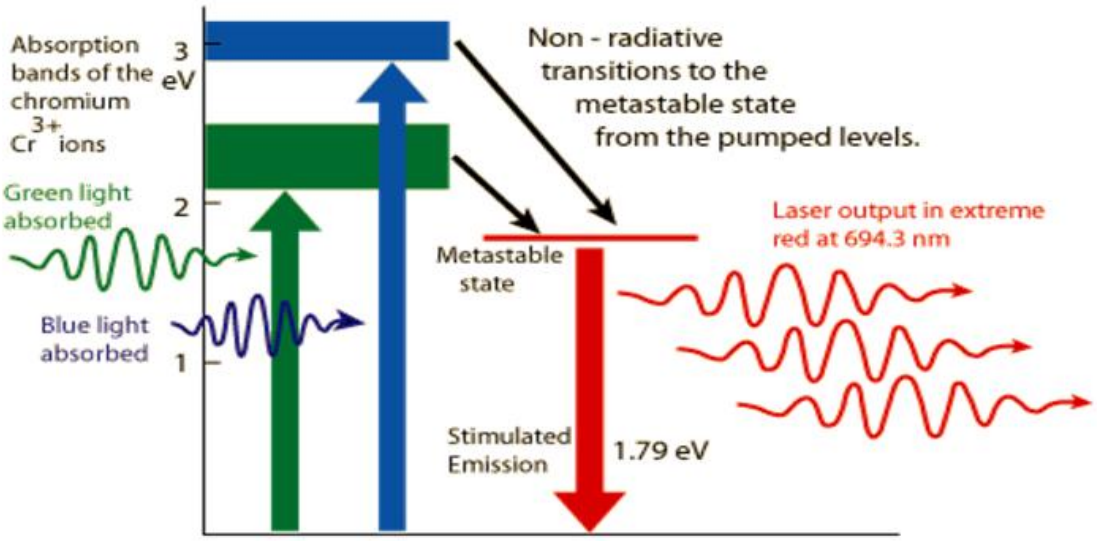

Figure 3.3: Transition Spectrum of Ruby Laser

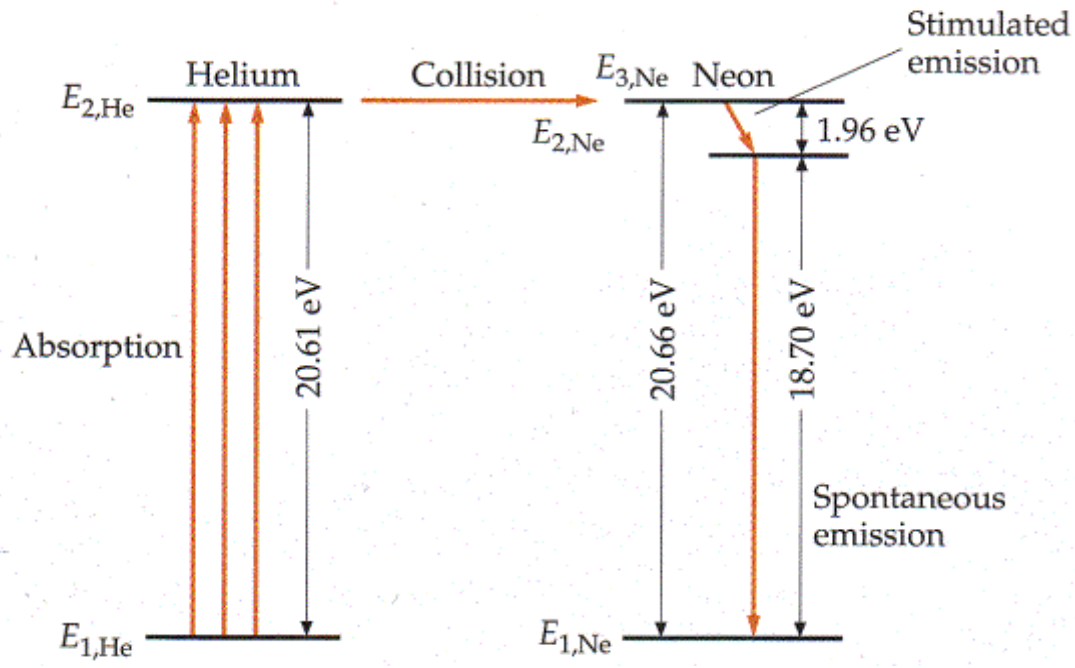

Figure 3.4: Transition Spectrum of Helium-Neon Laser

3.2. Semiconductor Laser:

Semiconductor lasers are lasers based on semiconductor gain media, where optical gain is usually achieved by stimulated emission at an interband transition under conditions of a high carrier density in the conduction band.

The physical origin of gain in a semiconductor (for the usual case of an interband transition) is illustrated in Figure 3.5. Without pumping, most of the electrons are in the valence band. A pump beam with photon energy slightly above the bandgap energy can excite electrons into a higher state in the conduction band, from where they quickly decay to states near the bottom of the conduction band. At the same time, the holes generated in the valence band move to the top of the valence band. Electrons in the conduction band can then recombine with these holes, emitting photons with energy near the bandgap energy. This process can also be stimulated by incoming photons with suitable energy. A quantitative description can be based on the Fermi–Dirac distributions for electrons in both bands.

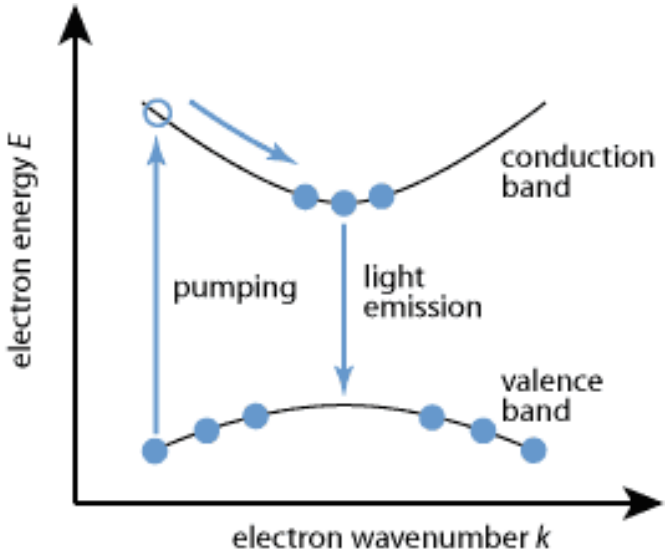

Figure 3.5: Physical gain in Semiconductor

Most semiconductor lasers are laser diodes, which are pumped with an electrical current in a region where an n-doped and a p-doped semiconductor material meet. However, there are also optically pumped semiconductor lasers, where carriers are generated by absorbed pump light, and quantum cascade lasers, where intraband transitions are utilized.

Direct bandgap energy semiconductors exhibit light emission property, which cannot be possible efficiently in an indirect bandgap semiconductor. The E-k diagrams of direct and indirect bandgap semiconductors are shown in figure 3.6(a) and 3.6(b) respectively. In direct bandgap semiconductor, the energy of conduction band minima and valence band maxima lies in the same momentum (k) plane. Thus, only a photon incident at energy greater than the bandgap energy of the semiconductor will make stimulated emission of atoms and hence, emission will occur corresponding to the bandgap energy. On the contrary, in an indirect bandgap semiconductor, the conduction band minima and valence band maxima do not lie in same k-plane. Thus, a third-particle interaction is necessary for satisfaction of the lasing criteria. The electrons should be first energized to a position in k-plane having the valence band maxima and thereafter the stimulated emission occurs. Thus, the efficiency will decrease to maintain the laws

of conservations of momentum and energy. Due to this, semiconductors like silicon or germanium being indirect bandgap semiconductor do not emit light.

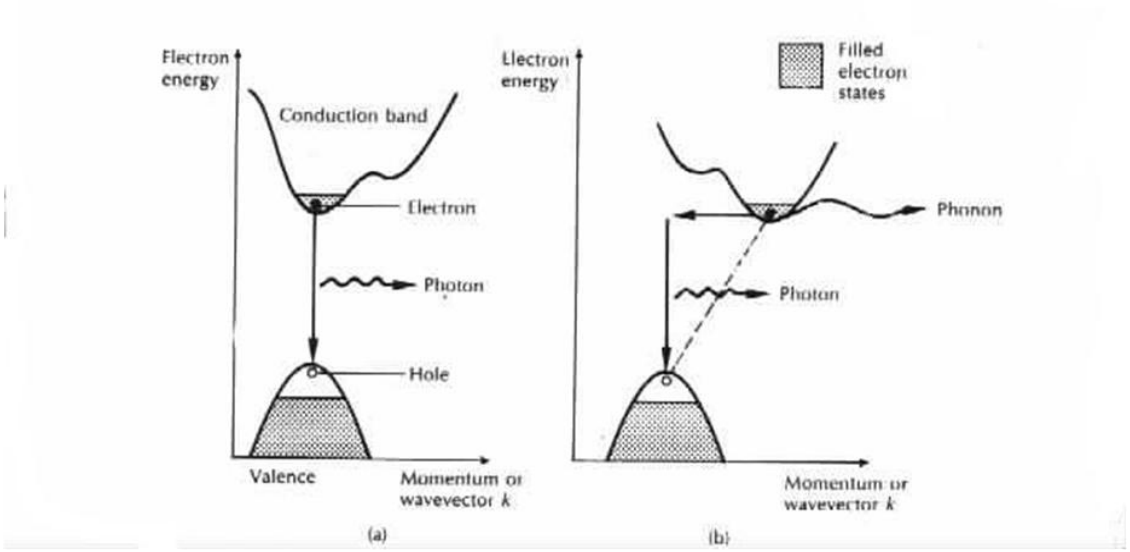

Figure 3.6(a): Direct Bandgap Semiconductor

Figure 3.6(b): Indirect Bandgap Semiconductor

The mostly used materials for optoelectronic devices are compounds of semiconductors. Usually, they are III-V semiconductors or their derivatives e.g. GaAs, GaP, $GaAs_xP_{1-x}$ which is the derivative of GaAs and GaP, x being the mole fraction. The bandgap energy of GaAs is 860 nm while that of GaP is 549 nm. So, the bandgap energy of $GaAs_xP_{1-x}$ lies between 549 and 860 nm, depending upon the value of x.

Laser diodes are designed to emit light either from their edge or their surface, the later providing a circular beam that couples better with the round core of the fiber. These are edge-emitting laser and surface-emitting laser respectively, depending upon the emission position. A laser diode, like many other semiconductor devices, is formed by doping a very thin layer on the surface of a crystal wafer. The crystal is doped to produce an n-type region and a p-type region, one above the other, resulting in a p-n junction, or diode. As in other diodes, when this structure is forward biased, holes from the p-region are injected into the n-region, where electrons are the majority carrier. Similarly, electrons from the n-region are injected into the p-region, where holes are the majority carrier. When an electron and a hole are present in the same region, they may recombine by spontaneous emission—that is, the electron may re-occupy the energy state of the hole, emitting a photon with energy equal to the difference between the electron and hole states involved. These injected electrons and holes represent the injection current of the diode, and spontaneous emission gives the laser diode below lasing threshold similar properties to an LED. Spontaneous emission is necessary to initiate laser oscillation, but it is a source of inefficiency once the laser is oscillating. Under suitable conditions, the electron and the hole may coexist in the same area for quite some time (on the order of microseconds) before they recombine. Then a nearby photon with energy equal to the recombination energy can cause recombination by stimulated emission. This generates another photon of the same frequency, travelling in the same direction, with the same polarization and phase as the first photon. This means that stimulated emission causes gain in an optical wave (of the correct wavelength) in the injection region, and the gain increases as the number of electrons and holes injected across the junction increases.

The gain region is surrounded with an optical cavity to form a laser. In the simplest form of laser diode, an optical waveguide is made on that crystal surface, such that the light is confined to a relatively narrow line. The two ends of the crystal are cleaved to form perfectly smooth, parallel edges, forming a Fabry-Perot resonator. Photons emitted into a mode of the waveguide will travel along the waveguide and be reflected several times from each end face before they are emitted. As a light wave passes through the cavity, it is amplified by stimulated emission, but light is also lost due to absorption and by incomplete reflection from the end facets. Finally, if there is more amplification than loss, the diode begins to lase.

Some important properties of laser diodes are determined by the geometry of the optical cavity. Generally, in the vertical direction, the light is contained in a very thin layer, and the structure supports only a single optical mode in the direction perpendicular to the layers. In the lateral direction, if the waveguide is wide compared to the wavelength of light, then the waveguide can support multiple lateral optical modes, and the laser is known as "multi-mode". These laterally multi-mode lasers are adequate in cases where one needs a very large amount of power, but not a small diffraction-limited beam; for example in printing, activating chemicals, or pumping other types of lasers. In applications where a small focused beam is needed, the waveguide must be made narrow, on the order of the optical wavelength. This way, only a single lateral mode is supported and one ends up with a diffraction limited beam. Such single spatial mode devices are used for optical storage, laser pointers, and fiber optics. These lasers may still support multiple longitudinal modes, and thus can lase at multiple wavelengths simultaneously.

The wavelength emitted is a function of the band-gap of the semiconductor and the modes of the optical cavity. In general, the maximum gain will occur for photons with energy slightly above the band-gap energy, and the modes nearest the gain peak will lase most strongly. If the diode is driven strongly enough, additional side modes may also lase. Some laser diodes, such as most visible lasers, operate at a single wavelength, but that wavelength is unstable and changes due to fluctuations in current or temperature.

Due to diffraction, the beam diverges (expands) rapidly after leaving the chip, typically at 30 degrees vertically by 10 degrees laterally. A lens must be used in order to form a collimated beam like that produced by a laser pointer. If a circular beam is required, cylindrical lenses and other optics are used. For single spatial mode lasers, using symmetrical lenses, the collimated beam ends up being elliptical in shape, due to the difference in the vertical and lateral divergences. This is easily observable with a red laser pointer.

Semiconductor lasers have some unique advantages over the solid-state lasers or gas lasers. These are:

- They are capable to work under any environmental conditions.
- They require very low power.
- They can be easily fabricated and thus can be used for large scale production.
- They are cheaper.
- They possess high modulation bandwidths ~ GHz.

3.3. Characteristics of a Semiconductor Laser:

There are five types of characterizations possible in a laser diode. These are Electrical (Light Output Power, Photodiode Monitor Current), Spatial (Output Light Intensity profile in far and near field and pointing angle of radiation pattern), Spectral (Spectral Width and Mode Structure observation), Optical (Astigmatism) and Dynamic (Noise, Intermodulation Distortion, Rise time, Fall time, chirping).

The most important and common characteristics is P-I curve, as shown in figure 3.7, where the output light intensity is plotted against the drive current to laser to obtain the operating point and threshold current.

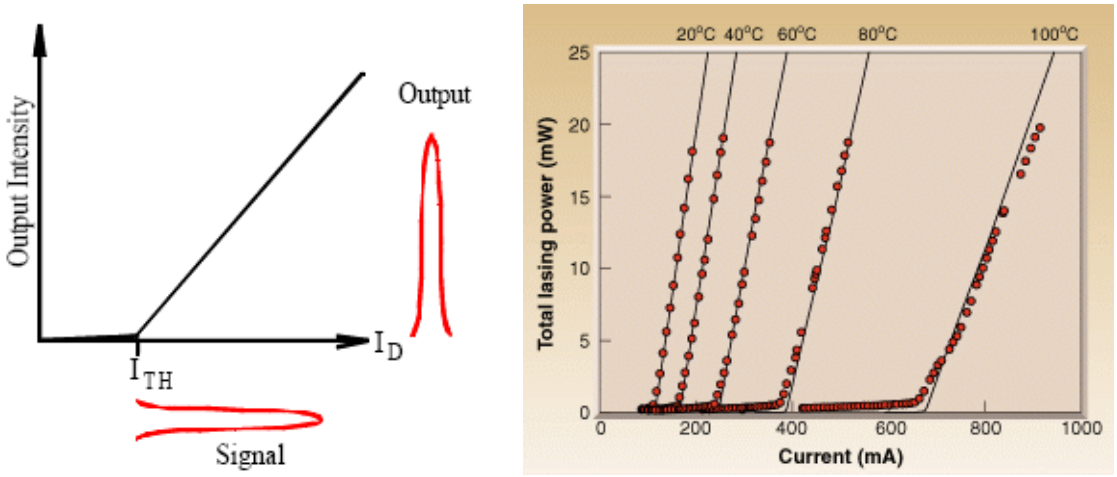

Figure 3.7: P-I Characteristics of a Semiconductor Laser at Different Temperatures

The laser threshold current I_{Th} is determined from the laser temperature T. I_{Th} can be found out to increase exponentially with T as given by equation 3.1, where T_0 is characteristic temperature of laser (~ 60 to 150 Kelvin) and μ is a constant depending upon the property of the material.

$$I_{Th} = \mu \exp(\frac{T}{T_0}) \qquad (3.1)$$

From the P-I curve, the slope efficiency can be found out in the linear region of the curve, expressed in unit of $mWmA^{-1}$. Also, the laser efficiency falls with the increase of T.

Apart from the electrical characteristics of a laser, spectral characteristics are very important to determine spectral width, tenability and mode hopping of the laser. The spectral width should be as less as possible. Due to the change in temperature, the bandgap will change to give rise to a change in peak wavelength of cavity gain. The allowed longitudinal mode can shift due to variation of the cavity length of laser with drive current. The current density in laser junction and instantaneous junction temperature change the refractive index of junction material to change effective cavity length. In single-longitudinal mode lasers, the tuning effects may give rise to mode hopping, which can be very difficult to deal with. The gain curve of a laser diode is shown in figure 3.8, where λ_p is the peak wavelength.

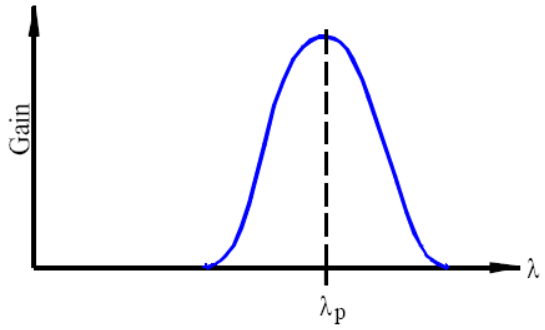

Figure 3.8: Gain-Wavelength Characteristics of a Semiconductor Laser

3.4. Different Types of Semiconductor Lasers:

There are different types of semiconductor lasers which are used in practice are described below.

3.4.1. Double Heterostructure (DH) Lasers:

In a double heterostructure (DH) laser, a small bandgap material is sandwiched between two materials of larger bandgap as shown in figure 3.9. One of the common DH lasers is composed of GaAs and $Al_xGa_{1-x}As$, where GaAs is a low bandgap material and it is sandwiched between two high bandgap materials made up of $Al_xGa_{1-x}As$. Each of the junctions between different bandgap materials is called a heterostructure, hence the name double heterostructure laser or DH laser. The advantage of a DH laser is that the region where free electrons and holes exist simultaneously, known as the active region, is confined to the thin middle layer. This means that many more of the electron-hole pairs can contribute to amplification—not so many are left out in the poorly amplifying periphery. In addition, light is reflected from the heterojunction; hence, the light is confined to the region where the amplification takes place.

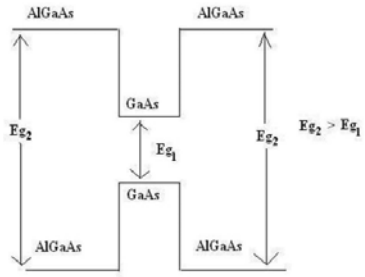

Figure 3.9: Double Heterostructure Semiconductor Laser comprising GaAs and AlGaAs

3.4.2. Quantum Well (QW) Lasers:

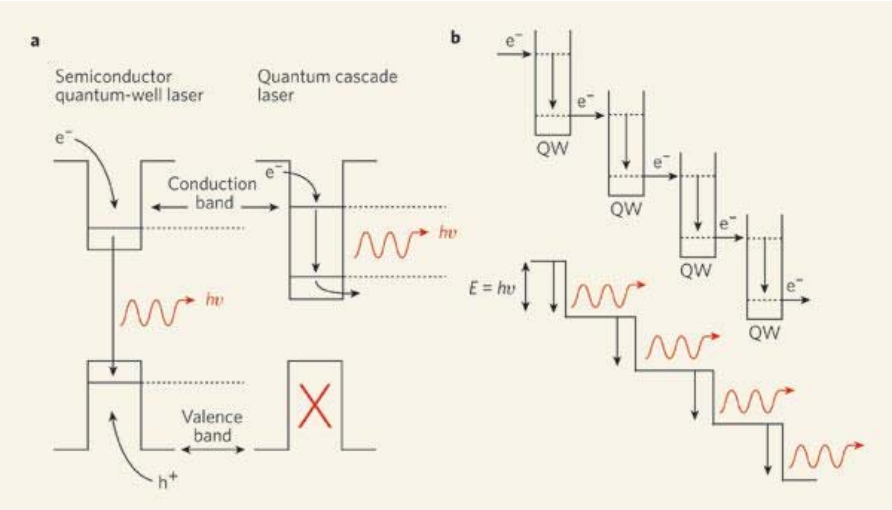

Figure 3.10(a): Quantum Well Laser **Figure 3.10(b): Quantum Cascade Laser**

If the middle layer is made thin enough, it acts as a quantum well. This means that the vertical variation of the electron's wavefunction, and thus a component of its energy, is quantized. The efficiency of a quantum well laser is greater than that of a bulk laser because the density of states function of electrons in the quantum well system has an abrupt edge that concentrates electrons in energy states that contribute to laser action. Lasers containing more than one quantum well layer are known as multiple quantum well lasers. Multiple quantum wells improve the overlap of the gain region with the optical waveguide mode. The quantum well laser and quantum cascade laser is shown in figure 3.10.

1. 3.4.3. Vertical Cavity Surface Emitting Lasers (VCSEL):

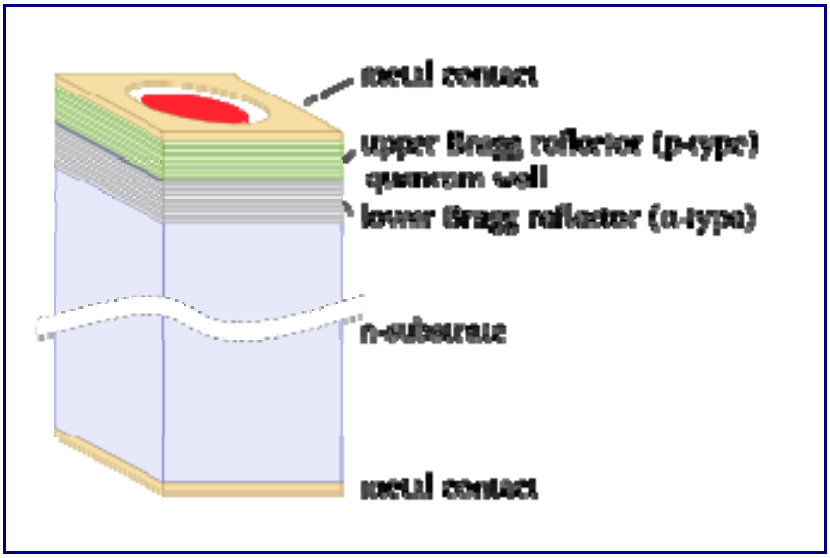

Figure 3.11: Diagram of a simple VCSEL structure

Vertical-cavity surface-emitting lasers (VCSELs) have the optical cavity axis along the direction of current flow rather than perpendicular to the current flow as in conventional laser diodes. The structure of a VCSEL is shown in figure 3.11. The active region length is very short compared with the lateral dimensions so that the radiation emerges from the surface of the cavity rather than from its edge. The reflectors at the ends of the cavity are dielectric mirrors made from alternating high and low refractive index quarter-wave thick multilayer.

There are several advantages to produce VCSELs compared to the production process of edge-emitting lasers. Edge-emitters cannot be tested until the end of the production process. If the edge-emitter does not work, whether due to bad contacts or poor material growth quality, the production time and the processing materials have been wasted. Additionally, because VCSELs emit the beam perpendicular to the active region of the laser as opposed to parallel as with an edge emitter, tens of thousands of VCSELs can be processed simultaneously on a three inch Gallium Arsenide wafer. Furthermore, even though the VCSEL production process is more labor and material intensive, the yield can be controlled to a more predictable outcome. But, due to the large ohmic resistances encountered by the injected current, considerable heating of the device occurs, needing of efficient thermal cooling thus becomes obvious. VCSELs can be operated at room temperature for 1300 nm wavelength only. VCSEL can operate at 1300 nm for single-mode fiber only.

3.4.4. Fabry Perrot (FP) Lasers:

A Fabry Perrot laser is a linear optical resonator (or cavity) which consists of two highly reflecting mirrors (with some small transmittivity) and is often used as a high-resolution optical spectrometer. One exploits the fact that the transmission through such a resonator exhibits sharp resonances and is very small between those. It consists of two planar mirrors, but the term is frequently also used for resonators with curved mirrors. From a theoretical viewpoint, plane–plane optical resonators are special in the sense that their resonator modes extend up to the edges of the mirrors and experience some diffraction losses. However, Fabry Perrot interferometers are usually used with input beams of much smaller diameter, which are actually not really matched to the resonator modes. For the usually small mirror spacing, where diffraction within a round trip is weak, this deviation is not very important.

A Fabry Perrot laser can simultaneously oscillate in several longitudinal modes. So, it is a multiple longitudinal mode (MLM) laser. The spectral width is slightly larger for this laser (~ 10 nm). The output spectrum and transmittivity are shown in figure 3.12 and figure 3.13 respectively.

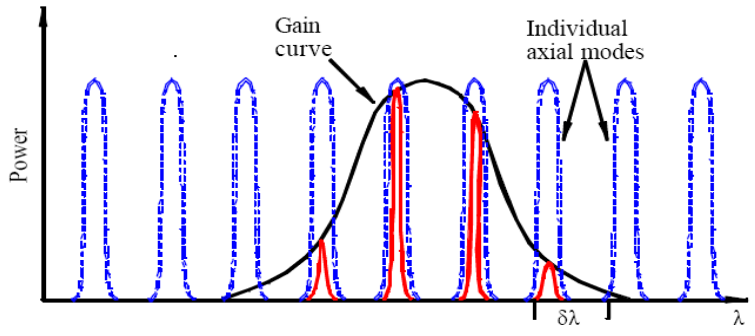

Figure 3.12: Output Spectrum of Fabry Perot Laser as a combination of gain curve and Cavity axial modes

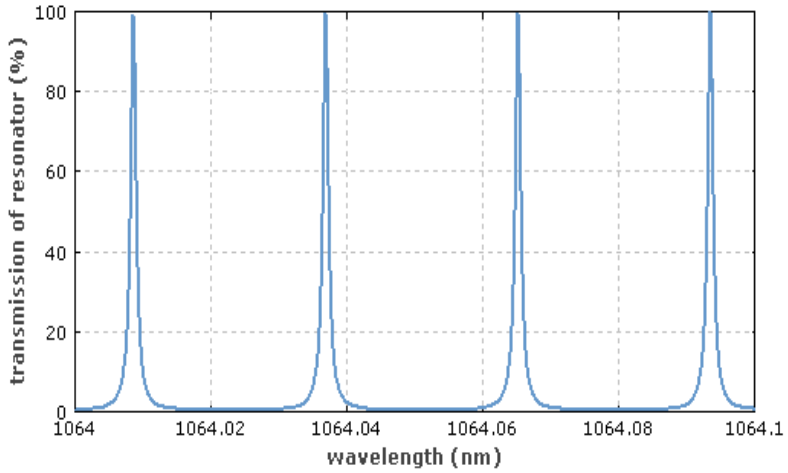

Figure 3.13: Frequency-dependent transmission of a linear Fabry–Perrot cavity with mirror Reflectivities of 90%

3.4.5. Distributed Feedback (DFB) Lasers:

A distributed-feedback laser is a laser where the whole resonator consists of a periodic structure, which acts as a distributed reflector in the wavelength range of laser action, and contains a gain medium. Typically, the periodic structure is made with a phase shift in its middle. This structure is essentially the direct concatenation of two Bragg gratings with internal optical gain. A schematic diagram of a DFB laser is shown in figure 3.14. The incident wave undergoes a series of reflections in the corrugated section of the cavity. Each of these reflected waves interfere constructively according to Bragg's law of diffraction, stating that the transmitted waves add in phase if the period of corrugation is half of the integral multiple of the wavelength. Therefore, single-frequency operation is often easily achieved, despite of spatial hole burning due to the standing-wave pattern in the gain medium. Due to the large free spectral range, wavelength tuning without mode hops may be possible over a range of several nanometers. However, the tuning range may not be as large as for a distributed Bragg reflector laser. For CW operation, the line width is 100 KHz whereas for modulated applications, the line width is 0.1 nm and thus, it can be used for any high-speed transmission.

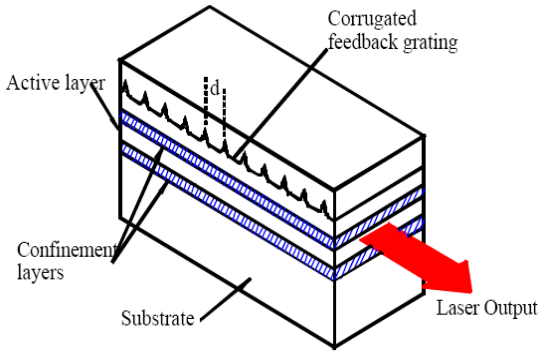

Figure 3.14(a): Structure of a DFB Laser

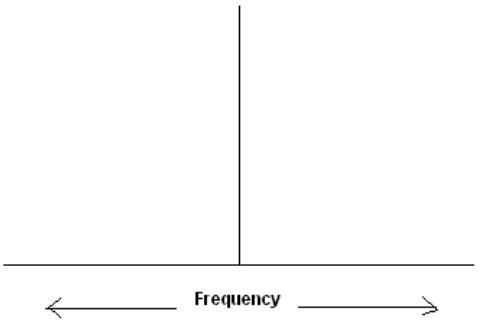

Figure 3.14(b): Spectrum of a DFB Laser

DFB lasers are more complex to fabricate than FP lasers and hence are expensive. Reflections into a DFB Laser can cause its wavelength and power to fluctuate and are prevented by packaging the Laser with an isolator in front of it. The Laser is also packaged with a Thermoelectric cooler (TE) and a monitor photodetector attached to its rear facet. The TE cooler is necessary to maintain the laser at a constant operating temperature to prevent its wavelength from drifting. The temperature sensitivity of a DFB laser operating in the 1550 nm wavelength region is about 0.1 nm/˚C. The Photodetector monitors the optical power leaking out of the rear facet, which is proportional to the optical power coming out of the laser.

3.4.6. Distributed Bragg Reflector (DBR) Lasers:

These lasers are also single mode lasers and work over the same principle like DFB lasers. But the only difference between DFB laser and DBR laser is that in DFB laser the corrugation in within the gain medium along its length while in DBR lasers the corrugation is outside the gain region. The structure of a DBR laser is shown in figure 3.15. The main advantage of DBR lasers is that the gain region is decoupled from the wavelength selection region. Thus it is possible to control both regions independently. For example, by changing the refractive index of the wavelength selection region, the laser can be tuned to a different wavelength without affecting its other operating parameters. Due to the larger laser length, it can generate high power with greater efficiency and narrower bandwidth.

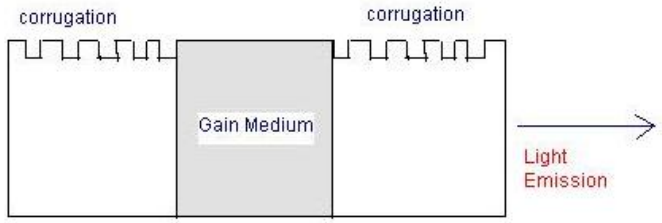

Figure 3.15: Structure of a DBR Laser

3.4.7. External Cavity Lasers (ECL):

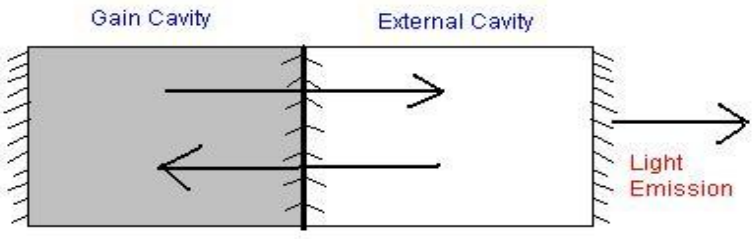

Figure 3.16: Structure of an ECL

Suppression of oscillation at more than one longitudinal mode can also be achieved by using another cavity, called the external cavity, following the primary cavity where gain occurs. This is illustrated in figure 3.16. Just as the primary cavity ha resonant wavelengths, so does the external cavity. This effect can be achieved by using reflecting facets or corrugation for the external cavity as well. The net result of having an external cavity is that the laser is capable of oscillating only at those wavelengths that are resonant wavelengths of both the primary and external cavity. By suitable design of both the cavities, it can be ensured that only one wavelength in the gain bandwidth of the primary cavity satisfies this condition. Thus the Laser oscillation can be confined to a single-Longitudinal mode.

3.5. Modulation in Semiconductor Lasers:

There are different types of modulations imposed upon semiconductor lasers. By modulation, data has been imposed upon the light stream [3]. The widely use simplest modulation scheme is on-off keying (OOK), where the light stream is turned on and off, depending upon the data bit to be 1 or 0. The OOK modulated signal is realized by two ways, either by direct modulation of the laser or by the use of external modulator.

3.5.1. Direct Modulation:

In direct modulation, the semiconductor laser is directly modulated by a modulated signal. The scheme is shown in figure 3.17. The drive current into the semiconductor is well above threshold for 1 bit.

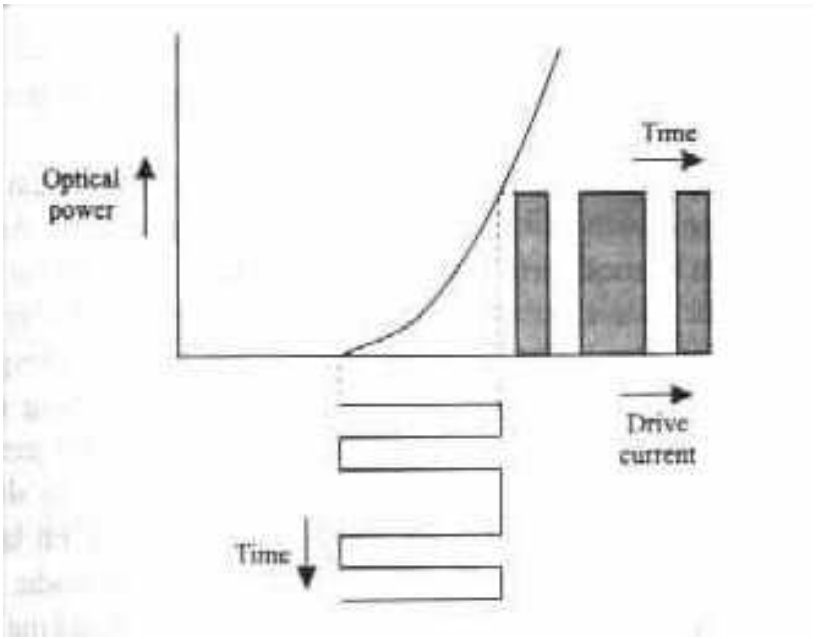

Figure 3.17: Direct Modulation of a Semiconductor Laser

There are salient characteristics of direct modulated laser. These are:

- This is simple type of modulation and also inexpensive since except light source itself, no other components are required. Semiconductor lasers can be modulated externally. Other types of lasers are CW type and cannot be directly modulated e.g., Erbium lasers cannot

be directly modulated even though at a speed of a few kbps due to larger lifetime of Erbium atoms at the metastable state.

- Due to the time variation of the carrier frequency of the transmitted pulse, there is broadening of the transmitted spectrum. This is known as frequency chirp. In direct modulation, the modulated pulses are chirped. Chirping can be reduced by increase of power of a 0 bit so that the laser is always above threshold.
- Due to the low optical power, the fibers non-linearities do not come into play as well as the photodiode in the receiver do not get saturated.
- Noise figure increases with increase in optical power while the gain remains constant.
- The frequency response for small-signal amplitude modulation of a laser diode is shown in figure 3.18. The modulation response is uniform over a large frequency range. The response peaks at the upper end of the range and thereafter decreases with frequency rapidly above the peak. As the laser bias is increased above threshold, the frequency of the peak response increases. The peak is referred to as the relaxation resonance. This suggests that there must be two coupled sources of energy storage. In any laser, one of the stored energies is due to collection of injected carriers, while the other is collection of photons in the cavity. Since the stimulated photons in laser cavity come from injected carriers, the two pools of stored energy are coupled. The probability of stimulated emission can be increased by a step increase in number of injected carriers via a step increase in the laser bias current.

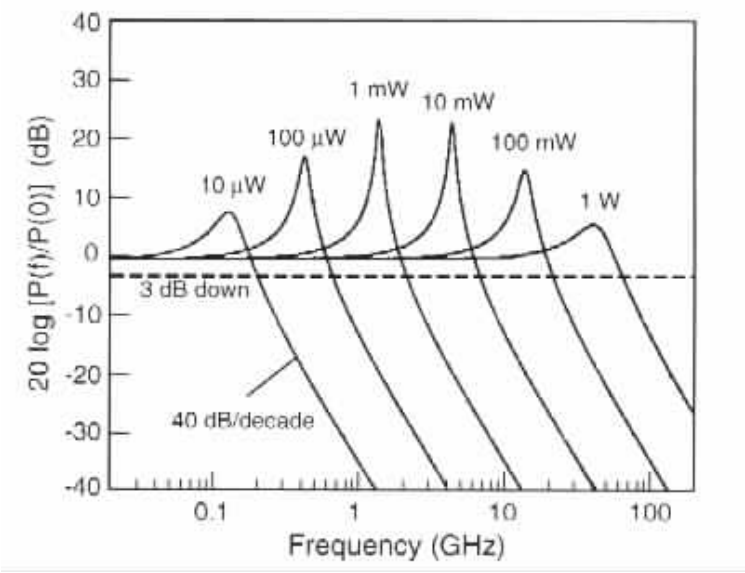

Figure 3.18: Frequency Response of a Semiconductor Laser for different Optical Power

3.5.2. External Modulation:

In external modulation of a laser, the modulator is placed in front of a light source and turns the light signal on or off based upon the data transmission. The light source is itself continuously operated. The scheme is shown in figure 3.19. But here we don't vary the drive current for varying the output intensity of the overall Laser. But instead of this we allow the

optical output from the Laser to pass through a specially designed device known as external Modulator and then vary the final optical output intensity by the application of electric field.

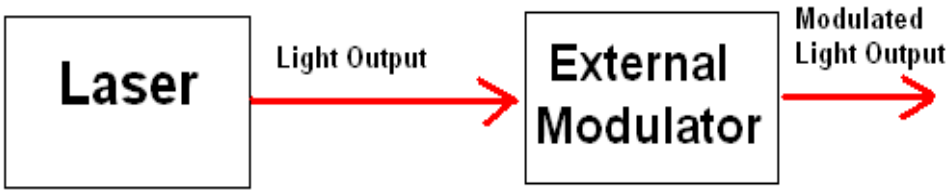

Figure 3.19: External Modulation of a Semiconductor Laser

These are essential to transmit using solitons or return-to-zero (RZ) modulations. A mode-locked laser followed by an external modulator is used to generate a train of modulated RZ pulses. Such a system is shown in figure 3.20. The output contains the periodic pulses only when the modulator input is 1.

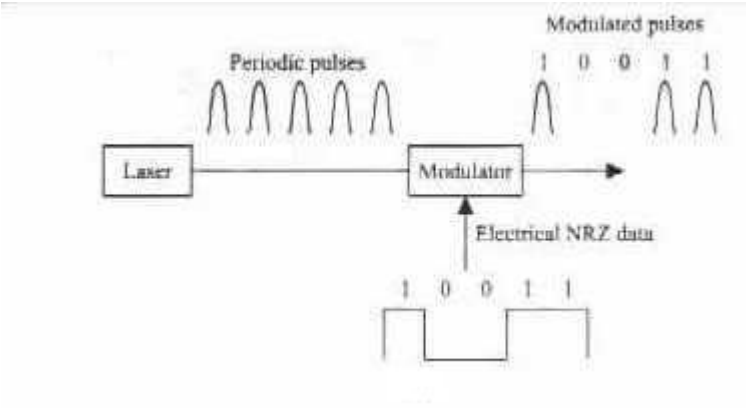

Figure 3.20: External Modulation of a digital signal

There are two types of external modulators, namely, Electro-Optic and Electro-Absorption Modulators.

Electro-optic modulator (EOM) is an optical device in which a signal-controlled element displaying electro-optic effect is used to modulate a beam of light. The modulation may be imposed on the phase, frequency, amplitude, or direction of the modulated beam. Modulation bandwidths extending into the GHz range are possible with the use of laser-controlled modulators. Generally a nonlinear optical material (organic polymers have the fastest response rates, and thus are best for this application) with an incident static or low frequency optical field

will see a modulation of its refractive index. The modulation is performed by using Pockel cells. Due to the change in electric field strength, the refractive index of the Pockel cell changes giving rise to linear electro-optic effect. However, these devices require higher voltages. Different types of Pockel cells are shown in figure 3.21.

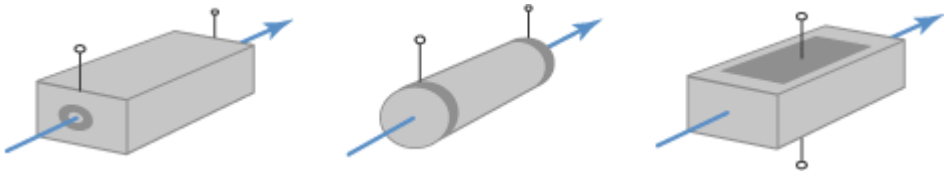

Figure 3.21: Different types of Pockel Cells

Lithium Niobate crystals are mostly used as electro-optic modulators. The device is configured as a directional coupler or a Mach-Zehnder Interferometer (MZI, figure 3.22(a)). In one state, the signals in two arms in MZI are in phase and interfere constructively to appear at output; while in other state, it is destructively interfere and hence no output (figure 3.22(b)). The overall structure of MZI is shown in figure 3.22(c) and its frequency response is shown in figure 3.22(d).

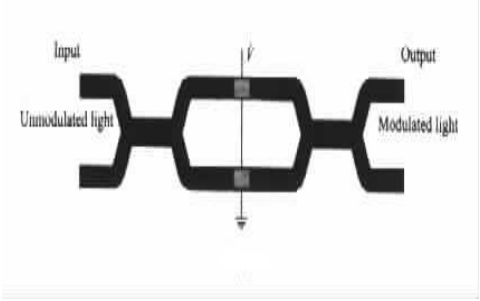

Figure 3.22(a): The MZI Configuration

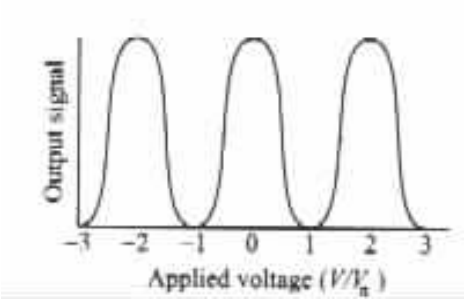

Figure 3.22(b): The MZI Response

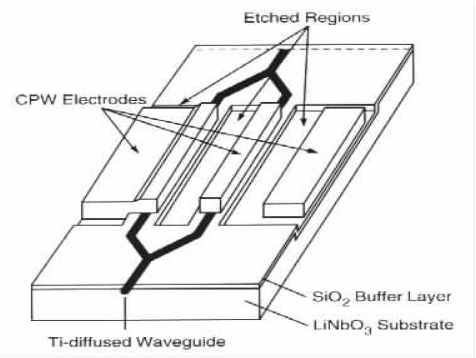

Figure 3.22(c): Structure of the MZI

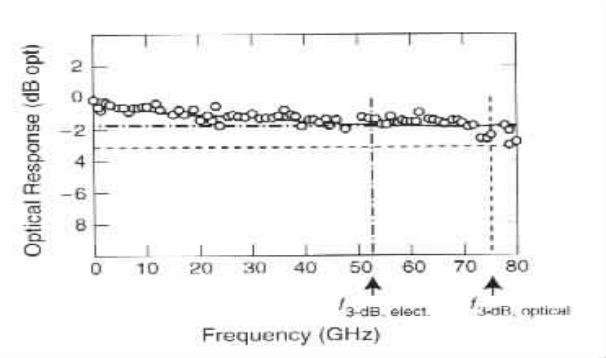

Figure 3.22(d): Frequency Response of MZI

An electro-absorption modulator (EAM) is a semiconductor device which can be used for controlling (modulating) the intensity of a laser beam via an electric voltage. Its principle of operation is based on the Franz–Keldysh effect. According to this effect, there is a change in optical absorption by a semiconductor when an electric field is applied. Since the absorption spectrum is varying, it means that the amount of energy an electron in the valence band needs to absorb to move to the conduction band also varies. This further implies that the bandgap energy of the semiconductor material changes accordingly. Now, when an electron moves back to the valence band from the conduction band, it emits energy in the form of a photon which carries energy equal to the bandgap energy for the material. Thus, if the bandgap energy is varied, the intensity of the light output can also be varied by Franz-Keldysh effect. These modulators are polarization sensitive, although integrating them on the laser chip simplifies packaging. They are made from InGaAsP semiconductors, so they can readily match laser wavelengths. Compared to EOM, they can operate at lower bias, but the chirp performance is worse and can be operated at a higher speed, making more modulation bandwidth possible. The structure is shown in figure 3.23.

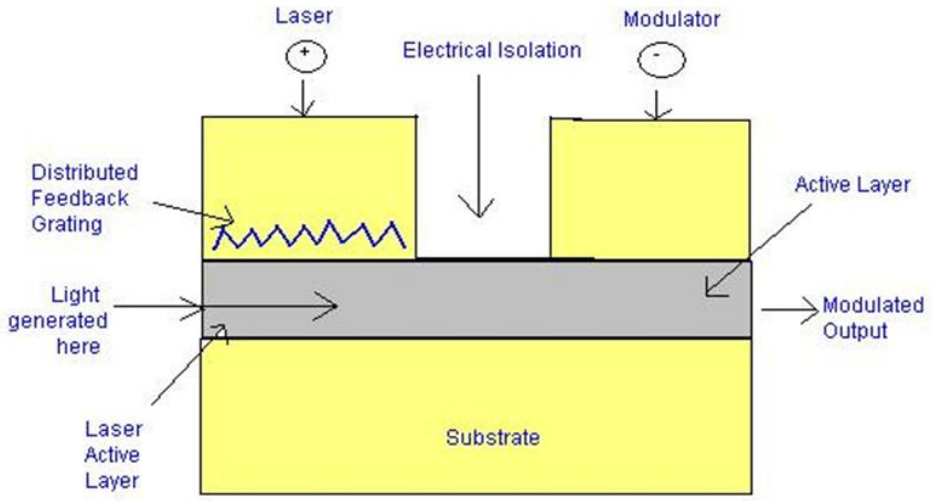

Figure 3.23: Externally Modulated Laser

There are salient characteristics of externally modulated lasers. These are mentioned as follows.

- There is no frequency chirp like the directly modulated laser.
- The system is costly.
- The non-linearity of the fiber affects the system performance.
- Photodiode saturation can be avoided by the use of optical attenuators.
- Noise Figure decreases with increase in optical power while gain increases.
- Since modulation is laser-independent, there is no bandwidth limitation.

3.6. Optical Amplifiers:

The optical amplifiers in a fiber-optic link are required to maintain the power to be detectable at the output end. The optical transmitted output is increased as in-line amplifiers or as optical pre-amplifiers of detectors, increasing in all applications the power budget of the fiber-optic network. The optical amplifiers are of three types. These are described as follows.

3.6.1. Semiconductor Optical Amplifier (SOA):

Here, amplification occurs while there is propagation through a medium fabricated in the waveguide form. It has a device length less than 1 mm. The mechanism in this case is similar to that of laser. When injected current is below threshold, then the laser acts as an optical amplifier while above threshold, it undergoes oscillation. The emission occurs between levels on lower part of the conduction band and levels on upper part of the valence band. The population inversion occurs by reverse-biased p-n junction, where the Fermi level in n-side is lower than the conduction band levels of p-side and the p-side Fermi level is lower than the valence band levels of n-side. A SOA fabricated in InP is shown in figure 3.24. There are two types of SOA. These are Fabry-Perrot Amplifiers and Travelling Wave Amplifiers.

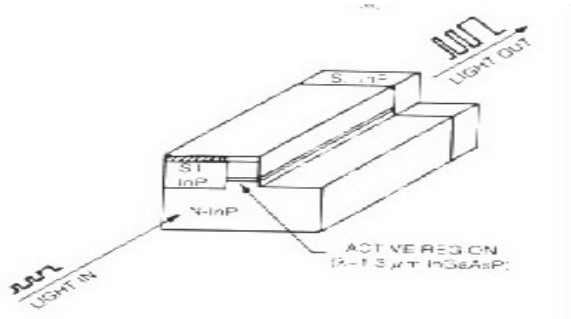

Figure 3.24: Semiconductor Optical Amplifier derived on InP substrate

3.6.2. Erbium-Doped Fiber Amplifier (EDFA):

Here, amplification occurs without conversion to the electrical domain. It consists of silica fiber is doped with rare earth metal Erbium (Er3+), which is pumped by using pump laser (operating at 980 or 1480 nm). The inputs are combined by a wavelength-selective coupler, which is shown in figure 3.25.

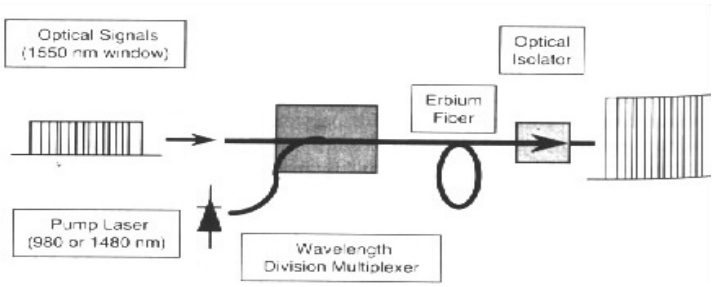

Figure 3.25: A Block Diagram of Erbium Doped Fiber Amplifier

There are certain advantages of EDFAs. These are mentioned below.

- Availability of compact and reliable high power pump laser at 980 and 1480 nm.
- The mechanism is polarization-independent and there is easy coupling for light in and light out.
- Simplicity of the device.
- There is no crosstalk for amplification of WDM signals.

There are some disadvantages of EDFAs. These are mentioned below.

- The gain is not flattened which is evident from gain-wavelength curve, which is flatter for a core mixed with Fluoride.
- This is brittle, difficult to splice and it is susceptible to moisture.

3.6.2. Raman Amplifier (RA):

Here, amplification occurs all over the frequency band as the whole medium acts as the gain medium. By injection of intense pump beam into the existing fiber, the signals can be amplified. This gain is called Raman gain. Due to this property of Raman gain, installed fibers can also be made to amplify signals by pump source into fiber span. If the pump signal is injected at the transmission span end, and is allowed to counter-propagate relative to signals, then Distributive Raman Amplification occurs. The block diagram of a RA is shown in figure 3.26.

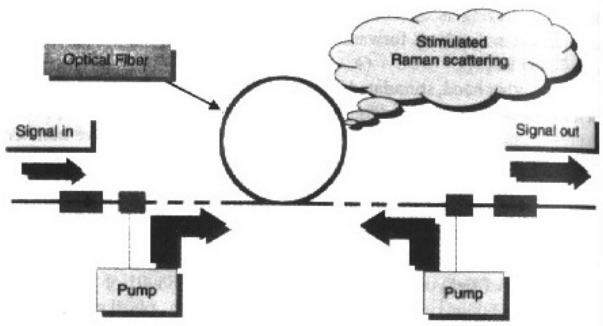

Figure 3.26: Block Diagram of a Raman Amplifier

There are three windows of the amplification band of Raman Amplifier. These are 1300, 1400 and 1500 nm. The gain is 40 dB in this region and the Noise Figure is 4.2 dB. But, there are some disadvantages of RA, which are mentioned below.

- Poor availability of ultra-high power pumping lasers in practical systems.
- DRS due to microscopic glass-composition non-uniformity.
- Short lifetime: minimum coupling chance to pump fluctuations in signal.
- Noise from ASE-ASE beating.
- Spontaneous gain of thermally induced photons in glass fiber at room temperature.

3.7. Photodetectors:

Photodetectors are devices used for the detection of light – in most cases of optical powers. These are made up of semiconductor materials as per as the emitting wavelength. Si and GaAs cannot be used as the photo detectors in 1.3 μm and 1.55 μm bands. The mostly used materials are InGaAs and InGaAsP.

Photons incident on semiconductors are absorbed by electrons in valence band. Thus, electrons, after acquiring energy, are excited into the conduction band, leaving behind a hole in valence band (vide figure 3.27). While there is an application of external voltage, the electron-hole pair recombination occurs to give rise to photocurrent. The emitted wavelength λ is dependent upon the bandgap energy E_g, as mentioned in equation 3.2, where h is Planck's constant and c is velocity of light.

$$\lambda \leq \frac{hc}{E_g} \tag{3.2}$$

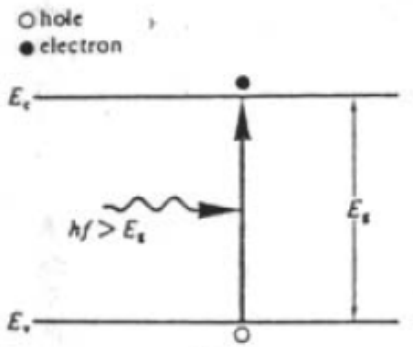

Figure 3.27: Recombination of electron-hole pair to generate photocurrent

The mostly used photo detectors are of intrinsic types due to fast response and efficient photon absorption. The intrinsic photo detectors are reverse-biased to avoid excess dark current and to reduce junction capacitance of device. The electron-hole pair generated near the junction is separated and swept under electric field, producing displacement current in external circuit, due to photon absorption along the depletion region. The depletion region is made large for absorption of maximum number of photons to absorb to create the maximum electron-hole pair. But, this limits the response speed. So, a trade-off is maintained between the number of incident photons and response speed. As the requirements for applications vary considerably concerning wavelength, maximum optical power, dynamic range, linearity, quantum efficiency, bandwidth, size, robustness and cost.

The quantum efficiency is defined as number of generated electrons with respect to number of incident photons. It is expressed by η in equation 3.3, where n_e and n_p are number of electrons generated and number of incident photons respectively.

$$\eta = \frac{n_e}{n_p} \tag{3.3}$$

The responsivity R is defined as the ratio of generated output current I_P with the incident power P_{in}, as given in equation 3.4. Its unit is AW^{-1}.

$$R = \frac{I_P}{P_{in}} \tag{3.4}$$

Since incident optical power P_{in} corresponds to an incidence of P_{in}/hf number of photons, where f be the emitted frequency, and η fraction of this number of incident photons are absorbed and generate an electron in external circuit, so R can be rewritten as in equation 3.5.

$$R = \frac{e\eta}{hf} \tag{3.5}$$

The responsivity R can also be expressed in terms of emission wavelength λ, as given by equation 3.6.

$$R = \frac{e\eta\lambda}{hf} = \frac{\eta\lambda}{1.24} AW^{-1} \tag{3.6}$$

There are two types of photodiodes, p-i-n photodiode and Avalanche Photo Diodes (APD). These are shown in figure 3.28 and 3.29 respectively.

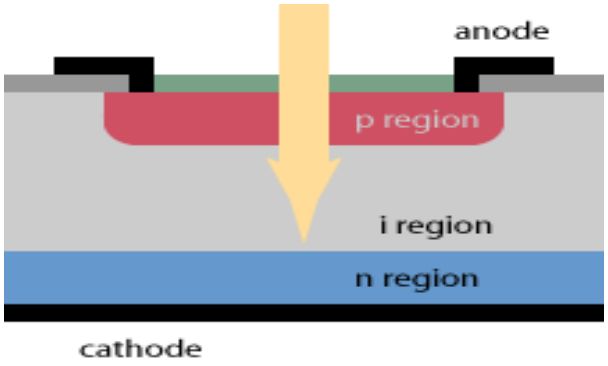

Figure 3.28: P-i-n Photodetector

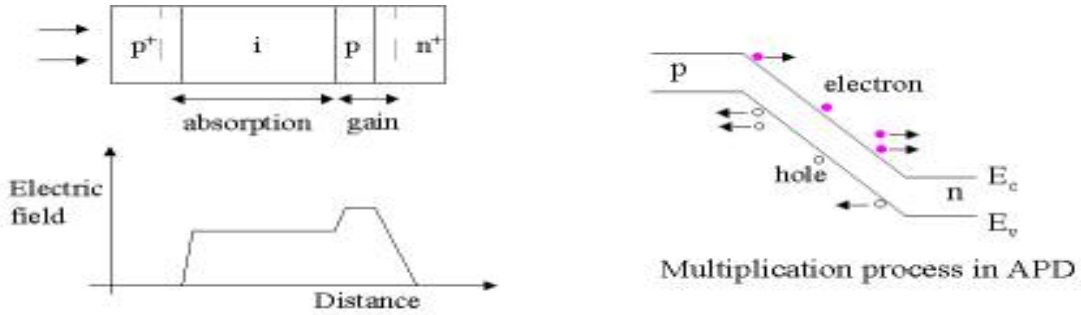

Figure 3.29: Avalanche Photodetector

In a p-i-n photodetector, an intrinsic region is sandwiched between the p-type and n-type material semiconductors. Here, the depletion region extends completely across the intrinsic semiconductor. The widths of p-type and n-type region are made small compared to that of the intrinsic region. Thus, light absorption occurs in this region, resulting in the increase of efficiency and hence, responsivity. Quaternary compounds like InGaAsP grown on InP substrate serves as a good p-i-n photodiode with dark current less than 0.2 nA and response time less than 100 ps, with quantum efficiency larger than 0.7.

In p-i-n photodiodes, one photon can generate only one electron, limiting the responsivity. If the electron generated is subjected to high electric field, it can acquire sufficient energy to knock off more electrons from the valence band to conduction band. These secondary generated electron-hole pairs can generate further electron-hole pairs and this process continues. This is called avalanche multiplication, and such a photodiode is avalanche photodiode (APD). Si and Ge APDs are used with high gain (~300). Also, quaternary III-V alloys are used.

Chapter 4

RF Over Fiber Optic Link

4.1. Mechanisms used in RF over Fiber:

In the RF over Fiber communication system, the key elements are optical sources capable of fast modulation, appropriate transmission media and fast optical detectors or optically controlled microwave devices. Here, the source can be realized by double heterostructure semiconductor devices which can operate at room temperatures continuously. Here, the direct modulation can also be done via the injected current (Ikegami and Suematsu, 1967 [22]). Here, the transmission medium is the optical fiber made up of silica. Systems migrated from graded index multimode fiber operating with GaAs/AlGaAs lasers at 850 nm wavelength is used for lower loss applications.

For RF signal propagation, there are two major limiting characteristics suffered by coaxial cables. Firstly, RF loss increases with frequency and length. Secondly, coaxial cables are limited in the length that they may be used without additional amplification (Daniel, 2000-2003 [17]). On the contrary, fiber optic cables suffer from very low losses compared to coaxial cables. The fact that RF signals are not decoupled from the Fiber Optic Cables makes them ideal while they run through the noisy environment or running long lengths parallel to other Fiber Optics in RF cables. The lack of electrical conductivity adds to the attractive applications, such as electrical utilities. These fiber optic cables are much smaller and of lighter weight than corresponding RF cables since it is non-metallic, simpler installation and easy routing. There are two different modes of fiber optic cable operation; viz., multimode & single mode. For short links, multimode fibers can be used. In shorter link, data rate is low (<100 Mbps) when compared to RF signals (100-2200 MHz). But, for longer communication links, single-mode fibers are used. These fibers possess less loss compared to those of multimode fibers.

The useful microwave bandwidth response is developed for the detection, fast depletion and avalanche detectors (Berchtold *et al*., 1975 [5]). Direct optical control of microwave devices was done earlier by tuning Gunn oscillators (Geutin, 1969 [20]), tuning and power modulation of TRAPATT (Kiehl, 1978 [25]), and tuning of IMPATT (Vyas et al., 1977 [39]) by optical illumination. Injection locking of BJT (Yen *et al*., 1977 [42]) and IMPATT oscillators (Seeds and Forrest, 1978 [34]) to intensity modulated optical signals was achieved. An edge-illuminated silicon 7.8-GHz IMPATT oscillator to a directly modulated GaAs/AlGaAs laser is done, where locking range is about 1 MHz.

4.2. Applications of RF over Fiber:

The low-loss wide-bandwidth capability of optoelectronic systems makes them attractive for the transmission and processing of the microwave signals, while the development of high-capability optical communication syste4ms has required the use of microwave techniques in optical transmitters and receivers. In this technique, optical heterodyning is one of the important tools. (Seeds, 2002 [33]) Optical heterodyning becomes an important tool for modern day communication system where RF signal is generated from optical signal. The principle is applied in various fields e.g., in Broadband Mobile Communications, in Radio Astronomical Applications, in Antenna Remoting etc...

4.2.1. Application in Broadband Mobile Communications:

In a broadband wireless access system, high transmission bandwidth is required (Qi *et al*., 2002 [30]). But, in microwave frequency range, the bandwidth is insufficient to provide mobile services, which occurs in the lower microwave region. Thus, at the upper microwave region & in mm-wave region, broadband services are introduced. Here, the propagation loss is

high as well as the traffic has been increased due to large number of subscribers under the same Base Station Controller (BSC). Thus, number of Base Stations (BTS) would be increased leading to increase of cost. (Choi *et al.,* 2005 [12]) This problem can be reduced by allowing mm-wave Radio over Fiber system to be propagated, where a number of BTS are located within the same Master Station Controller (MSC). This also compensates the transmission loss. This can be done by an optical source together with the RF sources. (Bhattacharyya *et al*., 2006 [7])

The MSC is driven by optical source and while the optical signal traverses through the optical fiber, some loss may be incurred due to chromatic dispersion of the fiber. But, when the mm-wave signals are generated at BSCs and are allowed to propagate down the optical fiber, there is no loss. Thus, the arrangement becomes simpler (Sarkar *et al*., 2006 [32]). A simplified block diagram showing the total arrangement is shown in figure 4.1.

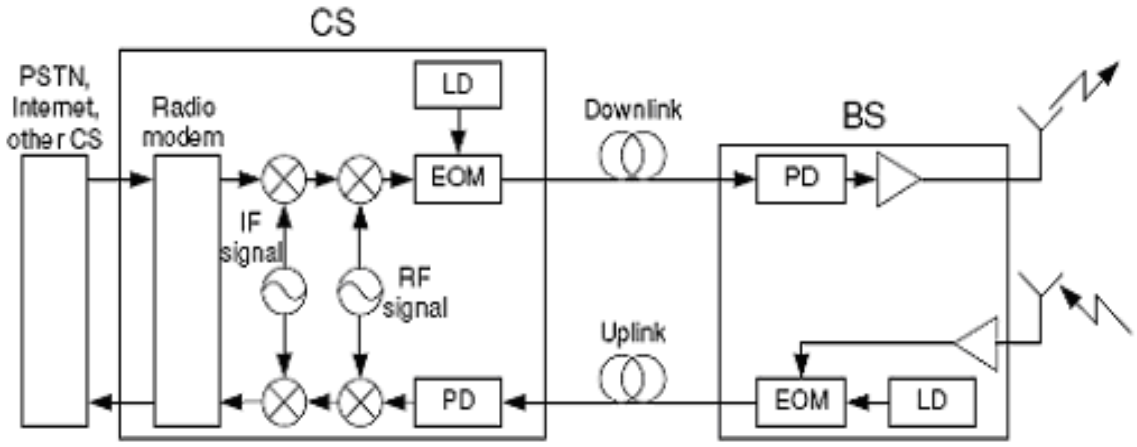

Figure 4.1: Arrangement for Broadband Mobile Access System

There are several advantages of the scheme used. These are:

- Low Noise Figure due to practically no fiber loss.
- Simple design of BTS possible.
- Insertion loss is very low.
- Can handle high powers.
- Possibility of number of subscribers maintaining the original bandwidth.

4.2.2. Application in Radio Astronomy:

Modern day Radio telescopes consist of large no. of array antennas located over tens or hundreds of kilometers. So, the RF signals received by all those remotely located antennas can be brought to the central processing facility through optical fibers because of their low loss. Also, the command and control signals for controlling these antennas and setting various parameters can be sent from the central processing facility through optical fibers. For this application, single-mode fibers are used.

4.2.3. Application in Antenna Remoting:

Metallic waveguides are lossy for the optical frequencies, but optical fibers behave as a lossless medium for propagation of optical waves. Thus, no attenuation occurs in this case. The stability and broad tenability is obtained by larger optical fiber link.

The Atacama Large Millimeter Array (ALMA) project is a large scale International Collaboration in Antenna Remoting & Radio Astronomy (Shen et al., 2002 [36]). A large-phased array system consisting of 60 movable high-gain dish antennas will be built in the Atacama Desert in Chile. The Radio Telescope is designed to operate at frequencies upto 950 GHz using high frequency mixers and the local oscillator signal is needed to drive these mixers. These mixers are very stable generating signals in mm-wave range with very narrow bandwidth (~few KHz) (Braun *et al*., 1996 [8]). Optical methods for generating this local oscillator signal are explored, including the optical heterodyning technique. A typical arrangement is shown in figure 4.2 below.

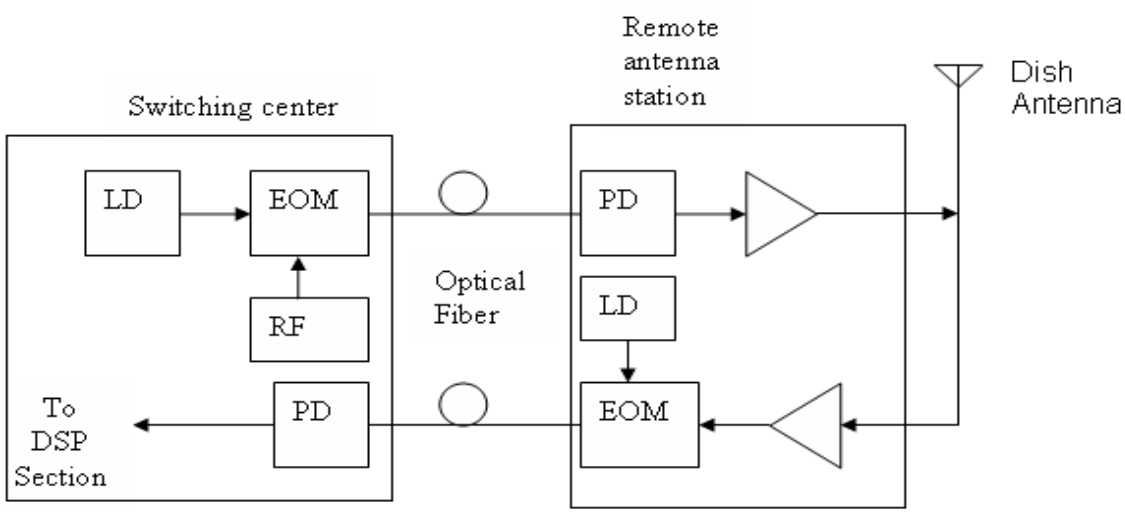

Figure 4.2: Arrangement for Antenna Remoting

4.3. Technology Used in RF over Fiber:

The simplicity of direct modulation of semiconductor lasers has led to reduce the electrical parasitic of laser structures and optimize laser parameters for high-speed operation [1]. The modulation bandwidth is limited by photon-electron resonance frequency ω_p above which the undamped detected electrical response falls as ω_m^{-4}, where ω_m is the modulating frequency, and ω_p is given in equation 4.1, where g_o is the differential gain, S_o is the mean photon density, τ_p is photon lifetime and ε is the gain compression factor.

$$\omega_p = \sqrt{\frac{g_o S_o}{\tau_p (1+\varepsilon S_o)}} \tag{4.1}$$

Thus, by reduction of photon lifetime by implementing short optical cavity and reduced facet reflectivity, the increase of the differential gain occurs by reducing dimensionality. The output power is thus increased. But, the gain compression has been valid for 1.55-μm room-temperature operation lasers to bandwidths less than 30 GHz. (Morton *et al*., 1994 [26]).

When the external modulator is used, the modulated optical power output is given in equation 4.2, where k_m is the modulation sensitivity (V^{-1}), V_i is the modulating signal voltage, and P_{op} is unmodulated optical input power.

$$P_{om} = k_m V_i P_{op} \tag{4.2}$$

Thus, if the input optical power is increased, then the l power for a given modulating signal is also increased. This leads to microwave photonic links having gain without electrical amplification (Cox *et al*., 1990 [14]).

The source can be two heterodyne sources also; which emit frequencies at ω_1, ω_2 where $|\omega_1 - \omega_2| << \omega_1, \omega_2$. If their optical fields are overlapped with common polarization, and illuminate the photodiode of responsivity R, the resulting photocurrent is (Bhattacharyya *et al*., 2007 [25]) given by equation 4.3, where P_1 and P_2 are the powers and φ_1 and φ_2 are phases of the two sources incident on the detector. The phase-noise of the heterodyning source is minimized by using an optical phase-lock loop (OPLL) (Sarkar & Kar, 2006 [32]).

$$i = R[P_1 + P_2 + 2\sqrt{P_1 P_2}\cos((\omega_1 - \omega_2)t + (\phi_1 - \varphi_2))] \tag{4.3}$$

MSM photodiodes are used as the detector in this case for its compatibility to form MMICs (Monolithic Microwave Integrated Circuits). Here, bandwidth is as large as 78 GHz (Droge *et al.,* 1998 [18]).

Optically controlled microwave devices can also be used as the detector. There are several advantages of this scheme. Firstly, no extra electronics circuitry is required to process the signal before detection. Secondly, optical control introduces extra control port to microwave devices. Finally, optical control is immune to most microwave electromagnetic disturbances.

Opto-electronic mixers are also used for the detection. Here, when optical pumped lasers are used, the signal to be converted in frequency is supplied electrically and the local oscillator signal is an intensity-modulated optical source (Gomes and Seeds, 1989 [21]). Integrating the photodetection and mixing, the electrical coupling between separate detector and mixer with consequent matching and parasitic component is not required.

4.4. Analog Fiber-Optic Link:

Technically, the analog optical links are those where the optical modulation depth is sufficiently small so that one can use incremental or small-signal models of various link devices. Usually, an analog optical fiber link is the link where analog modulation is performed over a fiber-optic link. The RF performance of analog optical links is done using same parameters that are used to characterize RF components [27].The different figure-of-merits are discussed.

4.4.1. Gain:

The link gain for a direct link is essentially the transducer power gain which is most useful for optical links. The intrinsic link gain is the transducer gain of amplifier less optical link. The link transducer power gain is expressed as the product of three separate terms, as given by equation 4.4, where G is the link transducer power gain, p_{out} is the RF power delivered to load at link output, p_{in} is the available RF power at input, p_o is fiber-coupled modulated optical power from modulating device, t_{od} is the link optical transfer frequency ($t_{od} = \frac{p_{od}}{p_o}$), and p_{od} is modulated optical power in the photodetector fiber. The optical power is squared in equation 4.4, since the considered electro-optic devices have optical power proportional to the RF voltage or current. The transfer efficiency t_{od} includes the factors affecting light transmission from modulating device to the detector. Here, the first and the third terms define the incremental modulation efficiencies, which are useful for the comparison of the performance of the several implementations of a given link function, such as source modulation.

$$G = \frac{p_{out}}{p_{in}} = \frac{p_o^2}{p_{in}} t_{od}^2 \frac{p_{out}}{p_{od}^2} \tag{4.4}$$

The link gain G_{link} is expressed as in equation 4.5, where η_l be slope efficiency of laser, R be the responsivity of the photodiode and α be the optical loss in ratio. [38]

$$G_{link} = (\frac{\eta_l \alpha R}{2})^2 \tag{4.5}$$

A practical limit of gain is set by the limits of slope efficiency and responsivity. For a link comprising of a single conventional diode laser and a p-i-n photo detector, the link gain is limited less than or equal to 1, where the laser input resistance and detector load resistance are of equal value.

The slope efficiency of an external modulator is a derived parameter. In a Mach-Zehnder modulator, the slope efficiency is given by equation 4.6, where P_I is continuous wave laser power into the modulator, T_{ff} is the fiber-to-fiber transmission of modulator, R_s be the source impedance and V_π is modulator's on-off switching voltage. Thus, from equation 4.6, it can be inferred that the slope efficiency can be improved by increasing output optical power of laser and reducing switching voltage of the modulator. Thus, higher gain requires a laser with optical power, a low-loss modulator withstanding this higher power, and a high-speed detector handling higher powers without saturation.

$$\eta_{mzi} = \frac{\pi P_I T_{ff} R_s}{2V_\pi} \tag{4.6}$$

In a broadband link, the increase of slope-efficiency increases the link gain. For a requirement of bandpass frequency response applications, it is possible to trade some bandwidth for increased response within interested domain of frequency range.

4.4.2. Noise Performance:

There are mainly three noises of a fiber-optic links. These are Laser Noise due to Relative Intensity Noise (RIN), Shot Noise and Thermal Noise due to the receiver circuitry.

Relative intensity noise (RIN) describes the instability in the power level of a laser. The noise term is important to describe lasers used in fibre-optic communication and LIDAR remote sensing. It can be generated from cavity vibration, fluctuations in the laser gain medium or simply from transferred intensity noise from a pump source. Since intensity noise typically is proportional to the intensity, the relative intensity noise is typically independent of laser power. RIN typically falls off with frequency and is a kind of pink noise. Relative intensity noise is measured by sampling the output current of a photodetector over time and transforming this data set into frequency with a fast Fourier transform. RIN is usually presented as relative noise power in decibels per hertz at one or several intensities. If the time-dependent power $P(t)$ be the sum of the with an average power $\bar{P}$ and a fluctuating power $\delta P(t)$, then RIN is described by the Power Spectral Density (PSD), as given by equation 4.7, which depends on the noise frequency f.

$$S_I(f) = \frac{2}{\bar{P}^2}\int_{-\infty}^{\infty} < P(t)P(t+\tau) > e^{i2\pi f\tau} d\tau \tag{4.7}$$

The unit of RIN PSD is Hz^{-1}, but it is generally specified in 10 times the logarithm of that quantity in $dBcHz^{-1}$. The root mean square value of the RIN is given by equation 4.8, which is in percentage.

$$\left.\frac{\delta P}{\bar{P}}\right|_{rms} = \sqrt{\int_{f_1}^{f_2} S_I(f) df} \tag{4.8}$$

The laser noise is arisen due to this RIN. The laser noise power is given by equation 4.9, where R_l be the load resistance at the receiver photodiode and I_{Ph} be the bias current above threshold as shown in equation 4.10.

$$P_{Laser} = RIN_{Laser}(\frac{I_{Ph}}{2})^2 R_l \tag{4.9}$$

$$I_{Ph} = (I_{Bias} - I_{Th})\eta_l R\alpha \tag{4.10}$$

Shot noise is a type of electronic noise that occurs when the finite number of particles that carry energy, such as electrons in an electronic circuit or photons in an optical device, is small enough to give rise to detectable statistical fluctuations in a measurement. It is important in electronics, telecommunications, and fundamental physics. It also refers to an analogous noise in particle simulations, where due to the small number of particles, the simulation exhibits detectable statistical fluctuations not observed in the real-world system. The strength of this noise increases with the average magnitude of the current or intensity of the light. However, since the magnitude of the average signal increases more rapidly than that of the shot noise, shot noise is often only a problem with small currents or light intensities. The intensity of a source will yield the *average* number of photons collected, but knowing the average number of photons which will be collected will not give the actual number collected. The actual number collected will be more than, equal to, or less than the average, and their distribution about that average will be a Poisson distribution. Since the Poisson distribution approaches a normal

distribution for large numbers, the photon noise in a signal will approach a normal distribution for large numbers of photons collected. The standard deviation of the photon noise is equal to the square root of the average number of photons. Thus, the signal-to-noise ratio is of the order of number of photons collected. Shot noise is a Poisson process and thus the current fluctuation follows Poisson distribution, as given by equation 4.11., where e be the electronic charge, Δf be the bandwidth and I be the average current. The resulting noise power P_{shot} generated by this noise current is given by equation 4.12, where I_d be the dark current of photodiode.

$$\sigma_i = \sqrt{2eI\Delta f} \tag{4.11}$$

$$P_{shot} = 2e(\frac{I_{Ph} + I_d}{2})R_l \tag{4.12}$$

Johnson–Nyquist noise (thermal noise, Johnson noise, or Nyquist noise) is the electronic noise generated by the thermal agitation of the charge carriers (usually the electrons) inside an electrical conductor at equilibrium, which happens regardless of any applied voltage. Thermal noise is approximately white, meaning that the power spectral density is nearly equal throughout the frequency spectrum (however see the section below on extremely high frequencies). Additionally, the amplitude of the signal has very nearly a Gaussian probability density function. Thermal noise is distinct from shot noise, which consists of additional current fluctuations that occurs when a voltage is applied and a macroscopic current starts to flow. For the general case, the above definition applies to charge carriers in any type of conducting medium (e.g. ions in an electrolyte), not just resistors. It can be modelled by a voltage source representing the noise of the non-ideal resistor in series with an ideal noise free resistor. The power spectral density is given by equation 4.13, where k is Boltzmann Constant, T_0 is absolute temperature of the resistor and R_1 be resistor used.

$$\sigma^2 = 4kT_0R_1 \tag{4.13}$$

The noise generated at the resistor can transfer to the remaining circuit; the maximum noise power transfer happens with impedance matching when the Thevenin's equivalent resistance of the remaining circuit is equal to the noise generating resistance. In this case the noise power transfer to the circuit per unit bandwidth is given by equation 4.14.

$$P_{Thermal} = kT_0 \tag{4.14}$$

The total noise power is given by the summation of three noise powers, i.e., laser noise, shot noise and thermal noise, as given by equation 4.15.

$$P_{Total} = P_{Laser} + P_{shot} + P_{Thermal} \tag{4.15}$$

The equivalent input noise (EIN) is the output noise of a system or device referred to the input. It is done by modelling the object as a noise-free device with an input noise generator equal to the output noise divided by the system or device gain. Thus, in decibel-scale, the link gain is subtracted from the total noise floor level to have the net EIN. [34] The expression of the EIN is given by equation 4.16.

$$EIN_{link} = \frac{P_{Total}}{G_{link}} \tag{4.16}$$

4.4.3. Noise Figure:

The noise figure (NF) is the ratio of the output noise power of a device to the portion thereof attributable to thermal noise in the input termination at standard noise temperature T_0 (usually 290 K). The noise figure is thus the ratio of actual output noise to that which would remain if the device itself did not introduce noise. It is a number by which the performance of a radio receiver can be specified.

In heterodyne systems, output noise power includes spurious contributions from image-frequency transformation, but the portion attributable to thermal noise in the input termination at standard noise temperature includes only that which appears in the output via the principal frequency transformation of the system and excludes that which appears via the image frequency transformation. Essentially, the noise figure is the difference in decibels (dB) between the noise output of the actual receiver to the noise output of an "ideal" receiver with the same overall gain and bandwidth when the receivers are connected to sources at the standard noise temperature T_0 (usually 290 K). It is also defined as the ratio of input signal-to-noise ratio (SNR_i) to output signal-to-noise ratio (SNR_o), as given by equation 4.17. The signal-to-noise ratio of a link is the measurement of signal power with respect to the noise power. SNR is usually expressed in dB, where it signifies the amount of signal power is above the noise level.

$$F = \frac{SNR_i}{SNR_o} \tag{4.17}$$

In a link, if the noise figure is F, and the input noise power is N_{in}, then the generated noise power in the device N_{ckt} will be given in equation 4.18 below.

$$N_{ckt} = (F-1)N_{in} \tag{4.18}$$

Similarly, the noise temperature at output T_{noise} will be given as in equation 4.19 below, where T_0 is the ambient temperature of 290K.

$$T_{noise} = (F-1)T_0 \tag{4.19}$$

If there are n no. of amplifiers in a link of gains G_1, G_2, G_3,G_n respectively and the noise figures of the stages are F_1, F_2, F_3, ..F_n respectively and of noise equivalent temperatures T_1, T_2, T_3,T_n respectively, then the equivalent noise figure F_{eq} and the equivalent noise temperature T_{eq} are given as in equations 4.20 and 4.21 respectively.

$$F_{eq} = 10\log(F_1 + \frac{F_2 - 1}{G_1} + \frac{F_3 - 1}{G_1 G_2} + ... + \frac{F_n - 1}{G_1 G_2 .....G_{n-1}}) \tag{4.20}$$

$$T_{eq} = T_1 + \frac{T_2}{G_1} + \frac{T_3}{G_1 G_2} + ... + \frac{T_n}{G_1 G_2 .....G_{n-1}}) \tag{4.21}$$

The noise figure in dB in terms of EIN can be defined as in equation 4.22, [38] where EIN_{link} is expressed in $dBmHz^{-1}$.

$$NF_{link} = EIN(dBmHz^{-1}) + 174 \tag{4.22}$$

When there are pre-amplifiers and post-amplifiers in the link, then the total noise figure of the link is determined essentially by the noise figure of the first stage, as given by equation 4.23, where NF_{link} is the noise figure of the link, NF_{total} is the total noise figure, $NF_{pre-amp}$ and $NF_{post-amp}$ are the noise figures of pre-amplifier and post-amplifier respectively, $G_{pre-amp}$ and G_{link} are gains of the pre-amplifier and link respectively.

$$NF_{total} = NF_{pre-amp} + \frac{NF_{link} - 1}{G_{pre-amp}} + \frac{NF_{post-amp} - 1}{G_{pre-amp} G_{link}} \tag{4.23}$$

For attenuator having attenuation L and the physical temperature T_{phys}, the noise figure F is given by equation 4.24, where T_o is the ambient temperature of 290 Kelvin.

$$F = 1 + \frac{(L-1)T_{phys}}{T_o} \tag{4.24}$$

There are two ways to achieve low noise-figure. Firstly, an intrinsic link can be designed to have low noise figure. Secondly, the intrinsic link can be augmented with a low-noise pre-amplifier to have low noise figure. But, the high-gain pre-amplifier should have a high intercept point to avoid the degradation of the spurious-free dynamic range. But, in practice, the link with high-gain and low noise figure may be unavailable for link with broad bandwidth. [40]

4.4.4. Linearity Characterization:

In a link, the important factors for the measure of linearity are 1-dB compression point (Raut & Praveenkumar, 2001 [29]), third order intercept point and the spurious free dynamic range (SFDR). These can be explained with the help of figure 4.3 and figure 4.4 respectively.

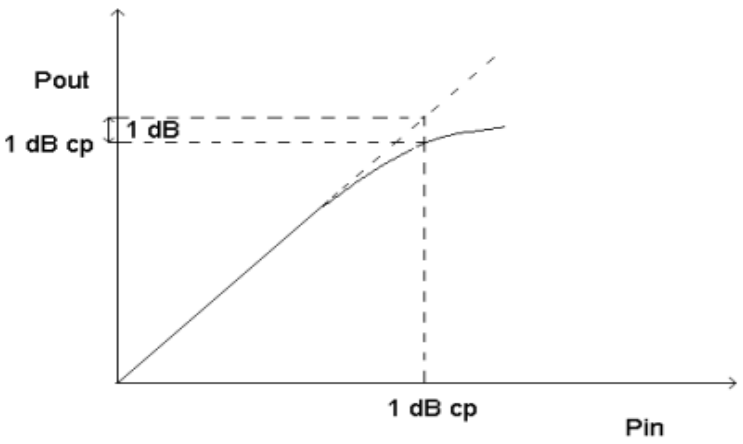

Figure 4.3: 1 dB Compression Point

The 1 dB compression point is defined as the output power at which the output is 1 dB lesser than the ideal output power. In figure 4.3, the input-output relationship is linear upto a certain point. But, if the input power is still allowed to be increased, then the output power does

not follow the ideal characteristics and it starts to deviate. There lies a particular input power 1 dB compression point, where the practical and ideal curve differs by an amount of 1 dB.

In the analog optical links, there are harmonic distortions to describe the non-linear behaviour of the circuits. If the input signal to the link possesses two frequencies f_1 and f_2, then due to the nonlinear behaviour of the medium, there are other frequencies creeps in. Due to the cubic term, the terms like $2f_1 - f_2$, $2f_2 - f_1$ et al will come into play. These are third order IM (Inter Modulation) products. As the difference between f_1 and f_2 is small, the components at $2f_1 - f_2$, $2f_2 - f_1$ appear in the vicinity of f_1 and f_2, which may be in the pass band of the device; thus, degrading the device performance.

Intercept Point (IP) is a figure of merit for the IM product suppression. A high intercept point refers to the high suppression of IM products. A third order intercept (IP3) is the point where the desired output power equals the third order IM product power. This is illustrated at figure 4.4.

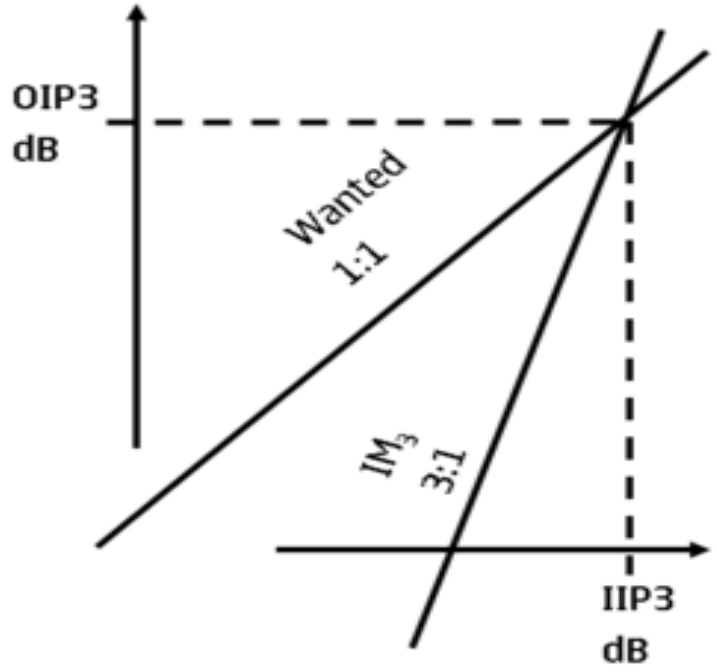

Figure 4.4: Graphical representation of third order IM Products

SFDR is the range of input power where the fundamental output is obtained in presence of noise but without non-linear interference. Third order IMD are used often to impose an upper bound of SFDR (Raut & Praveenkumar, 2001 [29]). Lower bound is taken as the receiver noise floor. The higher the SFDR, the better is the receiver. There lies a relationship between the SFDR and input third-order intercept point, for direct modulation as given by equation 4.25, where IP_3 be the input 1-dB compression point and NF_{total} be the noise figure in dB and SFDR is calculated in a bandwidth of 1-Hz.

$$SFDR = \frac{2}{3}(IP_3 + 174 - NF_{total}) \tag{4.25}$$

The SFDR for an externally modulated link (here, MZM link) is given by equation 4.26, where P_1, P_2 are modulated and unmodulated optical power respectively and Ω_1, Ω_2 are power loss in the link for modulated and unmodulated optical carrier respectively, R_{in}, R_{out} are input and output resistances respectively, η is photodiode responsivity, B is bandwidth, and I_{dc} be the dc photocurrent. The Noise Floor used here is given by equation 4.27.

$$SFDR(dB) = \frac{2}{3}[10\log_{10}(4P_1P_2\Omega_1\Omega_2\eta^2 R_{out}) - NoiseFloor(dBm)] \tag{4.26}$$

$$NoiseFloor(dBm) = 10\log_{10}(kTB + 2eI_{dc}R_{out}B + 10^{\frac{RIN}{10}} I_{dc}^2 R_{out}B) \tag{4.27}$$

There are certain advantages of the analog links. These are stated as follows.

- It is less complex.
- It reduces hardware and BW requirement.
- Here, the major hardware located at central location.
- There is reduced risk of radiated interference.
- There is no additional skill / training required to build, test and install units.
- It is easy to maintain.

There are disadvantages also. These are mentioned below.

- It is very sensitive to parameters affecting analog RF transmission (Phase, amplitude, Temperature, wavelength).
- The system is costly and requires less common components.
- It requires at least 20 dB SNR at receiver.
- The dynamic range is limited.

4.5. Digital Fiber-Optic Link:

In digital links, the optical modulation depth approaches 100%. For a digital fiber-optic link, the determining parameters are transmission distance, data rate or channel bandwidth and bit-error rate (BER). The components of the link, viz., transmitter, receiver and fiber are determined by the operating wavelength.

As per as the BER is concerned, the p-i-n photodiode is simple, stable with respect to the temperature variation and less expensive. If the optical power required is low, then the Avalanche Photo Diode (APD) with gains can also be used.

The spectral width of laser is lesser compared to that of a light emitting diode (LED). If the operating frequency is in the wavelength region between 800-900 nm, then the bandwidth-length product is 150 Megabit per second km for a silica fiber limited by its dispersion characteristics. In this wavelength region, LED can be used as the transmitter. But, if the operating wavelength is increased, then laser has been preferred. As an example, at a wavelength

of 1300 nm, the dispersion is minimum. By using LED, the bandwidth-length product obtained is 1500 Mbps only, while that using an InGaAsP laser, the product is 25 Gbps (Keiser, [24]). A single-mode fiber can operate upto a bandwidth-length product of 500 Gbps at an operating wavelength of 1550 nm. The coupling of optical power is more in laser compared to LED; but, the lasing threshold is controlled dynamically as a function of temperature.

The fiber is chosen between single-mode fiber (SMF) and multi-mode fiber (MMF) depending upon the source and application of the link. For LED to be the source, a MMF can be used. But, for a SMF fiber, an edge-limiting laser can be used. In practice, there are some other losses due to the connectors, splices, temperature drift, radiation, dust and moisture.

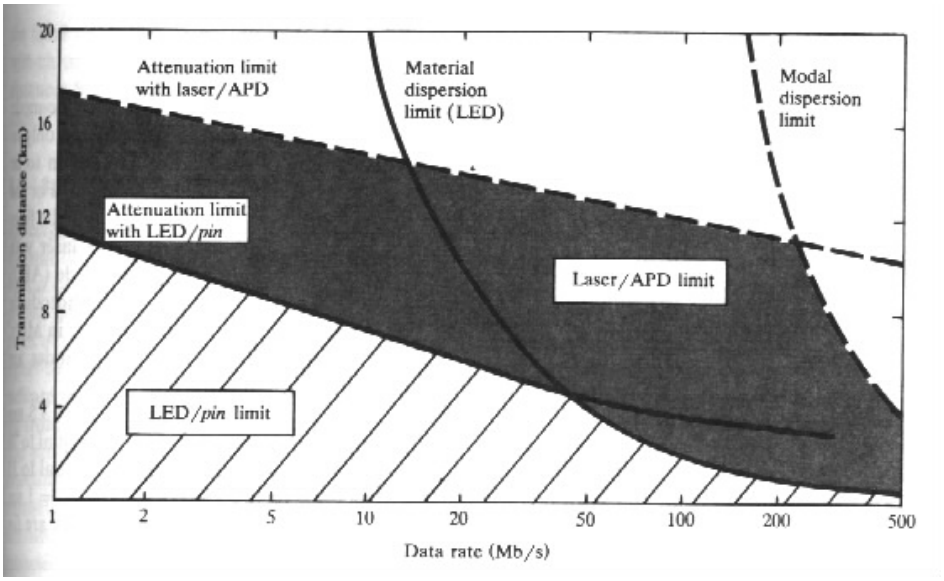

Figure 4.5: Transmission Window for different data rates

The transmission window for different data rates is shown in figure 4.5. There is attenuation and dispersion limitation on repeater less transmission distance as function of data rate for LED/p-i-n photodiode combination operating at 800-900 nm. The BER obtained is 10^{-9}. Upto 200 Mbps data rate, the output power of a LED is -13 dBm. Since the minimum optical power required at receiver for a given BER becomes higher for increasing data rates, the attenuation limit curve slopes downward to right. The material dispersion is 0.07 $nsnm^{-1}km^{-1}$ at an operating wavelength of 800 nm. The transmission distance is attenuation limited upto 40 Mbps, after which the distance is pre-dominantly material dispersion limited. Larger transmission distance can be obtained by the combination of laser and avalanche photodiode.

The transmission window for different digital modulation schemes and different spectral width is shown in figure 4.6. The dispersion due to group-velocity effect is 2.5 $psnm^{-1}km^{-1}$ and the attenuation at 1550 nm is $0.2\,dBkm^{-1}$. If a laser couples a 0 dBm optical power into the fiber with line width σ_λ of 3.5 nm, and a receiver APD with InGaAs possesses a sensitivity of $11.5\log B - 71$ dBm, while a InGaAs p-i-n photodiode has a sensitivity of $11.5\log B - 60.5$ dBm, B being the data rate in Mbps. Also, a system margin of 8 dB is taken into considerations.

For NRZ data format of spectral width of 3.5 nm, $D\sigma_\lambda L$ is 70% of the bit period while for RZ data format, $D\sigma_\lambda L$ is 35% of the bit period. In practice, the laser instabilities coupled with chromatic dispersion in fiber resulting in noise, reducing dispersion-limited distance.

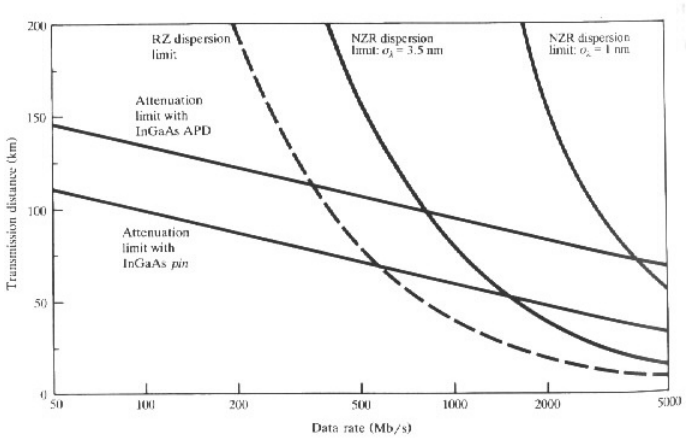

Figure 4.6: Transmission Window for different data rates of InGaAs photodiode

There are different noises in the link. These are modal noise, wavelength chirp, spectral broadening induced by optical reflections back into lasers and mode partition noise. In a SMF, the modal noise is absent. For a coupling between a coherent laser into a MMF, there is no problem below 100 Mbps but it poses a serious problem for data rate greater than 400 Mbps. There are mainly two sources of this noise. Mechanical disturbance along the link, like vibrations, connectors, splices, micro bends, source/detector coupling results in differential mode delay. The intermodal delays are due to frequency fluctuations also. A coherent source forms speckle patterns when the coherence time is greater than the intermodal dispersion time within the fiber i.e., if the frequency width be df, then the coherence time is df^{-1}, and for speckle formation, $df^{-1} < dT$ where dT be the intermodal dispersion time. The modal distortion due to interference between a single pair of modes appears as a sinusoidal ripple having frequency as given by equation 4.29, where $\frac{df_{source}}{dt}$ is the rate of change of optical frequency.

$$f = dT \frac{df_{source}}{dt} \tag{4.29}$$

From the figure 4.7, if number of speckles (M') is high, then the error rate curve approaches curve with no modal noise. As number of speckles decreases, the performance decreases. If M'=50, an additional 1 dB receiver power to maintain the BER of 10^{-6}. For M'=20 to maintain the same BER, the additional power required is 2 dB.

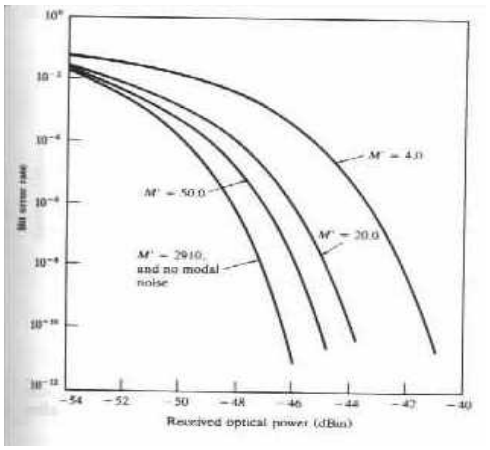

Figure 4.7: Variation of BER with received optical power

Mode partition noise is due to intensity fluctuations in longitudinal modes of laser i.e., sidebands are not suppressed. This is dominant in SMF. For BER=10^{-9}, the receiver error probability is 10^{-12}, as shown in point A in figure 4.8, the mode intensity ratio is nearly 50.

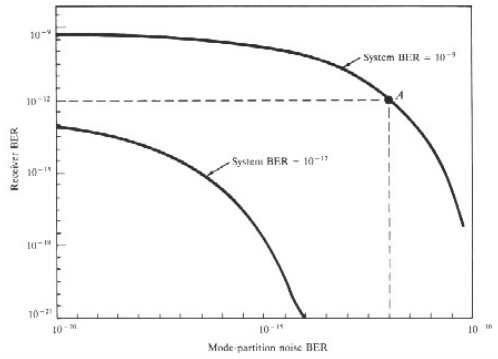

Figure 4.8: Variation of received BER with mode partition noise BER

In a single-longitudinal mode CW laser, the dynamic line broadening is due to the directly modulated injection current which results in dispersion for intensity-modulated pulses when laser emission wavelength is displaced from 1300 nm. To minimize this chirp, the bias level is increased so that modulation current does not drive below the threshold.

Reflection noise is due to the reflections at refractive index discontinuities like splice, coupler, filter, or air-glass interfaces in connectors. In high-speed systems, the reflected power causes optical feedback inducing laser instabilities. This leads to intensity noise, jitter (pulse distortion), or phase-noise in laser, changing the spectral width, operating wavelength and threshold current. There are two sources of this noise. Multiple reflection points set up an interferometric cavity feeding power back into the laser cavity, converting the phase-noise into intensity noise. Also, there are spurious signals at receiver with different delays causing the inter symbol interference (ISI).

There are salient advantages of digital fiber-optic links. These are stated as follows.

- Signal is frozen when digitized and less affected in transportation.
- It can use commercial fibre-optic systems at low cost.
- 10^{-5} BER is acceptable.
- It is ttolerant to group delay changes in fibre.

There are disadvantages also. These are mentioned below.

- Shifts complexity from a central building to remote antennas.
- Requires word frame sync. And data formatting.
- Requires very high BW.
- All high speed circuits produce harmonic and sub-harmonic interference.
- Back end systems cost more and complex compared to digital fibre-optic systems.

Chapter 5

DWDM Technology and Its Application in Upgradation of GMRT Link

5.1. Wavelength Division Multiplexing (WDM) System:

In a fiber-optic system, multiple optical carrier signals are multiplexed on a single fiber by using different wavelengths of laser to carry different signals by Wavelength Division Multiplexing (WDM). By this system, the capacity is multiplied, in addition to enabling bidirectional communications over one fiber-strand. This capacity improvement can be done by using optical-to-electrical-to-optical translation at the very edge of the transport network, thus permitting interoperation with existing equipment with optical interfaces. WDM systems are divided into different wavelength patterns, coarse WDM (CWDM) and dense WDM (DWDM). CWDM provides 16 channels in C-band of silica fiber (1550 nm), while DWDM uses the same window but with denser channel spacing. This is shown in figure 5.1.

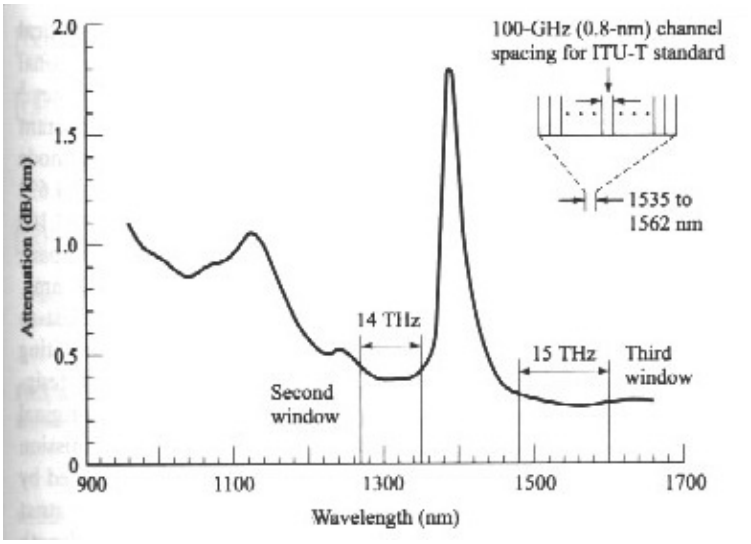

Fig. 5.1: Attenuation-Wavelength Curve showing Third Transmission Window (C-Band)

A WDM bidirectional link is shown in figure 5.2, where full duplex communication is achieved using a single fiber-optic cable. Here, the information flow in each of two directions is discriminated by two different wavelengths; one for each directions (Selvarajan et. al, [35]). For N-channel full-duplex communications, both the purposes can be achieved by combination of 2N distinct optical sources.

Fig. 5.2: A Bidirectional Link using WDM

A typical WDM link is shown in figure 5.3. Here, different wavelengths ($\lambda_1, \lambda_2, ...\lambda_N$) are multiplexed by using wavelength multiplexer and thereafter allowed to travel over a single fiber, where there is a demultiplexer at the other end, where they are separated ($\lambda_1, \lambda_2, ...\lambda_N$) by using the wavelength demultiplexer.

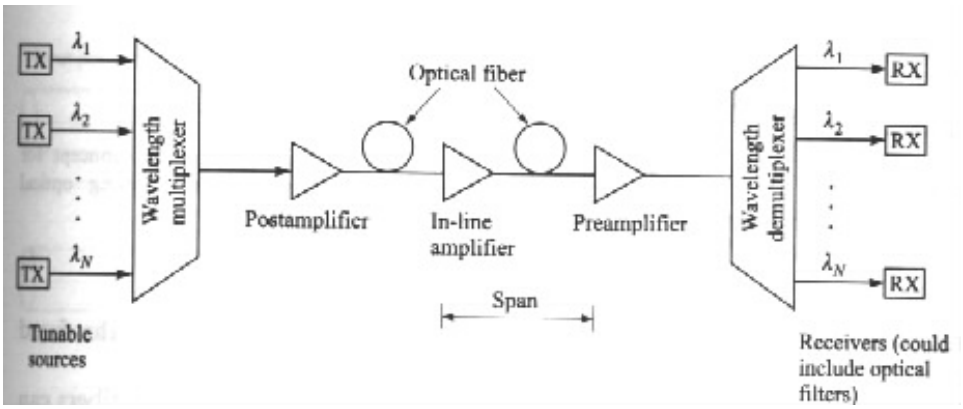

Fig. 5.3: A Typical WDM Link

5.2. CWDM System:

Here, the channel spacing as mentioned by ITU standard is approximately 20 nm. In recent ITU CWDM standard, the signals are not appropriately spaced for amplification by EDFAs. So, for a CWDM link of 2.5 Gbps signal, the optical span is 60 km; which is used in metropolitan applications. CWDM is used for cable TV networks also for providing different wavelengths for downstream and upstream. But, the downstream and upstream signals are well-separated like downstream is at 1310 nm and upstream at 1550 nm. The ITU-T G.694.2 standardized CWDM spectrum is shown in figure 5.4.

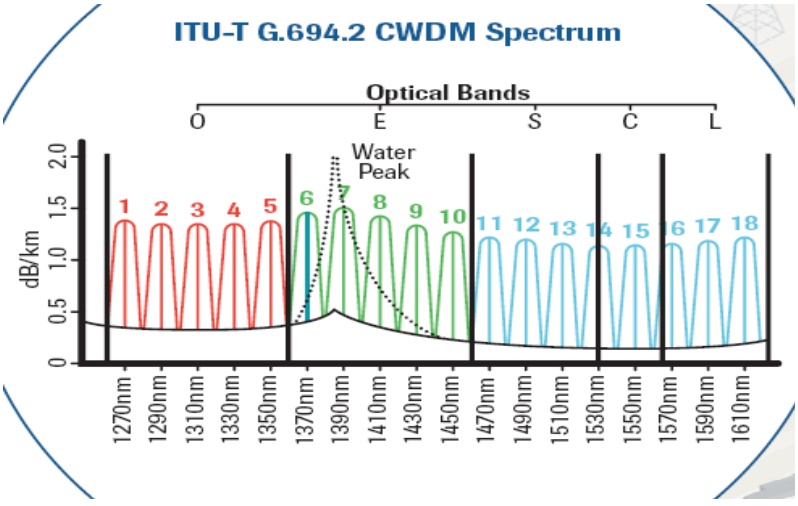

Fig. 5.4: ITU-T G.694.2 Standard CWDM Spectrum

5.3. DWDM System:

Dense Wavelength Division Multiplexing (DWDM) refers to signal multiplexing within 1550 nm band for the capability of EDFAs, which are effective for wavelengths between C-band (1525-1565 nm) or L-band (1570-1610 nm). Many wavelengths can be generated around 1550 nm. ITU-T Recommendation G.692 defines 43 wavelength channels from 1530 to 1565 nm, at a spacing of 100 GHz; carrying signal of 10 Gbps. The number of channels depends on fiber type [23]. A single strand of Single-Mode fiber can transmit over 80 km without amplifications. EDFAs can amplify any optical signal in their operating range, regardless of modulated bit rate. As pump energy of EDFA is high, many optical signals can be multiplexed within the amplification band. Thus, EDFA can allow a single-channel optical link to be upgraded in a bit-rate by replacement of equipments at link end, while retaining existing EDFA or series of EDFAs through a long route. Moreover, single-wavelength links using EDFAs can be upgraded to WDM links at reasonable cost.

DWDM utilizes a large aggregate bandwidth in a single fiber by taking advantage of advanced optical technology which is able to launch and multiplex many wavelengths in one fiber, switch wavelengths optically, and at receiving end demultiplex and read each wavelength separately [37]. Each wavelength in DWDM constitutes a separate channel capable of carrying traffic at a bit rate that may not be same in all channels. Since a channel consists of narrowband around the centre wavelength instead of a singular wavelength, each band is spaced from next by several GHz to provide safety zone and to avoid crosstalk and channel-wavelength overlapping. This is done for two reasons. Firstly, laser sources and tunable filters may drift with temperature and time, optical amplifiers do not exhibit true flat gain over the wavelength range, spontaneous noise from EDFAs is cumulative, and there are dispersion effects. The centre frequency for DWDM is governed by equation 5.1, as it is obvious from figure 5.5, where F be the centre frequency and m is an integer.

$$F = 193.1 \pm m \times 0.1 \tag{5.1}$$

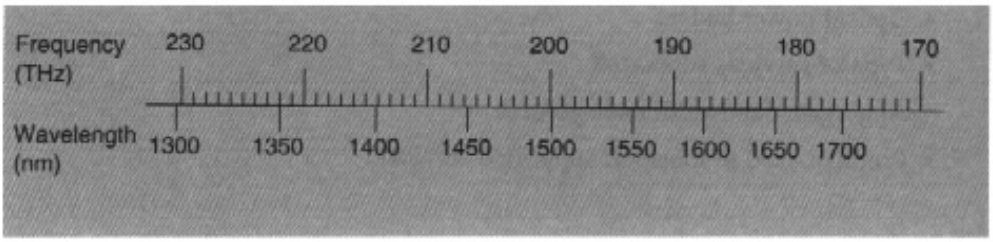

Fig. 5.5: The Centre Frequency for DWDM Applications

Here, frequency is used instead of wavelengths since certain materials emit specific well-known optical frequencies used as reference points. Additionally, the frequency remains constant; while the wavelength may vary due to change in refractive index of material. In DWDM, the number of channels, center frequency, frequency width, and channel separation are very important.

Centre frequency and the channel width determine number of non-overlapping channels in the spectrum. Channel width, wavelength, bit rate, fiber type, and fiber length determine the dispersion. The channel separation should allow for a frequency deviation of 2

GHz due to the frequency drift in laser, filter and amplifier to avoid intersymbol interference (ISI). The channel bit rate and the modulation determine channel width and the separation limits. Dispersion, noise due to amplifiers and noise due to other sources affect the signal-to-noise ratio (SNR) and hence, signal integrity. As the dispersion increases, the crosstalk also increases.

The maximum optical power launched per channel in fiber is the optical signal at the receiver to detect power without the error so that BER<10^{-11}. But, as the optical power increases, the non-linear effects come into play. Hence, there should be a compromise between the two.

Optical amplifiers are used in the system to restore the optical signal intensity. But, this includes cumulative pulse widening and cost. EDFAs performance becomes best at an operating wavelength of 1550 nm. The amplifier bandwidth, amplifier spontaneous emission (ASE), linear effects like attenuation, chromatic dispersion and polarization mode dispersion (PMD) limit the total system. Additionally, there are non-linear effects related to refractive index and scattering degrade the system performance. The non-linear effect depends upon the optical power density which is the power per effective area. This effective area is the cross-section of light path in the fiber. For a dispersion-shifted fiber (DSF), it has a value $50\mu m^2$ and for a single-mode fiber (SMF), it has a value of $75\mu m^2$. As the optical power density increases, the fiber length increases as well as the non-linear effects increase. For a minimum BER (<10^{-9}), there should be low optical power requirement to have low bit rate. Thus, there should be a compromise in the optical power. The optical amplifiers bandwidth and receivers ability to identify two close wavelengths sets the channel spacing. A typical DWDM specification is shown in figure 5.6.

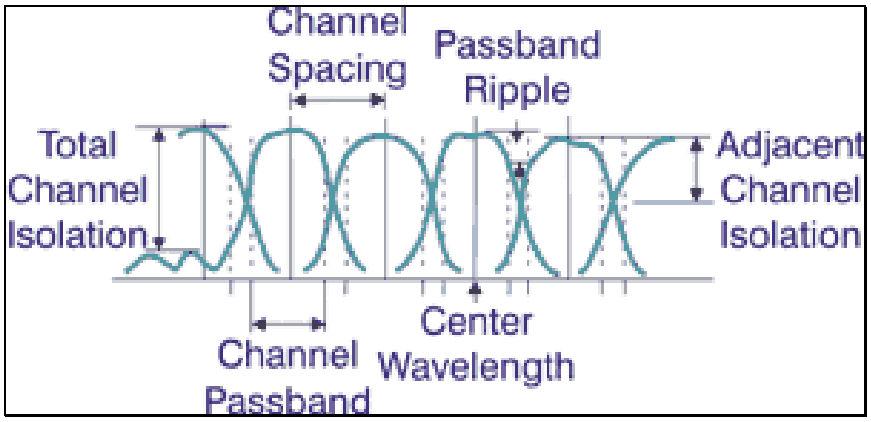

Fig. 5.6: Typical Output Characteristics for DWDM Channels

A point-to-point technology using DWDM technology is shown in figure 5.7. It is used for long-haul communication at a speed of 10-40 Gbps. This also provides high bandwidth of Terabits per seconds, high signal integrity, great reliability, and fast path restoration capability. The Optical Add-Drop Multiplexer (OADM) enables the system to add or drop channels. A low-cost and low-loss OADM adds or drops groups of wavelengths on a selective basis.

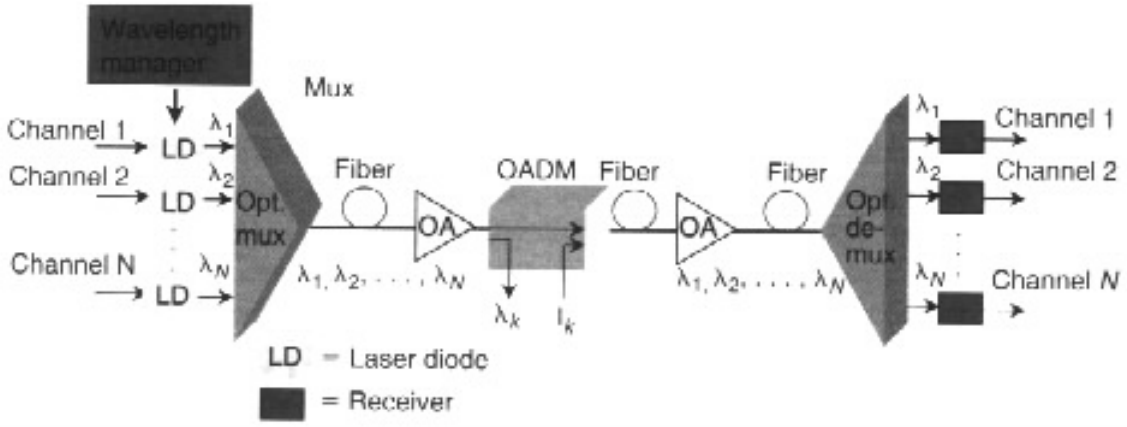

Fig. 5.7: A Point-To-Point (PTP) DWDM Link Using OADM

5.4. Applications of DWDM System for Upgradation of GMRT:

The GMRT existing link is planned to upgrade using the DWDM technology. The Upgradation plan of the link is shown in figure 5.8. Here, two polarizations have been received by two different wavelengths from the front-end system, marked as LHCP and RHCP. Both these outputs are then amplified by an MSA0520 amplifier of 8 dB. Both the amplified outputs are then splitted through a 3-dB power splitter and one of the splitted outputs is transferred to the IF system while the other one is amplified by 22 dB by a GALI amplifier. The amplified signal is passed to an optical transmitter containing a single mode laser (DFB laser) which is ideal for DWDM applications. The modulated optical outputs are then passed to a DWDM Multiplexer and sent through the optical fiber. The multiplexed optical output received at the receiver end is demultiplexed by using a DWDM Demultiplexer and then passed to separate optical receiver units. The optical signals are reconverted back to electrical signals by the optical receivers. Here, the advantage lies in the fact that the system employs the direct transmission of the received RF over fiber to have the larger SFDR. Thus, no down conversion into the intermediate frequencies will further occur. This new link has been established by the Fiber-Optic group of GMRT in three antennas till now; C5, C11 and W4.

The new link can be used to provide support for the existing GMRT link. This has been shown in figure 5.9. By using a WDM coupler, as mentioned earlier, the Telemetry signal is sent from the receiver room to the antenna base (ABR). The Local Oscillator signal is also sent for the synchronization to suffer minimum loss. These are sent via 1550 nm OTX at receiver end and received by ORX at ABR. But, currently 1310 nm is used in exiting GMRT link. By using the 1310 nm wavelength, Telemetry, IF and LO are sent via 1310 nm OTX as the return link and received by ORX at the receiver end.

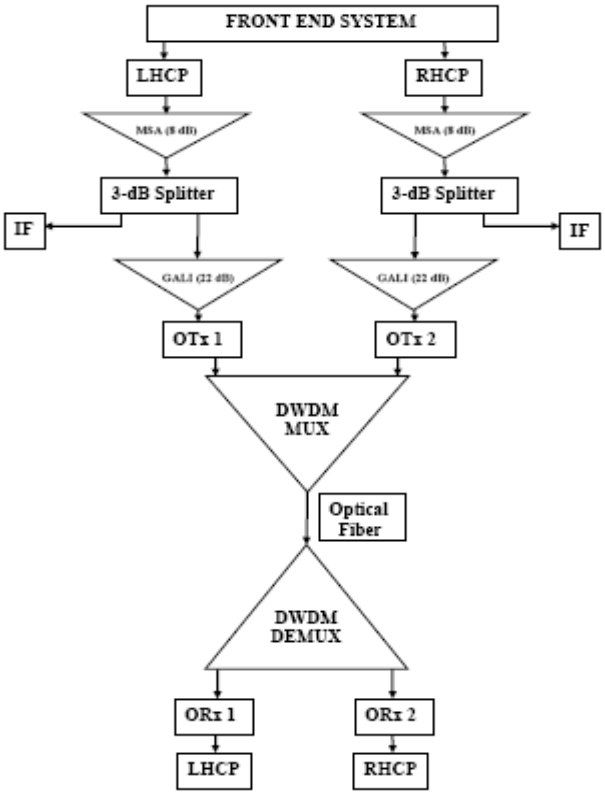

Fig. 5.8: Broadband Optical Fiber Link using DWDM Technology

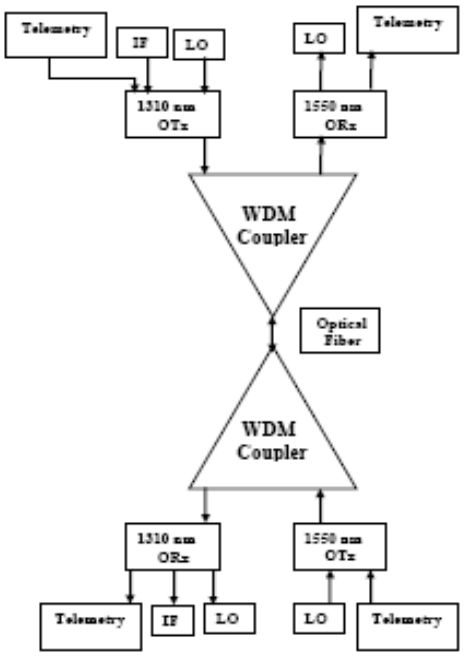

Fig. 5.9: Broadband Optical Fiber Link to Support the Existing Link

5.5. Components of the DWDM System for Upgradation of GMRT:

The block diagram of the transmitter used in the DWDM system is shown in the figure 5.10. It consists of four different blocks. These are Laser Diode Module, Automatic Power Control (APC), Thermoelectric Cooler (TEC) and the Slow Start.

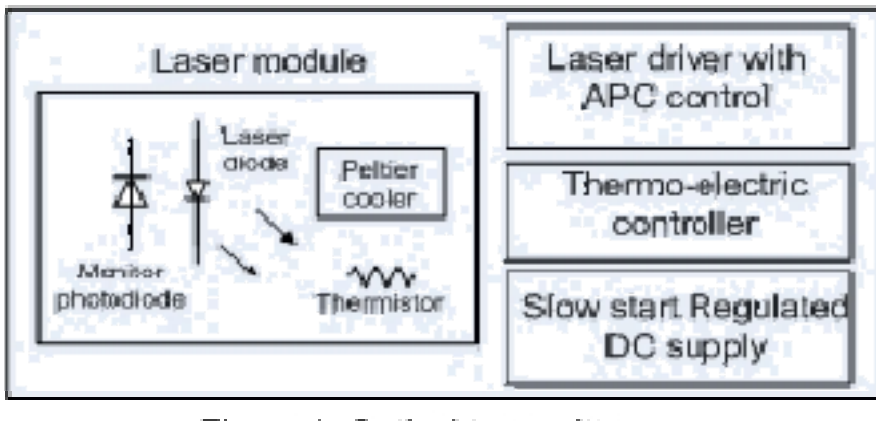

Fig. 5.10: Optical Transmitter

5.5.1. Laser Diode (LD) Module:

The job of transmitting a signal through the fiber cable can be done easily with help of Laser Diode. Laser diode can be best characterized by its upper limit and lower limit. When a supply is given to laser diode its get energized to its lower limit. Now when a modulating signals, which in analog form is applied to laser it, emits the light proportional to modulating signal.

5.5.2. Thermoelectric Controller (TEC):

As the fiber optic transmitter, is based on technique of DWDM (Dance Wavelength Division Multiplexing). In this technique different wavelength signal are multiplexed and send through a single fiber. It shows that wavelength of a laser diode depends on its temperature, so by varying temperature of laser diode we can adjust the wavelength of laser diode. Normally it varies about 0.1-nm/ºC changes in temperature. Since our surrounding temperature doesn't remain constant; as generally it varies up and down in whole day, which is undesirable for the operation of laser diode and finally will affect its operating wavelength; so as to maintain temperature of laser diode at its fixed value thermoelectric controller is used for this purpose. If temperature reaches above its rated value, then it absorbs current from laser diode. If temperature reaches below its rated value then it source current to laser diode and maintain temperature at its desired value.

5.5.3. Automatic Power Control (APC):

Bias current is applied to laser diode for its operation witch bias laser at its mid bias point of its power versus current characteristic, and then modulating signal is applied to laser diode along with this bias current, so we can modulate an analog signal. If bias current changes from middle point, then it varies the output power of laser diode, and output modulated signal

will not be proper. To maintain output power constant, maintain bias point at middle of its characteristic, for this purpose APC unit is used. It consist of a photo detector which senses the output of laser diode and feed back this output to circuit which detect only the bias current and maintain the output power constant.

5.5.4. Slow Start:

Laser diode used in this transmitter is very sensitive for any voltage spike in the supply voltage, it get damage due to any voltage spike in supply voltage. To prevent laser diode from this damage soft start circuit is provide for this purpose, soft start circuit applies voltage to laser diode in controlled manner.

The transmitter circuitry is shown in figure 5.11; where it is integrated with other components to be driven by a laser driver. Here, it is used as MAX3273A. The total DWDM system using MUX-DEMUX is shown in figure 5.12.

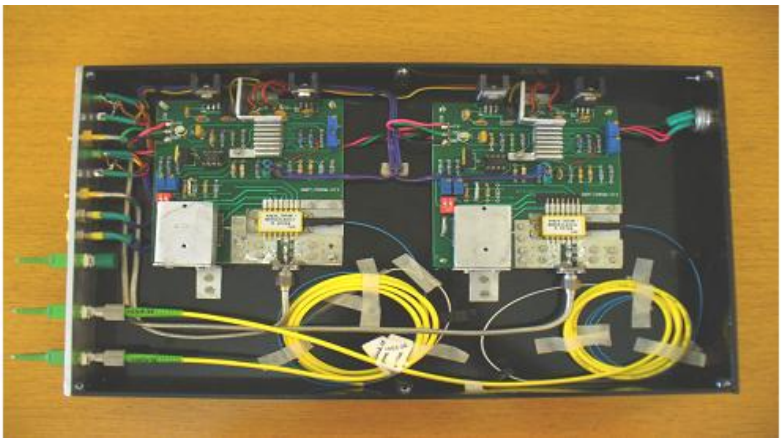

Fig. 5.11: DWDM Transmitter using the Laser Driver Circuitry

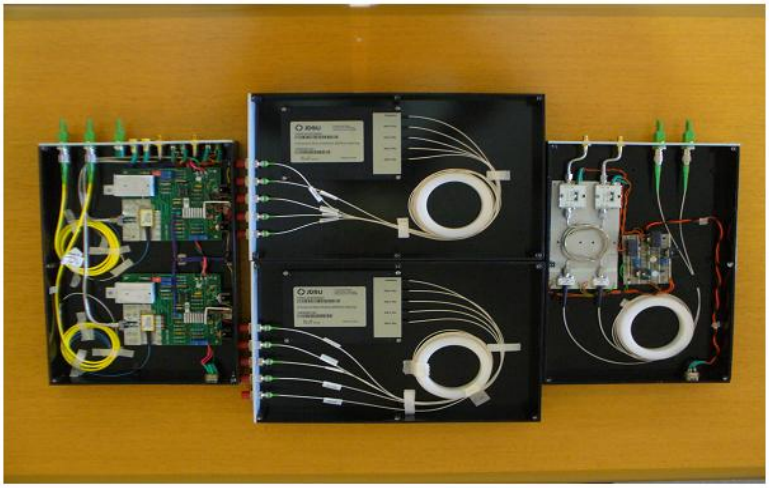

Fig. 5.12: Total DWDM System using Transmitter, MUX, DEMUX and Receiver

Chapter 6

System Performances of DFB-Uncooled Laser and DWDM Laser

6.1. DFB-Uncooled Laser:

The MQW-DFB laser is used as optical transmitter on which the RF signals are imposed and the modulated signals are multiplexed using DWDM MUX. The link specification details using DWDM laser and 10 Gbps TIA receivers using Discovery Semiconductor has been shown in table 6.1. Also, the DFB-Uncooled laser together with the Ortel receiver has been characterized by using its noise performances. The different parameters of the link specifications have been mentioned in table 6.2. This laser is used as the transmitter of telemetry signal from CEB to Antenna Base as the transmitter in the WDM bidirectional link.

Table 6.1

(MQW-DFB Laser (NX8563LA) and Discovery Semiconductor TIA Receiver)

Parameters	Value
Laser Relative Intensity Noise (RIN)	-140 $dBmHz^{-1}$
$I_{Bias} - I_{Th}$	43 mA
Laser Slope Efficiency (η_l)	0.1701 WA^{-1}
Maximum Optical Power (P_{max})	1 mW
Photodiode Responsivity (R)	0.8 AW^{-1}
Input and Output Impedance	50 Ω and 500 Ω
Dark Current (I_d)	10 nA

Table 6.2

(DFB- Uncooled Laser (D571) and Ortel Receiver)

Parameters	Value
Laser Relative Intensity Noise (RIN)	-155 $dBmHz^{-1}$
$I_{Bias} - I_{Th}$	9.39 mA
Laser Slope Efficiency (η_l)	0.095 WA^{-1}
Maximum Optical Power (P_{max})	1 mW
Photodiode Responsivity (R)	0.8 AW^{-1}
1-dB Compression Point (P_{1dB})	+21 dBm
Third-order Intercept Point (IIP_3)	+30.1 dBm
Input and Output Impedance	50 Ω
Dark Current (I_d)	1 nA

From the input details, the RF parameters (Conversion Loss, Total Noise Power, Equivalent Input Noise, Noise Figure and SNR) of the link using MQW-DFB laser and Discovery Semiconductor Receiver have been computed. The results have been shown in figure 6.1.

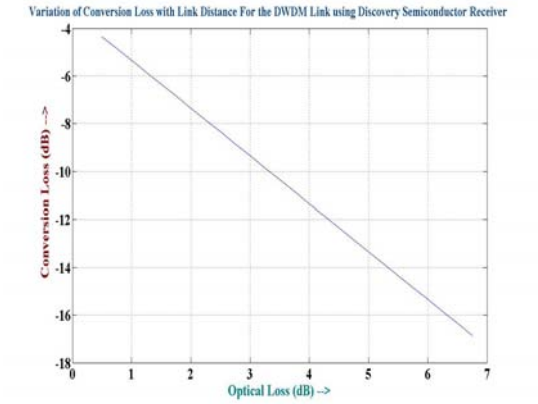

Figure 6.1(a): Variation of Conversion Loss

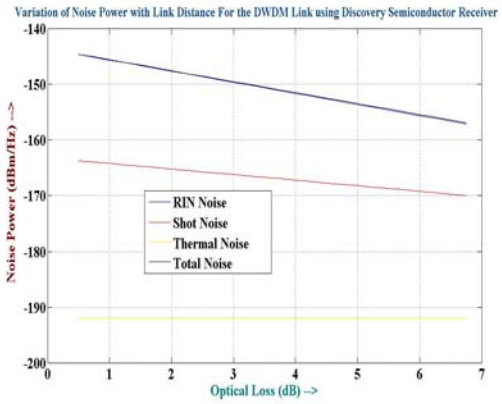

Figure 6.1(b): Variation of Noise Power

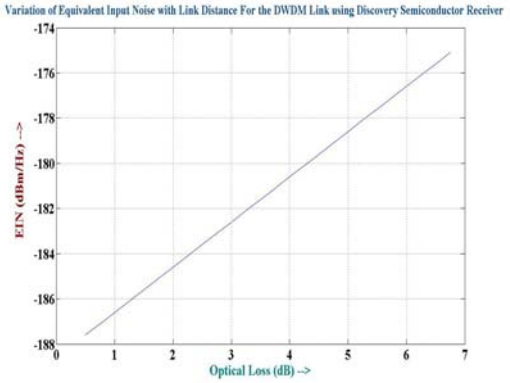

Figure 6.1(c): Variation of EIN

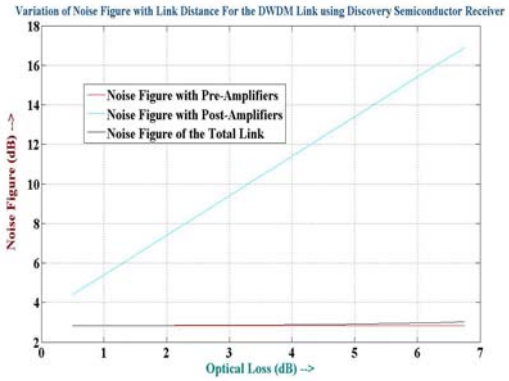

Figure 6.1(d): Variation of Noise Figure

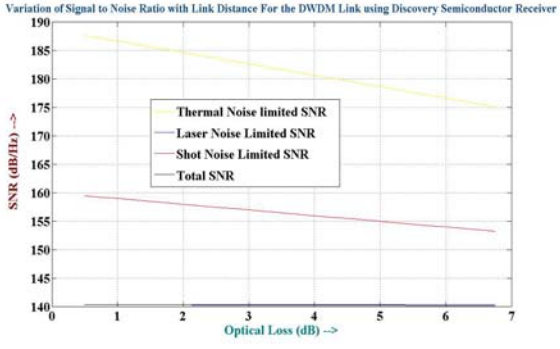

Figure 6.1(e): Variation of Signal-To-Noise Ratio (SNR)

These calculated parameters for MQW-DFB laser with Discovery Semiconductor receiver have been compared with those of existing GMRT link. The comparisons of different calculated parameters have been shown in figure 6.2.

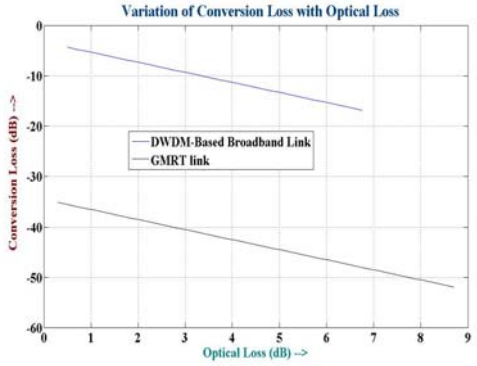

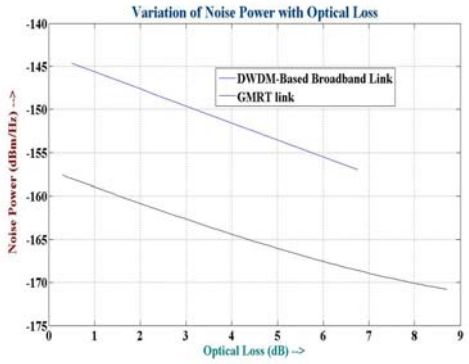

Figure 6.2(a): Comparison of Conversion Loss **Figure 6.2(b): Comparison of Noise Power**

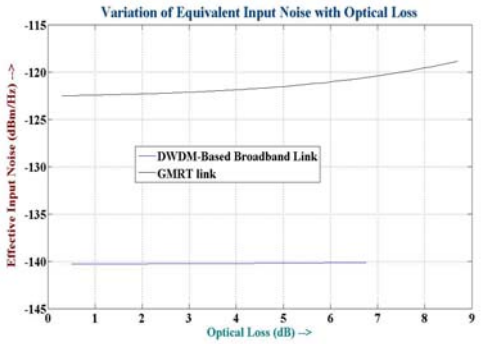

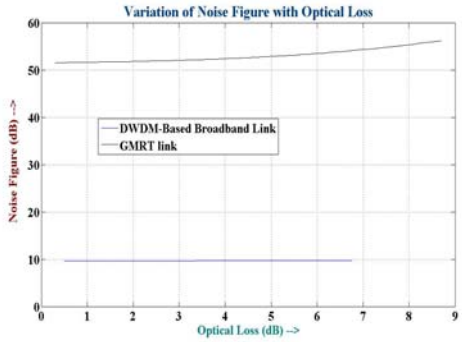

Figure 6.2(c): Comparison of EIN **Figure 6.2(d): Comparison of Noise Figure**

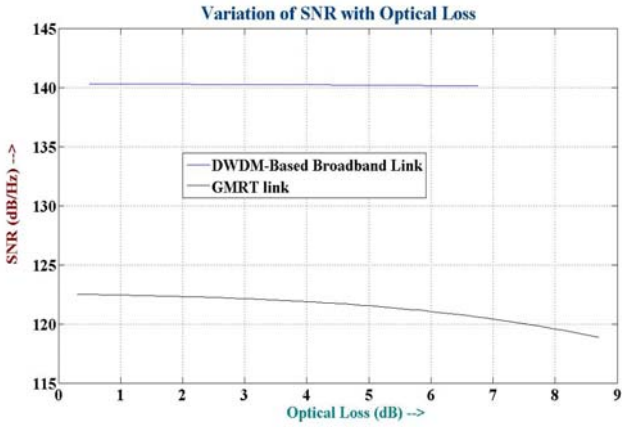

Figure 6.2(e): Variation of Signal-To-Noise Ratio (SNR)

From the input details, the RF parameters (Conversion Loss, Total Noise Power, Equivalent Input Noise, Noise Figure, SNR and SFDR) of the link using DFB-Uncooled laser and Ortel Receiver have been computed. The results have been shown in figure 6.3.

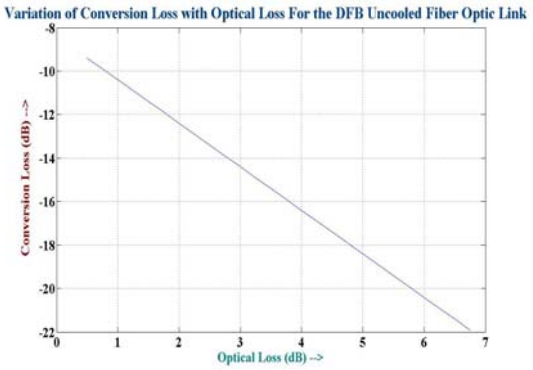

Figure 6.3(a): **Variation of Conversion Loss**

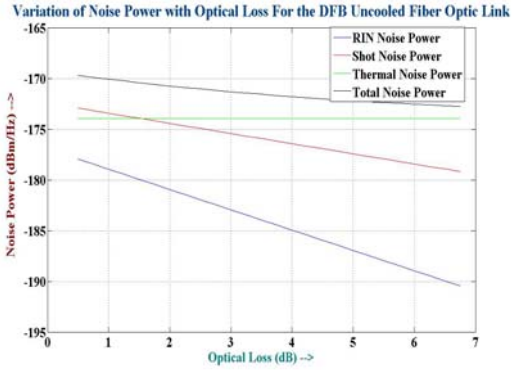

Figure 6.3(b): **Variation of Noise Power**

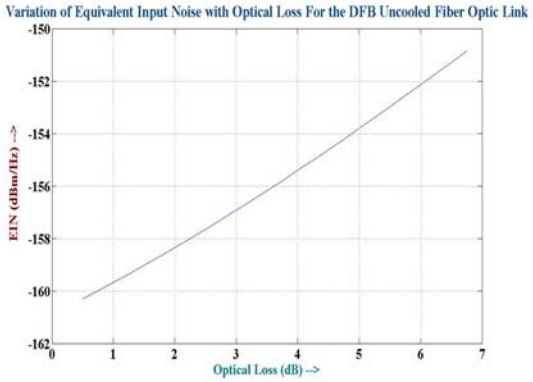

Figure 6.3(c): **Variation of EIN**

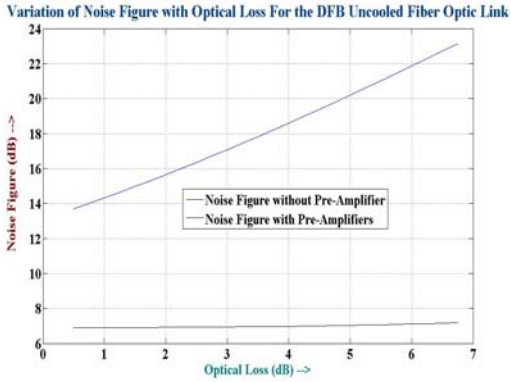

Figure 6.3(d): **Variation of Noise Figure**

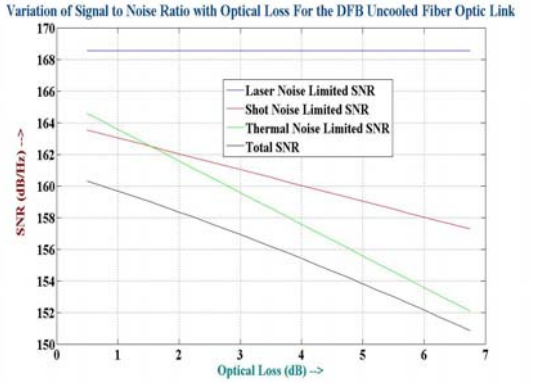

Figure 6.3(e): **Variation of SNR**

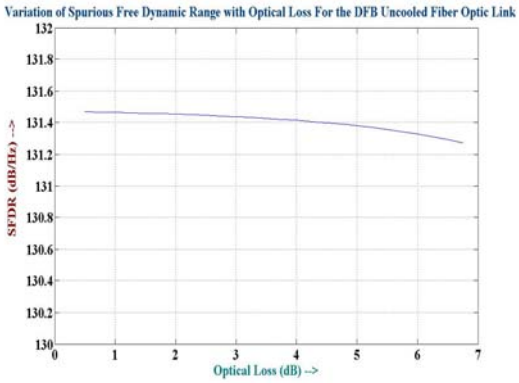

Figure 6.3(f): **Variation of SFDR**

These calculated parameters for DFB-Uncooled laser with Ortel receiver have been compared with those of existing GMRT link. The comparisons of different calculated parameters have been shown in figure 6.4.

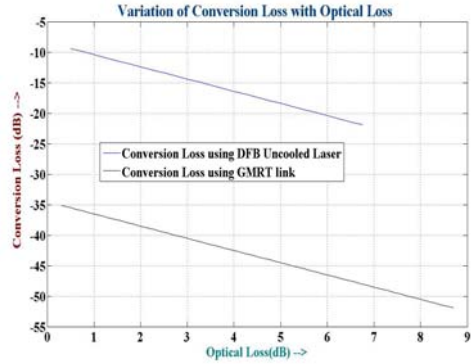

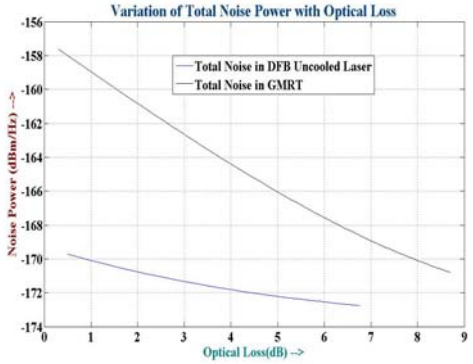

Figure 6.4(a): Comparison of Conversion Loss **Figure 6.4(b): Comparison of Noise Power**

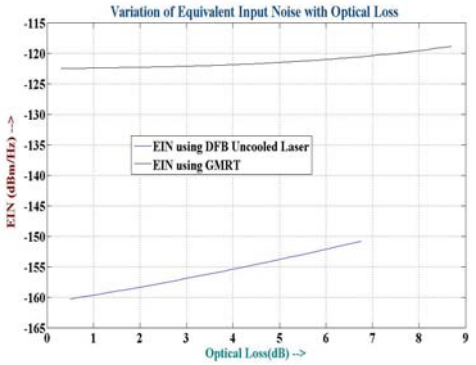

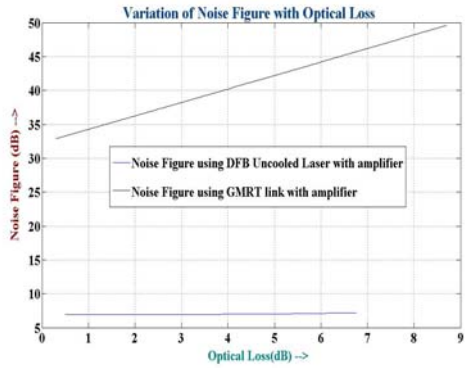

Figure 6.4(c): Comparison of EIN **Figure 6.4(d): Comparison of Noise Figure**

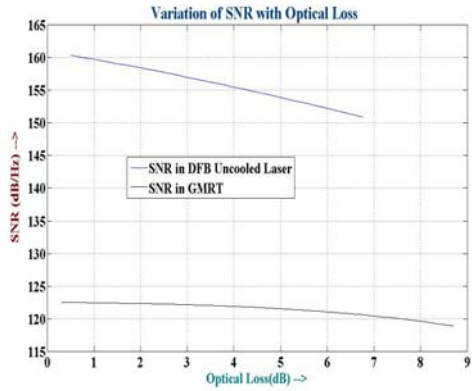

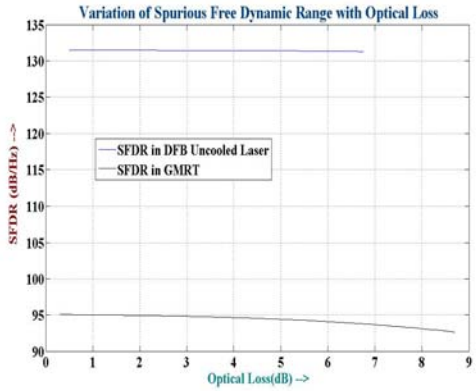

Figure 6.4(e): Variation of SNR **Figure 6.4(f): Variation of SFDR**

Chapter 7

Characterization of DFB-Uncooled Laser

7.1. Stability of DFB-Uncooled Laser:

The stability of a DFB-Uncooled laser has been done and tested with the help of a LabView Program and thereafter with successful testing, it has been kept into an environmental test chamber in which the temperature has been varied to test the bias and power stability with respect to the temperature. Since there is an automatic power control in the transmitter, so, the power should remain constant with temperature variation while the bias will increase or decrease with temperature increase or decrease respectively.

7.1.1. By using LabView:

The block diagram of the experimental set up for testing the bias stability in LabView is shown in figure 7.1 and the LabView front panel has been shown in figure 7.2. Data have been recorded online by using LabView as DAQ Assistant in the figure indicates the National Instrument I/O Card, which has been configured. The outputs (bias voltages and temperature) have been taken separately and then stored in a file, named, '18may_uncooled.LVM', where data are available for nearly 1000 minutes, with an interval of 1 minute. The variation of bias and temperature can be seen in the front panel, where three indicators have been displayed; two to notice the bias variations and one to notice the temperature variation with time. The recorded data (bias and temperature) have been plotted using MATLAB scripts, as shown in figure 7.3.

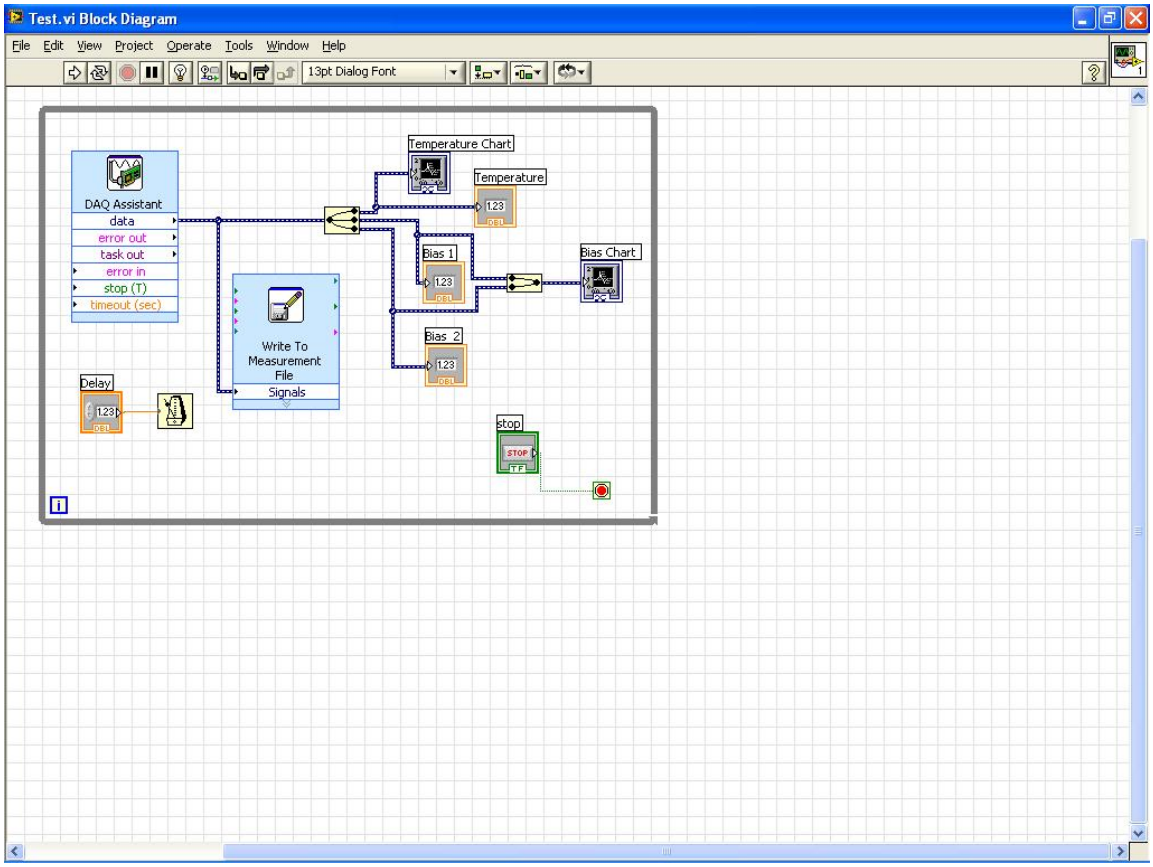

Figure 7.1: The Experimental Setup for Bias Stability in LabView

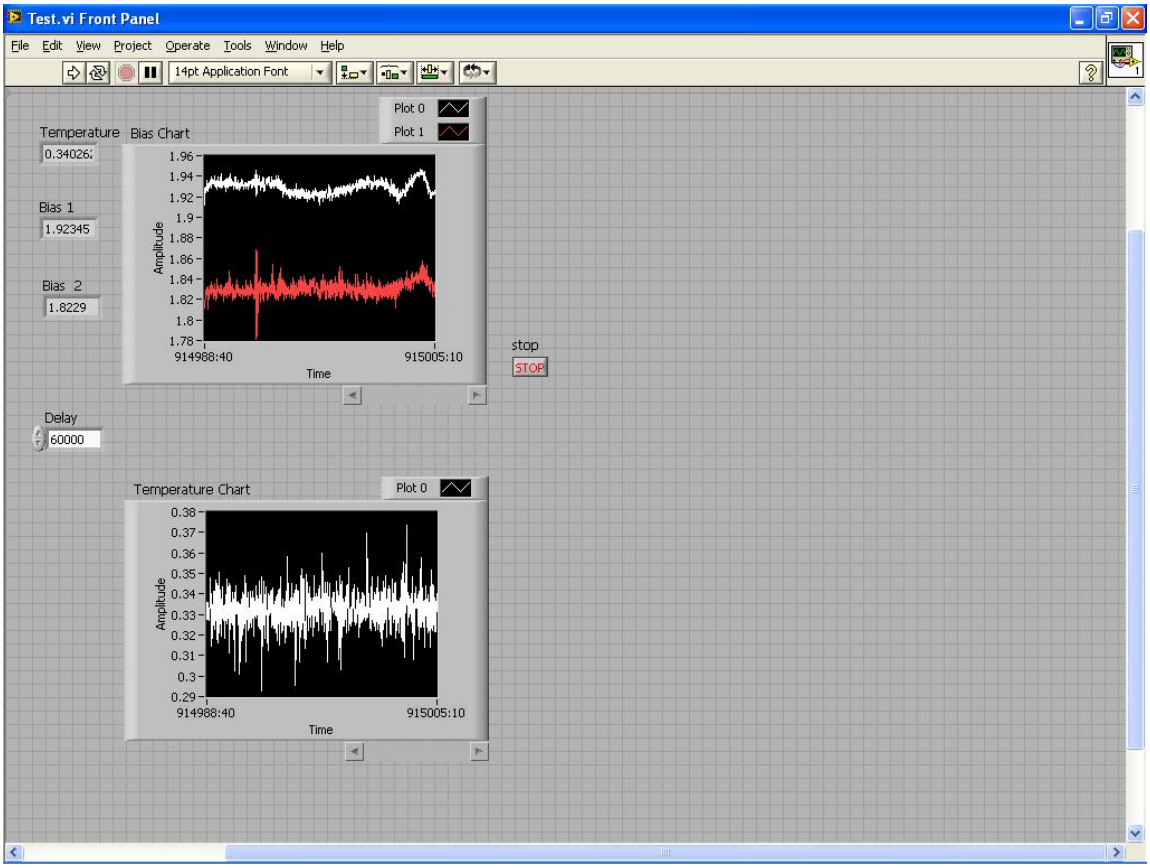

Figure 7.2: Front Panel showing the result in LabView

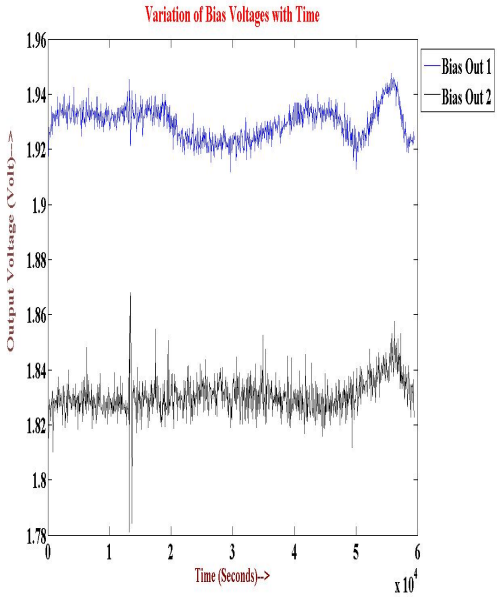

Figure 7.3(a): Bias variations with time

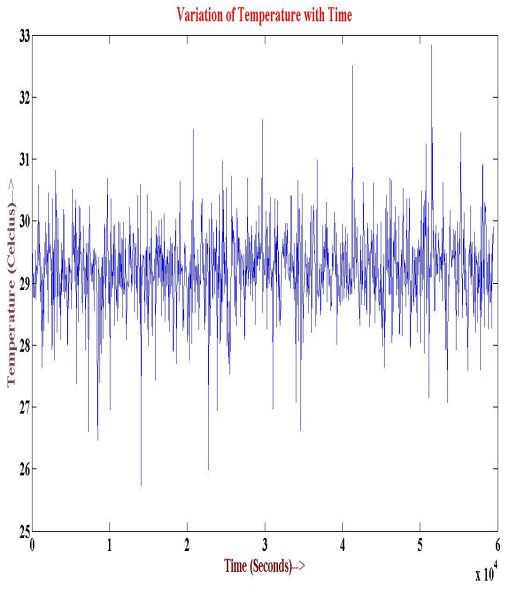

Figure 7.3(b): Temperature variations with time

7.1.2. By Environmental Test Chamber:

The block diagram of the experimental arrangement is shown in figure 7.4(a). Here, there are two DFB-Uncooled lasers (T1 and T2) have been put into the environmental test chamber. The temperature of the chamber has been varied, which is noticed by the thermometer kept inside. There are two multimeters, measuring output voltages from the transmitter, which can make aware of the operating bias current since the voltage has been measured across a known resistance. Also, there are two optical power meters which measure the optical powers coming out from the transmitter and going towards the Ortel receivers. The total arrangement is shown in figure 7.4(b). At first, the temperature has been increased while later on, the temperature has been decreased continuously. The readings of bias, optical power and temperature have been taken. The readings for increasing and decreasing temperature have been shown in table 7.1 and table 7.2 respectively. The results of bias and optical power stability are shown in figure 7.5 and figure 7.6 for first and second transmitter respectively.

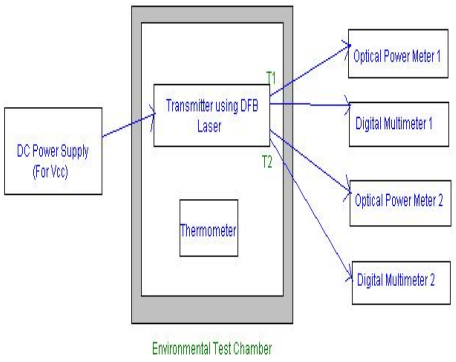

Figure 7.4(a): Block diagram of the scheme **Figure 7.4(b): Total experimental arrangement**

Table 7.1

(Temperature Increasing)

Temperature	First Transmitter			Second Transmitter		
(degree Celsius)	Bias Voltage (Volt)	Bias Current (mA)	Optical Power (dBm)	Bias Voltage (Volt)	Bias Current (mA)	Optical Power (dBm)
9	1.865	56.5152	4.7	1.781	53.9697	4.7
10	1.868	56.6061	4.8	1.780	53.9394	4.6
11	1.873	56.7576	4.8	1.785	54.0909	4.6
12	1.856	56.2424	4.8	1.789	54.2121	4.6
13	1.894	56.9091	4.8	1.808	54.7879	4.6
14	1.878	57.3939	4.8	1.823	55.2424	4.6
15	1.895	57.4242	4.8	1.842	55.8182	4.6
16	1.927	58.3939	4.9	1.851	56.0909	4.6
17	1.927	58.3939	4.9	1.870	56.6667	4.6
18	1.953	59.1818	4.9	1.891	57.3030	4.6
19	1.966	59.5758	4.9	1.903	57.6667	4.6
20	1.989	60.2727	4.9	1.915	58.0606	4.6
21	1.991	60.3333	4.9	1.930	58.4848	4.6
22	2.001	60.6364	4.9	1.940	58.7879	4.6
23	2.016	61.0909	4.9	1.950	59.0909	4.6
24	2.025	61.3636	4.9	1.954	59.2121	4.6
25	2.017	61.1212	4.9	1.960	59.3939	4.6
26	2.023	61.3030	4.9	1.982	60.0606	4.6
27	2.061	62.4545	4.9	1.991	60.3333	4.6
28	2.050	62.1212	4.9	2.018	61.1515	4.6
29	2.094	63.4545	4.9	2.033	61.6061	4.6
30	2.088	63.2727	4.9	2.056	62.3030	4.5
31	2.115	64.0909	4.9	2.090	63.3333	4.5

Table 7.2

(Temperature Decreasing)

Temperature	First Transmitter			Second Transmitter		
(degree Celsius)	Bias Voltage (Volt)	Bias Current (mA)	Optical Power (dBm)	Bias Voltage (Volt)	Bias Current (mA)	Optical Power (dBm)
32	2.109	63.909	4.6	2.081	63.061	4.1
31	2.109	63.909	4.6	2.087	63.242	4.2
30	2.110	63.940	4.7	2.087	63.242	4.2
29	2.111	63.970	4.7	2.088	63.273	4.2
28	2.112	64.000	4.7	2.090	63.333	4.3
27	2.113	64.030	4.8	2.091	63.364	4.4
26	2.113	64.030	4.8	2.092	63.394	4.5.
25	2.114	64.061	4.8	2.077	62.939	4.5
24	2.116	64.121	4.9	2.092	63.394	4.5
23	2.117	64.152	4.9	2.064	62.545	4.6
22	2.116	64.121	4.9	2.049	62.091	4.6
21	2.095	63.485	4.9	2.033	61.606	4.6
20	2.101	63.667	4.9	2.023	61.303	4.6
19	2.095	63.485	4.9	1.995	60.455	4.6
18	2.064	62.545	4.9	1.980	60.000	4.6
17	2.049	62.091	4.9	1.958	59.333	4.6
16	2.028	61.455	4.9	1.949	59.061	4.6
15	1.998	60.545	4.9	1.936	58.667	4.6
14	1.993	60.394	4.9	1.911	57.901	4.6
13	1.965	59.545	4.9	1.901	57.607	4.6
12	1.964	59.515	4.9	1.887	57.182	4.6
11	1.912	57.939	4.9	1.862	56.424	4.6
10	1.926	58.364	4.9	1.847	55.970	4.6
9	1.877	56.879	4.9	1.835	55.607	4.6
8	1.901	57.607	4.9	1.813	54.939	4.6
7	1.855	56.212	4.9	1.790	54.242	4.6
6	1.860	56.364	4.9	1.780	53.939	4.7

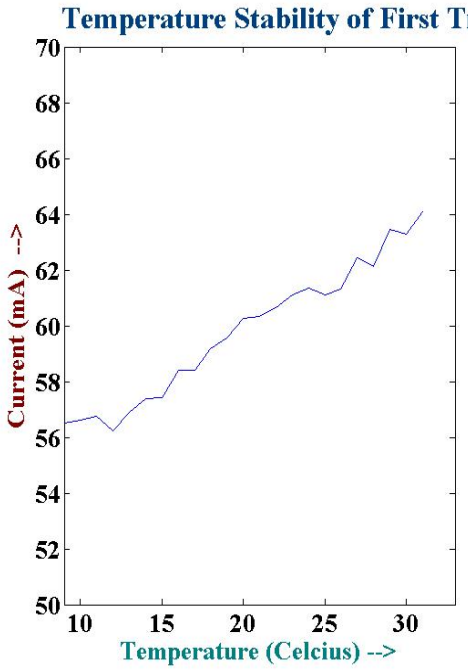

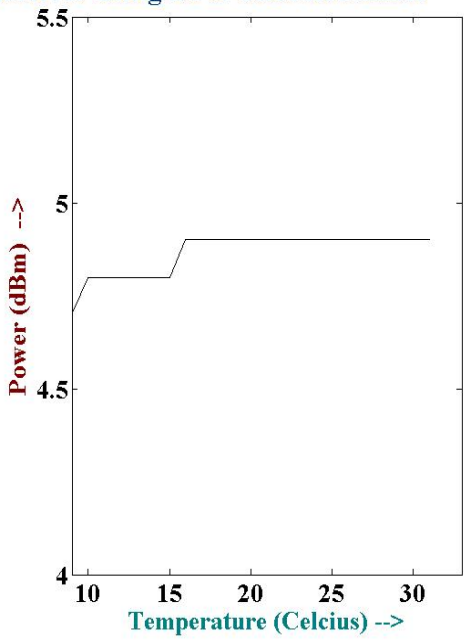

Figure 7.5(a): Bias Variation

Figure 7.5(b): Optical Power Variation

(Temperature Increasing for First Transmitter)

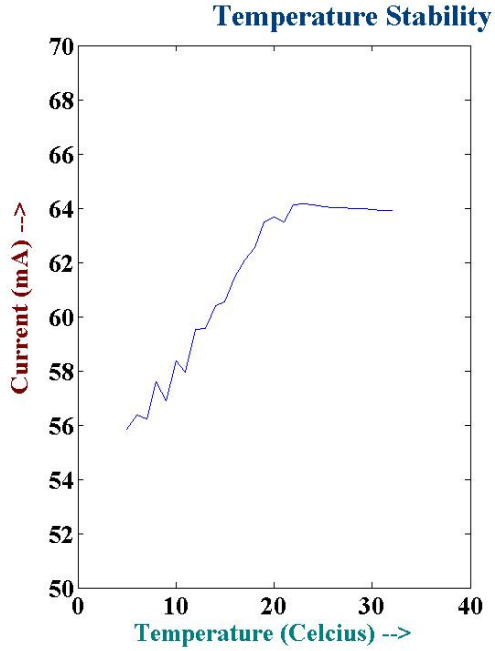

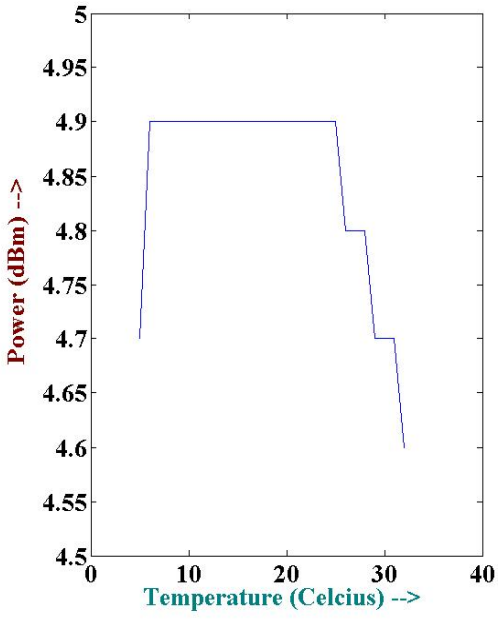

Figure 7.5(c): Bias Variation

Figure 7.5(d): Optical Power Variation

(Temperature Decreasing for First Transmitter)

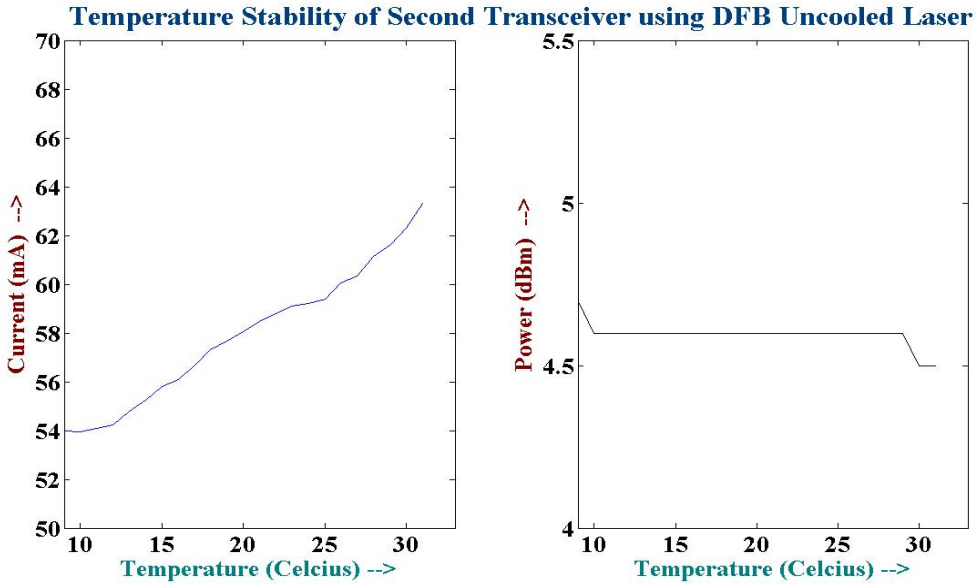

Figure 7.6(a): Bias Variation

Figure 7.6(b): Optical Power Variation

(Temperature Increasing for Second Transmitter)

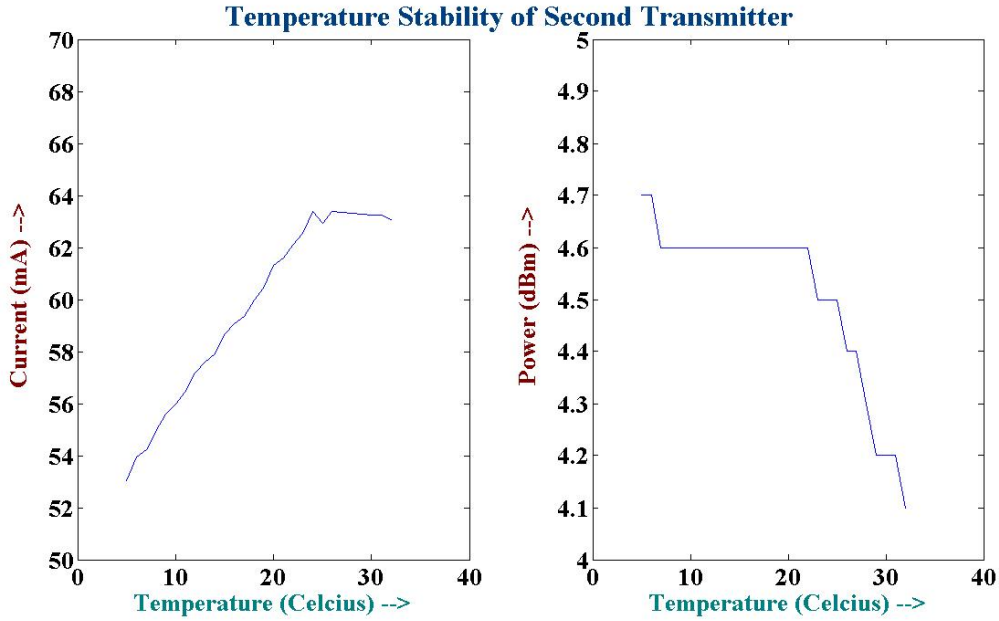

Figure 7.6(c): Bias Variation

Figure 7.6(d): Optical Power Variation

(Temperature Decreasing for Second Transmitter)

7.2. RF Characterization of DFB-Uncooled Laser:

For RF characterization of the DFB-Uncooled laser, a number of measurements have been carried out. These are explained in following sections.

7.2.1. Measurements of S-Parameters and determination of VSWR and Conversion Loss:

The block diagram of the arrangement for the measurements of the S-parameters of the link consisting of transmitter using DFB-Uncooled laser and Ortel receiver is shown in figure 7.7. The S-parameters are measured with the help of the Network Analyser as shown. The measured values of S_{11} and S_{21} are tabulated for different frequencies, as well as the calculated values of the VSWR and conversion losses are mentioned in table 7.3. The transceiver using DFB-Uncooled laser is shown in figure 7.8(a) and the total experimental set-up is shown in figure 7.8(b). The measured and frequency response of S_{11} and S_{21} are shown in figure 7.8(c) and 7.8(e) respectively; while the calculated VSWR is shown in figure 7.8(d). The Smith charts for different frequencies (450 MHz, 834.347 MHz and 70 MHz) are shown in figure 7.9. From the figure, it is shown that the impedance matching is the best for frequency is 70 MHz, while for other two frequencies; the matching is worse compared to the frequencies below 300 MHz.

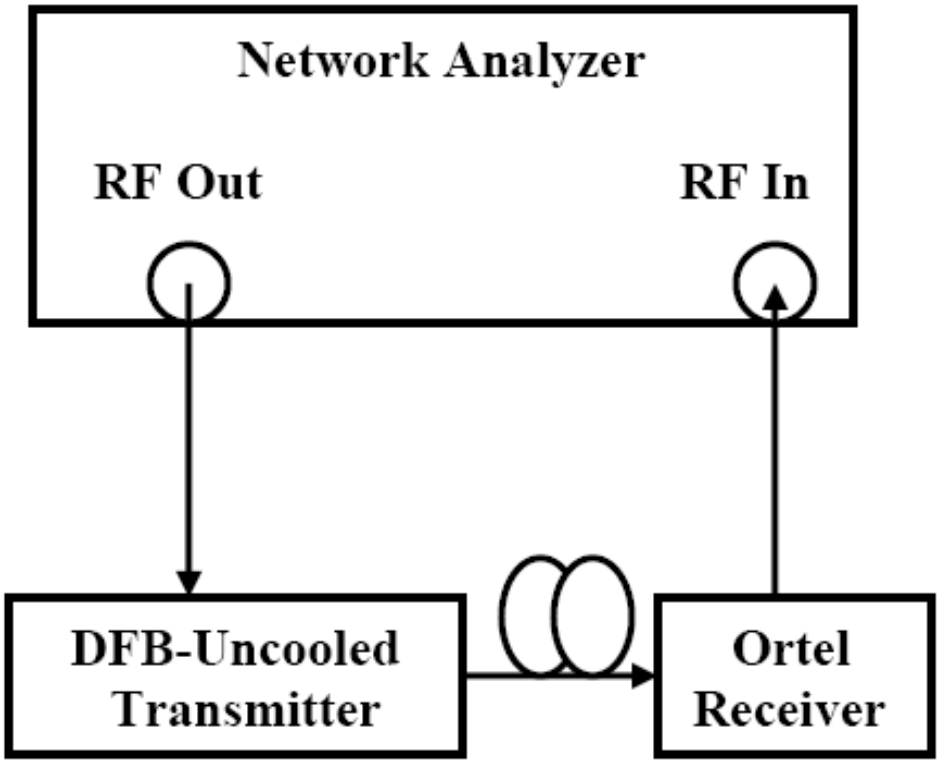

Figure 7.7: Block diagram of the setup for the measurement of S-parameters

Table 7.3

Network Analyser Used: HP 8714C

RF Power to the DFB-Uncooled Laser: 0 dBm

Frequency (MHz)	S_{11} (dB)	S_{21}(dB)	VSWR
10	-9.90	-37.42	1.2280
20	-16.20	-36.83	1.0492
30	-20.66	-36.92	1.0173
40	-24.66	-36.92	1.0069
50	-28.77	-36.91	1.0027
60	-33.42	-36.94	1.0009
70	-36.36	-36.95	1.0005
80	-33.80	-36.95	1.0008
90	-30.43	-36.96	1.0018
100	-27.87	-36.95	1.0033
150	-21.41	-37.00	1.0146
200	-18.21	-36.95	1.0307
250	-16.05	-37.04	1.0509
300	-14.11	-37.00	1.0808
350	-12.66	-36.85	1.1146
400	-11.21	-36.77	1.1638
450	-10.16	-36.45	1.2133
500	-9.04	-36.43	1.2850
550	-7.93	-36.04	1.3840
600	-6.83	-35.68	1.5236
650	-6.00	-35.50	1.6709
700	-5.48	-35.28	1.7899
750	-4.40	-35.00	2.1401
800	-3.90	-34.24	2.3748
850	-3.89	-34.19	2.3802
900	-4.51	-34.96	2.0960
950	-5.80	-35.88	1.7138
1000	-7.77	-38.03	1.4013

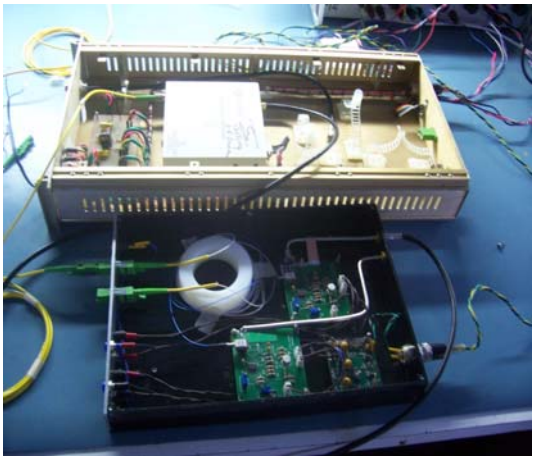

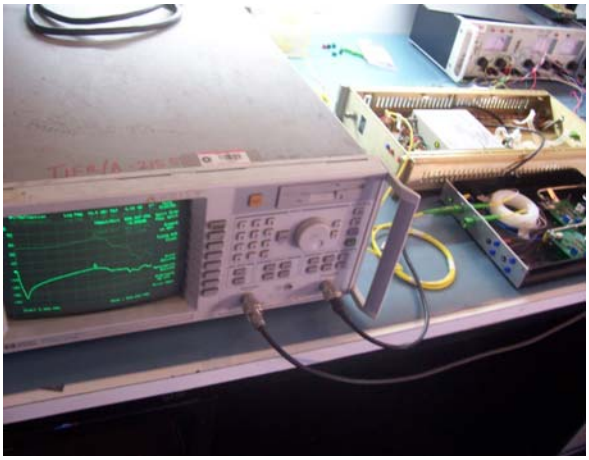

Figure 7.8(a): DFB-Uncooled-Based System **Figure 7.8(b):** Total experimental arrangement

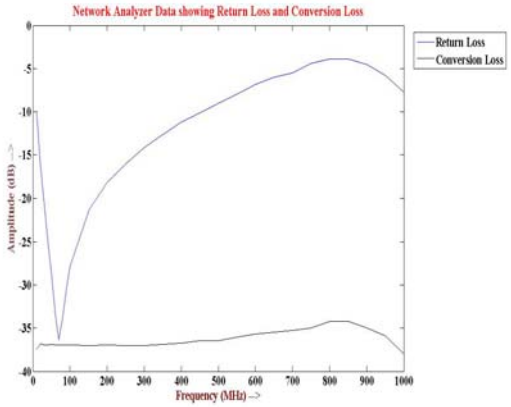

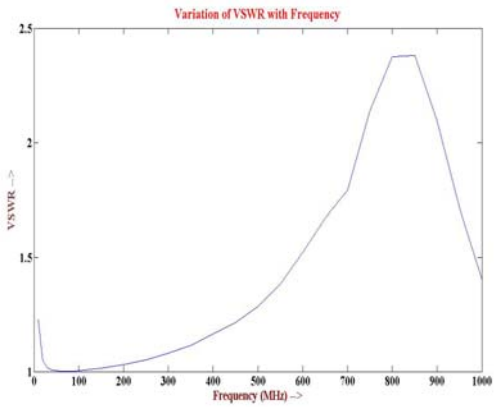

Figure 7.8(c): Plotted S_{11} and S_{21}

Figure 7.8(d): Frequency Response of VSWR

Figure 7.8(e): Frequency Response of S_{11} and S_{21}

Figure 7.9(a): Smith Chart at 450 MHz

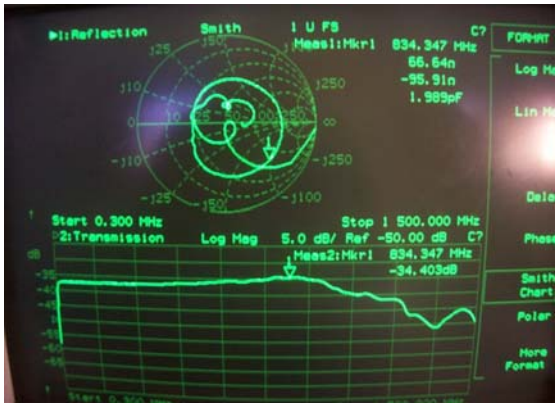

Figure 7.9(b): Smith Chart at 834.347 MHz

Figure 7.9(c): Smith Chart at 70 MHz

7.2.2. Determination of 1-dB Compression Point:

The block diagram and experimental setup of the arrangement for measurement of 1-dB compression point are shown in figure 7.10(a) and figure 7.10(b) respectively.

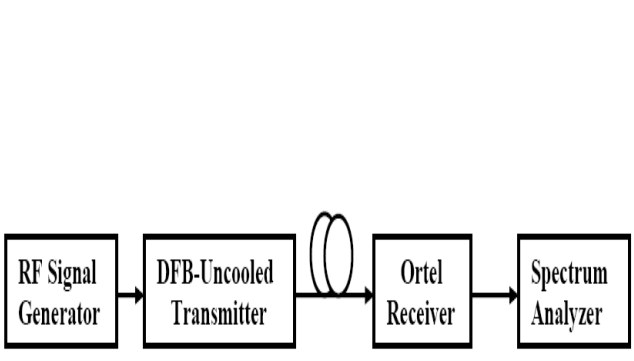

Figure 7.10(a): Block Diagram of the arrangement **Figure 7.10(b):** Total experimental setup

The experimental data are tabulated in table 7.4 and the result of the calculated Input 1-dB Compression Point is calculated from figure 7.11, which i +21-dBm.

Table 7.4

Spectrum Analyser Used: HP 8714C

RF Signal Generator Used: Agilent 8648D

RF generated from the Signal Generator: 500 MHz

Optical Power Output from DFB-Uncooled Transmitter: +4.6 dBm

Input Power (dBm)	Output Power (dBm)
-10	-46.85
-9	-45.88
-8	-44.89
-7	-43.90
-6	-42.93
-5	-41.55
-4	-40.56
-3	-39.56
-2	-38.56
-1	-37.57
0	-36.57
+1	-35.56
+2	-34.56
+3	-33.57
+4	-32.58
+5	-31.60
+6	-30.60
+7	-29.60
+8	-28.60
+9	-27.60
+10	-26.60
+11	-25.60
+12	-24.56
+13	-23.54

Input Power (dBm)	Output Power (dBm)
+14	-22.52
+15	-21.48
+16	-20.44
+17	-19.50
+18	-18.57
+19	-17.86
+20	-17.30
+21	-17.02

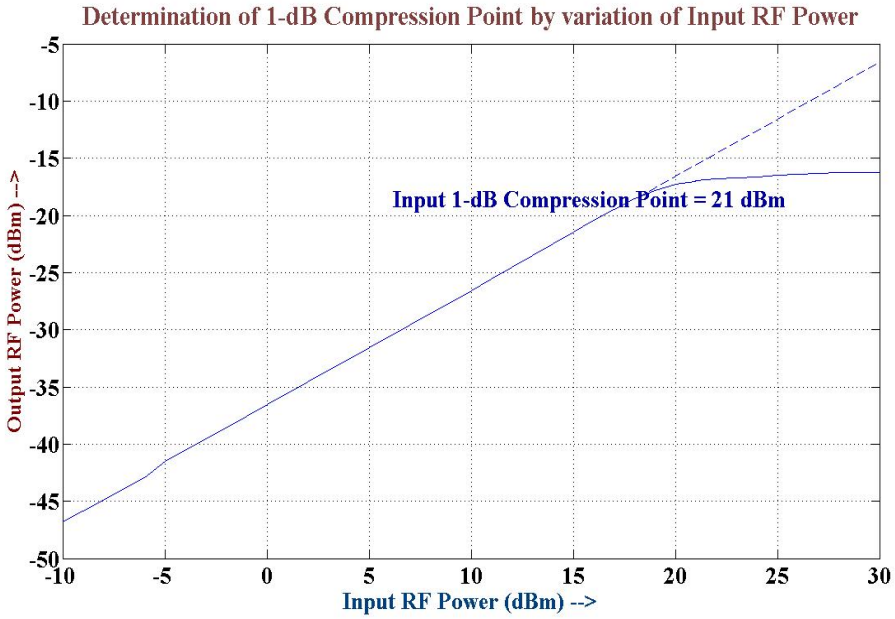

Figure 7.11: Experimental plot determining 1-dB Compression Point

7.2.3. Determination of Third-Order Intercept Point:

The block diagram and experimental setup of the arrangement for measurement of third-order intercept point are shown in figure 7.12 and figure 7.13 respectively. Two closely spaced frequencies, 500 and 501 MHz are combined and then fed to the transceiver. The experimental data are tabulated in table 7.5 and the result is shown in figure 7.14. The spectrum is shown in figure 7.15, where the third-order modulated components appear.

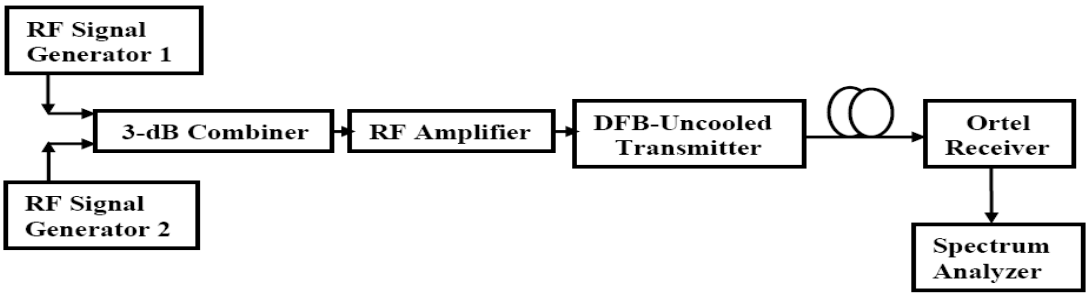

Figure 7.12: Block Diagram of the arrangement to measure third-order intercept point

Table 7.5

Spectrum Analyser Used: HP 8714C

RF Signal Generator Used: Agilent 8648D (Signal Generator 1)

Marconi Instruments 2031 (Signal Generator 2)

RF generated from the Signal Generator 1: 500 MHz

RF generated from the Signal Generator 2: 501 MHz

Optical Power Output from DFB-Uncooled Transmitter: +4.6 dBm

Input RF Power from Signal Generator 1 (dBm)	Input RF Power from Signal Generator 2 (dBm)	Output Power of Fundamental Frequency (dBm)	Output Power of Third-order product Frequency (dBm)
-30.0	-24.0	-41.42	-94.9
-29.5	-23.5	-40.87	-94.4
-29.0	-23.0	-40.37	-93.9
-28.5	-22.5	-39.83	-92
-28.0	-22.0	-39.36	-90.9
-27.5	-21.5	-38.77	-89.5
-27.0	-21.0	-38.31	-88.6
-26.5	-20.5	-37.76	-87.3
-26.0	-20.0	-37.19	-85.7

Figure 7.13: Experimental set-up for the arrangement

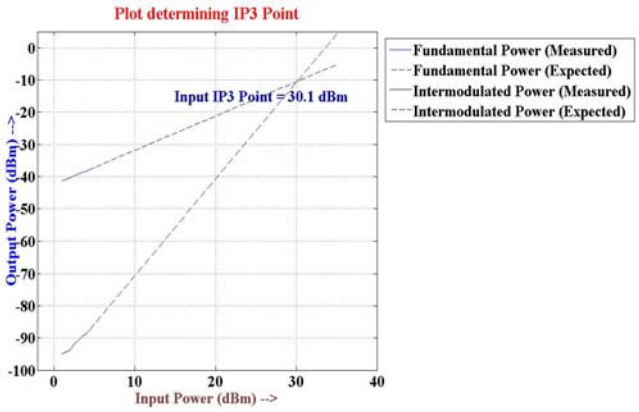

Figure 7.14: Determination of Third-order Intercept Point

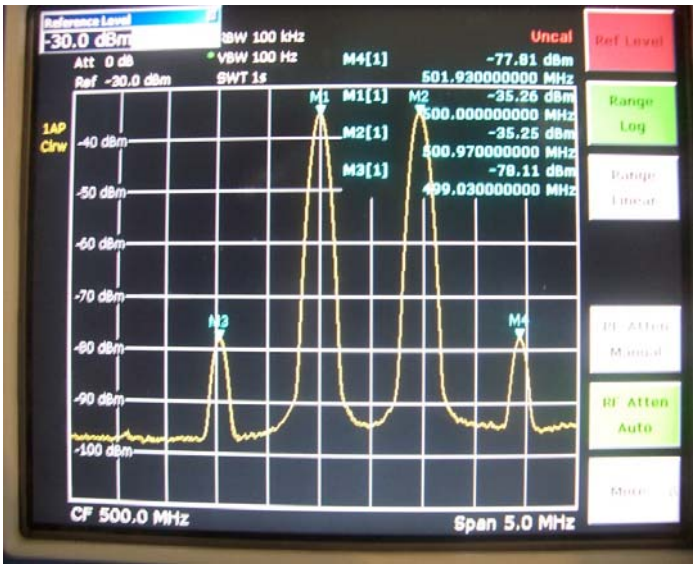

Figure 7.15: Spectrum of Third-order Product terms at 499 MHz and 502 MHz

7.2.4. Determination of Signal-To-Noise Ratio:

The block diagram of the arrangement for measurement of signal-to-noise ratio is shown in figure 7.16. Here, the attenuator is varied to change the optical power in the transceiver and keeping the RF input constant, the signal power has been noted with respect to the noise floor level. The RF power level is kept constant at 0 dBm. As the RF voltage varies in proportion with the optical power, the RF power changes by 2-dB with a 1-dB change in optical power level. The different values of Signal-to-Noise ratio (SNR) are tabulated in table 7.6 and the variation of SNR is plotted with respect to the optical power in the link in figure 7.17. The spectrum of such an instant is shown in figure 7.18. The SNR per unit bandwidth has also been calculated theoretically and the comparison has been plotted in figure 7.19.

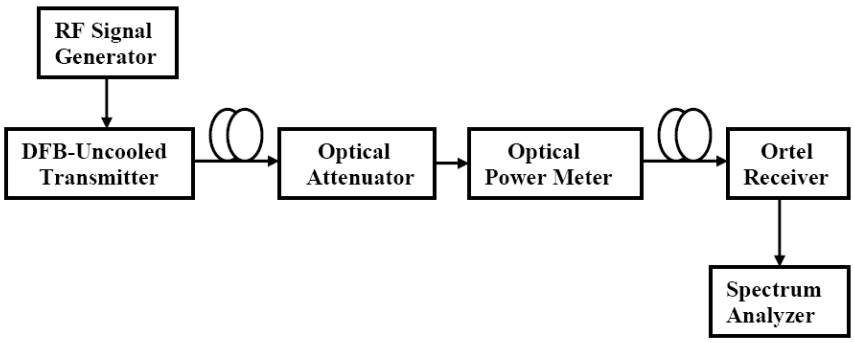

Figure 7.16: Block Diagram of the arrangement to measure signal-to-noise ratio

Table 7.6

Spectrum Analyser Used: HP 8714C

RF Signal Generator Used: Agilent 8648D

RF generated from the Signal Generator: 500 MHz

RF Power Used: 0 dBm

Noise Floor: -71.6 dBm

Resolution Bandwidth: 100 KHz

Optical Power (dBm)	Signal-To-Noise Ratio (dB)	Signal-To-Noise Ratio per unit bandwidth (dB/Hz)
+4	46.0	96.0
+3	44.3	94.3
+2	42.0	92.0
+1	40.5	90.5

Optical Power (dBm)	Signal-To-Noise Ratio (dB)	Signal-To-Noise Ratio per unit bandwidth (dB/Hz)
0	38.4	88.4
-1	36.6	86.6
-2	34.8	84.8
-3	32.8	82.8
-4	30.5	80.5
-5	28.8	78.8
-6	27.1	77.1
-7	25.0	75.0
-8	23.0	73.0
-9	21.1	71.1
-10	18.6	68.6
-11	16.5	66.5
-12	14.6	64.6
-13	12.7	62.7
-14	11.0	61.0
-15	8.8	58.8
-16	6.2	56.2
-17	5.0	55.0
-18	3.1	53.1

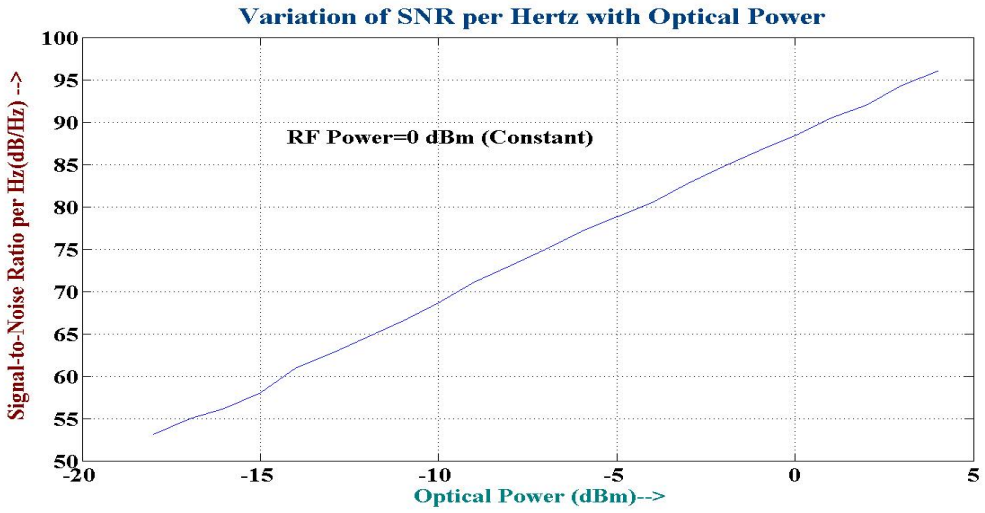

Figure 7.17: Variation of signal-to-noise ratio per unit bandwidth with Optical Power

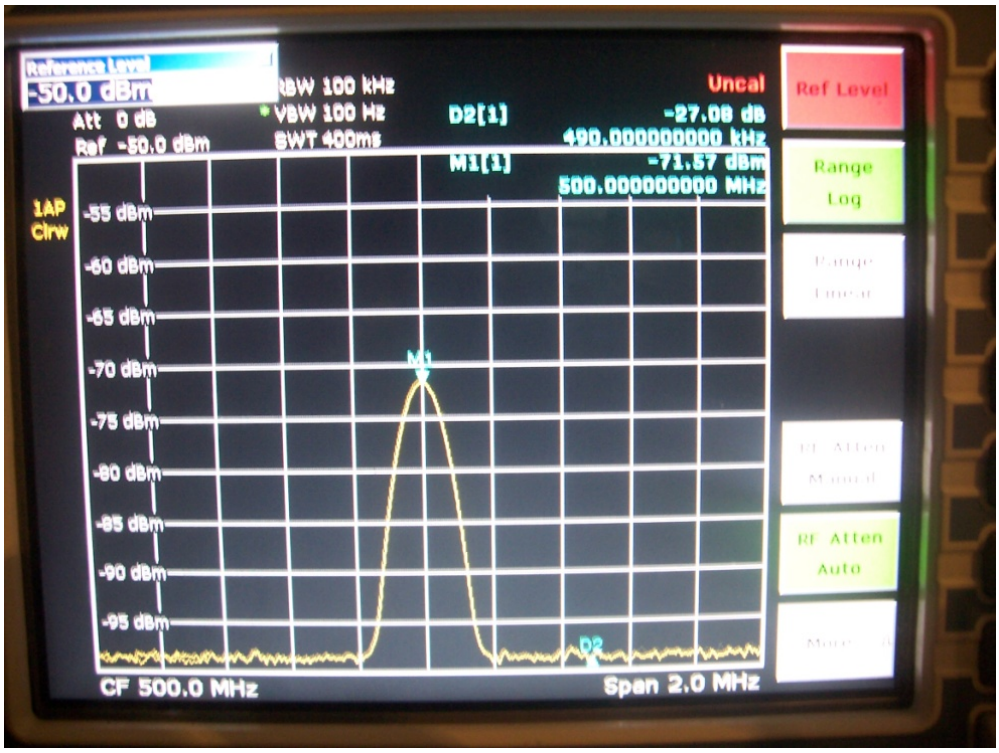

Figure 7.18: **Spectrum of Third-order Product terms at 499 MHz and 502 MHz**

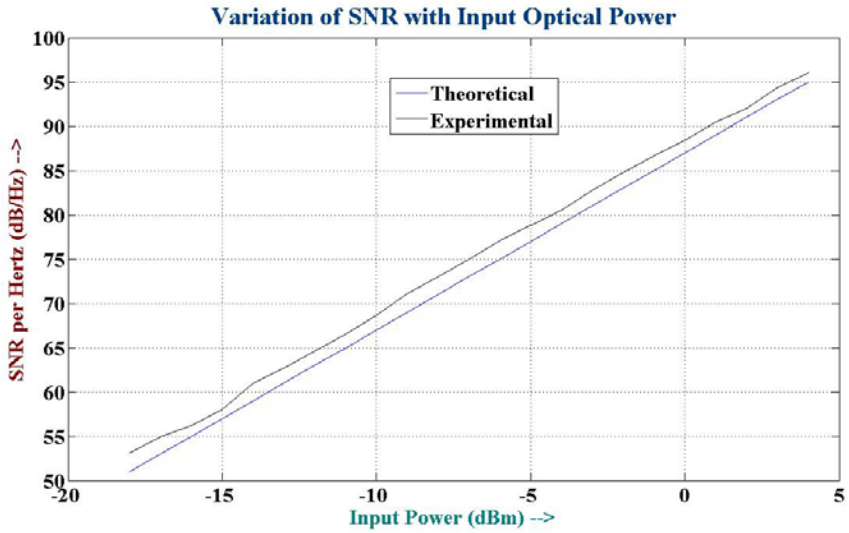

Figure 7.19: **Comparison of signal-to-noise ratio per unit bandwidth with Optical Power**

Chapter 8

Characterization of Pre-Amplifiers in DWDM System

8.1. RF Characterization of the Pre-Amplifiers in DWDM System:

The pre-amplifier chain in the DWDM system consists of two amplifiers and a 3-dB attenuator. As shown in figure 5.8, there is a pre-amplifier MSA0520 in the system, following a 3-dB power splitter, where the power has been divided to the IF system and the DWDM fiber-optic link. In DWDM fiber-optic system, the power has been amplified by an amplifier GALI 74 of gain of 22 dB to feed the RF power at the input of the Optical Transmitter. This system has been tested by Network Analyzer. The whole system developed in a PCB is shown in figure 8.1(a). There are two such units for receiving signals of two different polarizations in two signals. The overall system consisting of two units is shown in figure 8.1(b). The overall experimental arrangement is shown in figure 8.1(c) to test the return loss and the gain with the help of a Network Analyzer for the all GMRT operating frequencies.

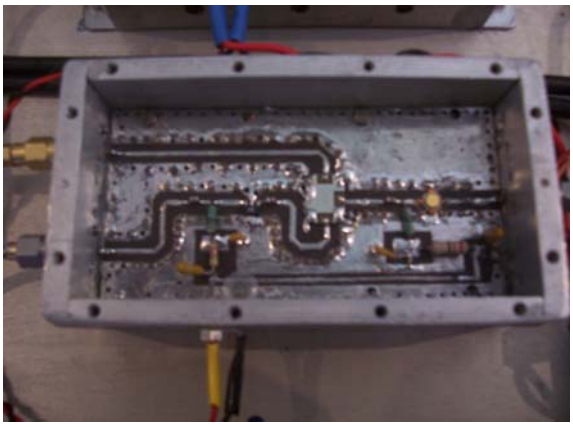

Figure 8.1(a): Pre-Amplifiers mounted in PCB

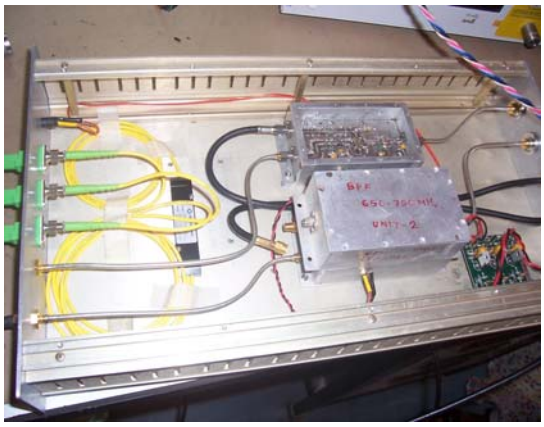

Figure 8.1(b): The whole unit

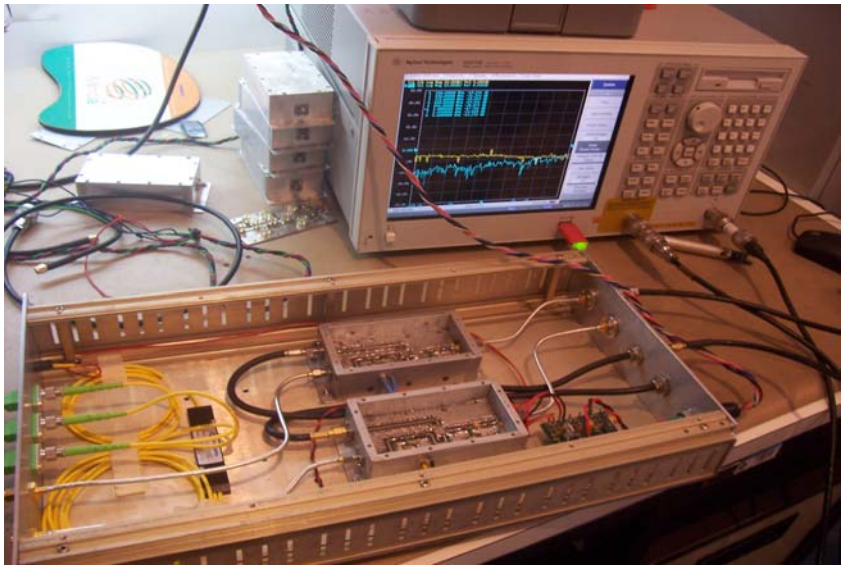

Figure 8.1(c): The experimental arrangement measuring the return loss and gain

The Network Analyzer used during the testing is ENA Series E5070B. The input power to the unit is -55 dBm. The return loss (S_{11}) and the gain (S_{21}) have been studied for the two channels (IF Path and DWDM Link) of the two units in the whole frequency band. A 10-dB RF attenuator is placed at the port of the Network Analyzer so that it would not be damaged. The images of IF Port and at the input of the Optical Transmitter for two units are shown in figure 8.2 for all the frequency bands of GMRT.

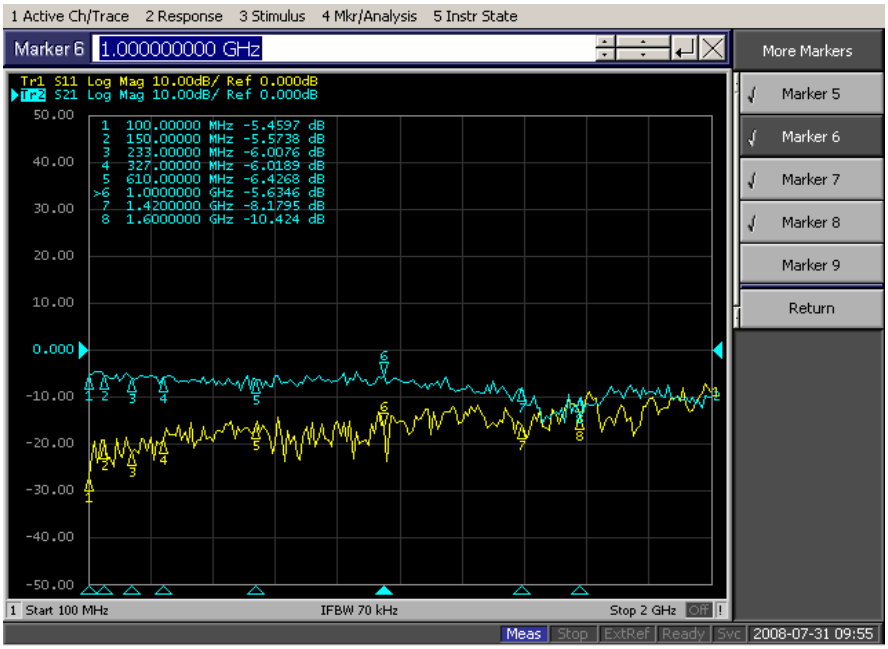

Figure 8.2(a): Response in the IF Port of the first unit

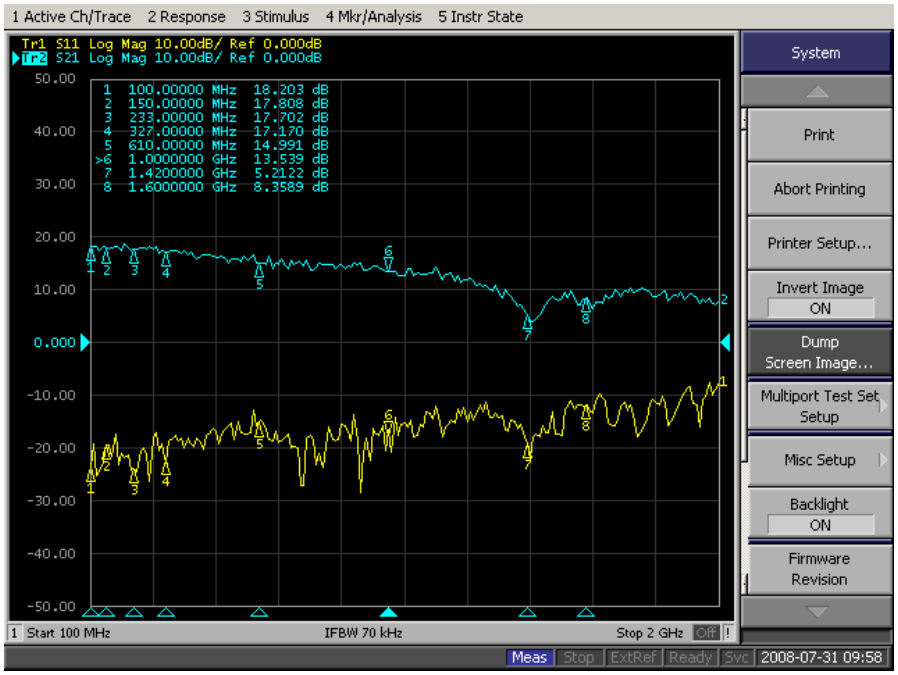

Figure 8.2(b): Response in the Input Port of Optical Transmitter of the first unit

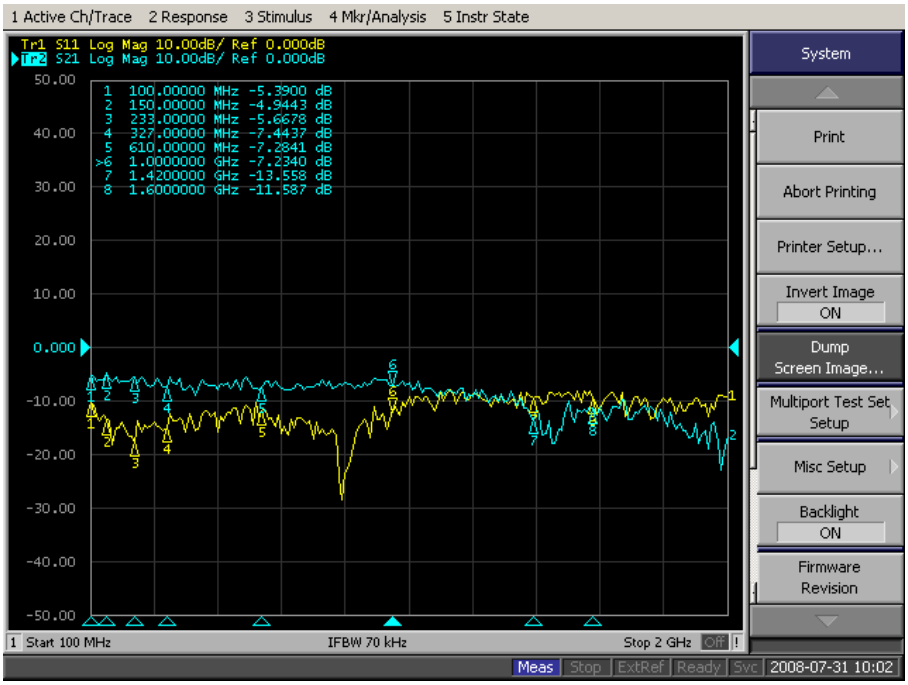

Figure 8.2(c): Response in the IF Port of the second unit

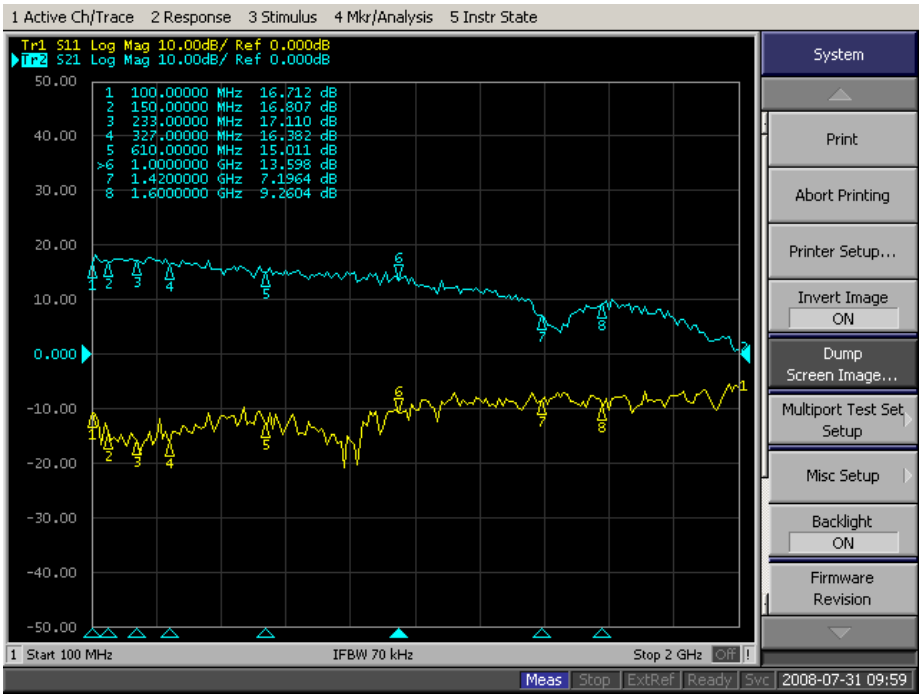

Figure 8.2(d): Response in the Input Port of Optical Transmitter of the second unit

Chapter 9

Characterization of the DWDM System in Antenna and Receiver Room

9.1. Characterization of the DWDM-Based Broadband System:

The DWDM fibre-optic links as well as the WDM bidirectional link have been established in three antennas of the GMRT antennas. These are C5, C14 and W4. In the C5 antenna, instead of Gali52 Amplifier in the broadband link, Gali74 has been used which has a gain of 15 dB. The powers in the front end, Optical Transmitter Input (OTx), IF system and receiver system in the receiver room (ORx) have been measured for two channels, which is tabulated in table 9.1. The different spectrum for channels 1 and 2 for different operating frequencies are shown in figure 9.1.

Table 9.1

(C-5 Antenna)

Operating Frequency	Power in Channel 1 (dBm)				Power in Channel 2 (dBm)			
(MHz)	Front End	OTx Input	IF Output	ORx Output	Front End	OTx Input	IF Output	ORx Output
150	-56	-35	-50	-46	-54	-32	-52	-44
233	-57	-38	-52	-52	-52	-33	-55	-42
327	-55	-34	-52	-59	-54	-30	-52	-56
610	-58	-42	-56	-63	-60	-37	-60	-61
1060	-57	-40	-54	-62	-62	-40	-61	-62
1170	-60	-43	-57	-68	-64	-42	-61	-68
1280	-63	-45	-63	-71	-65	-48		-72
1390	-69	-50	-67	-75	-69	-50	-72	-73
1420 (Full L-Band)	-52	-33	-49	-58	-52	-30	-50	-57

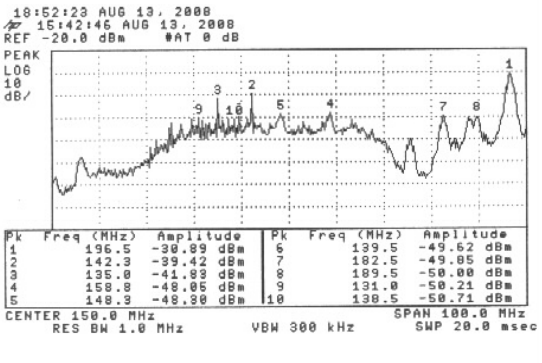

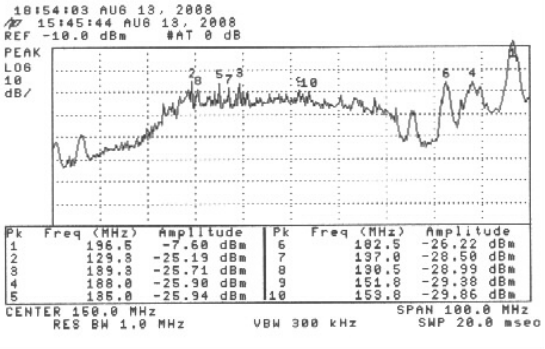

Figure 9.1.1: Channel-1 150 MHz Front End

Figure 9.1.2: Channel-1 150 MHz OTx

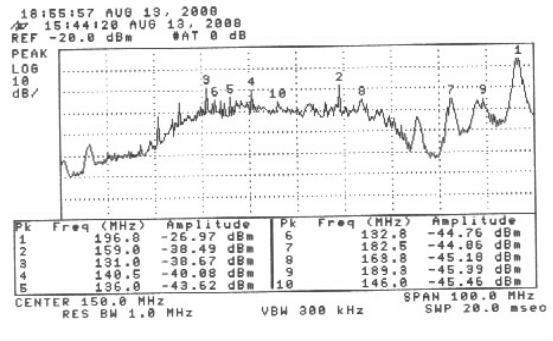

Figure 9.1.3: **Channel-1 150 MHz IF**

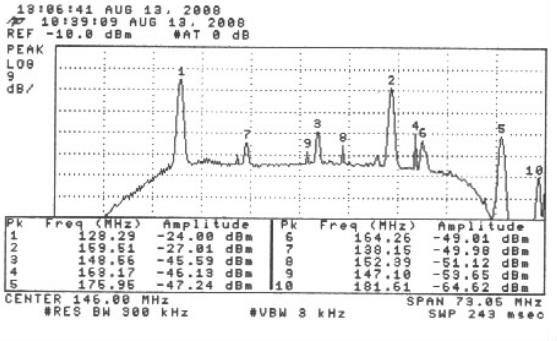

Figure 9.1.4: **Channel-1 150 MHz ORx**

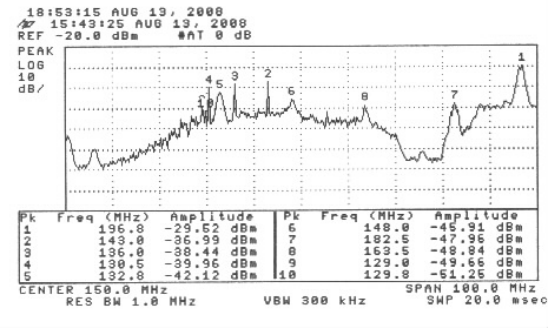

Figure 9.1.5: **Channel-2 150 MHz Front End**

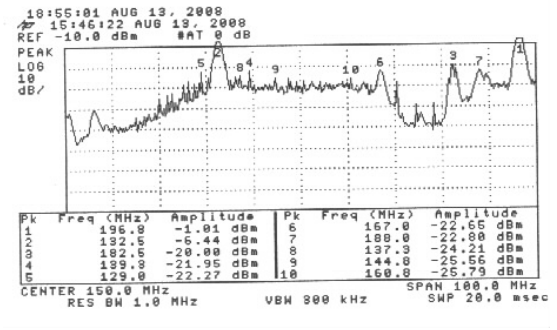

Figure 9.1.6: **Channel-2 150 MHz OTx**

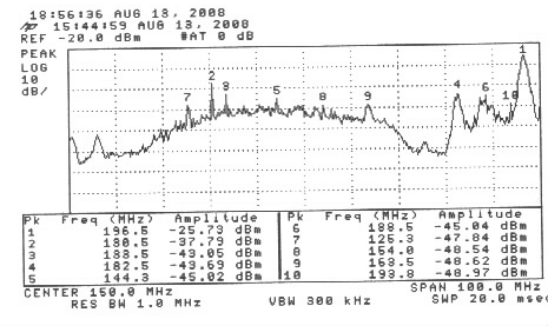

Figure 9.1.7: **Channel-2 150 MHz IF**

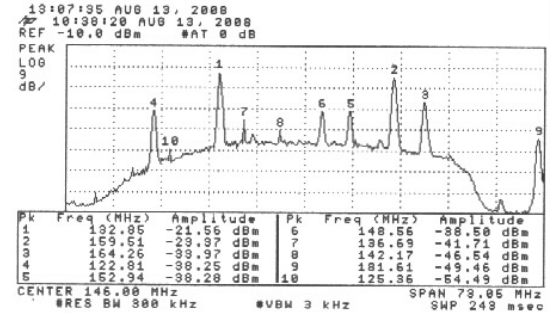

Figure 9.1.8: **Channel-2 150 MHz ORx**

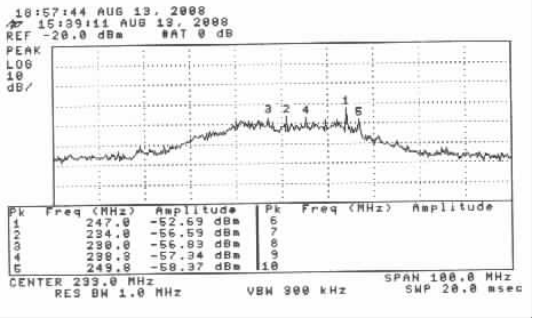

Figure 9.1.9: **Channel-1 233 MHz Front End**

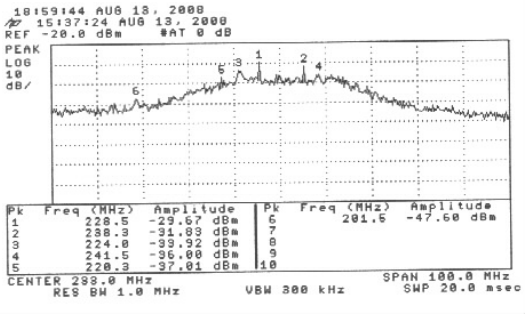

Figure 9.1.10: **Channel-1 233 MHz OTx**

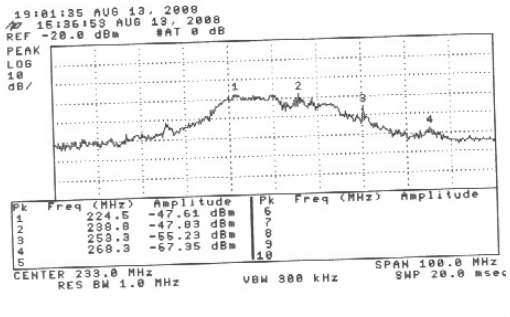

Figure 9.1.11: Channel-1 233 MHz IF

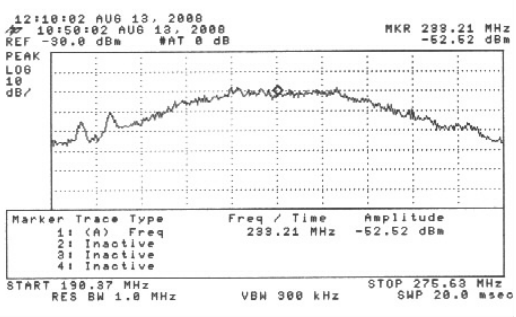

Figure 9.1.12: Channel-1 233 MHz ORx

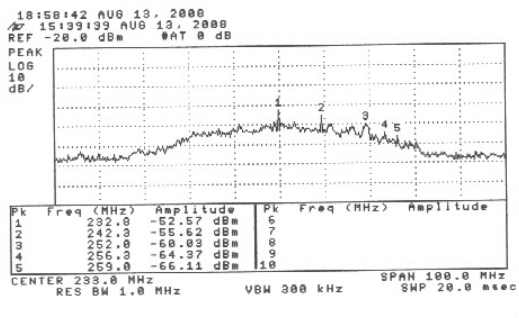

Figure 9.1.13: Channel-2 233 MHz Front End

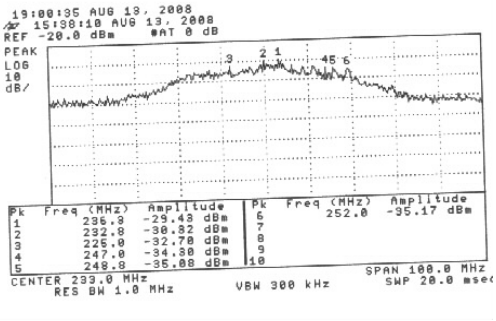

Figure 9.1.14: Channel-2 233 MHz OTx

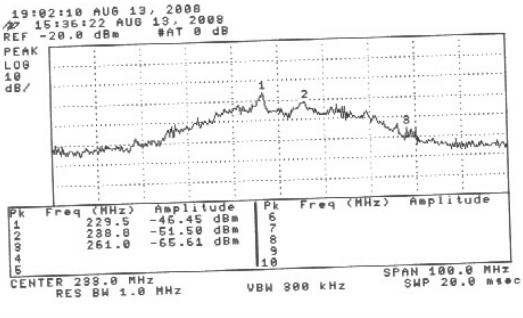

Figure 9.1.15: Channel-2 233 MHz IF

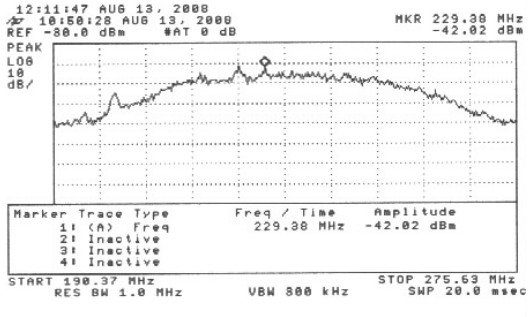

Figure 9.1.16: Channel-2 233 MHz ORx

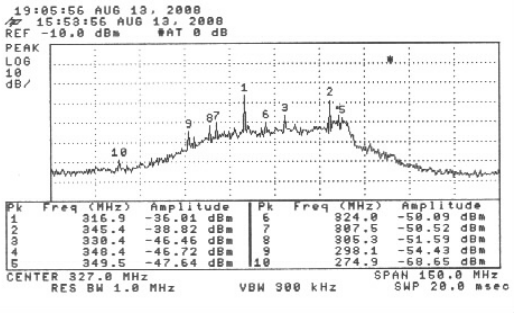

Figure 9.1.17: Channel-1 327 MHz Front End

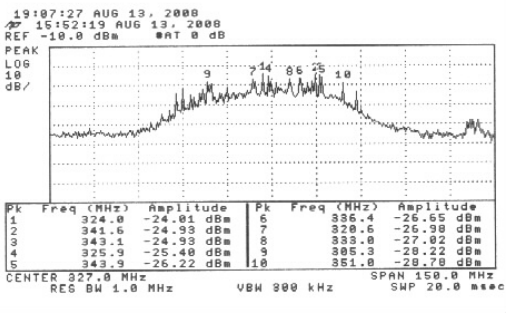

Figure 9.1.18: Channel-1 327 MHz OTx

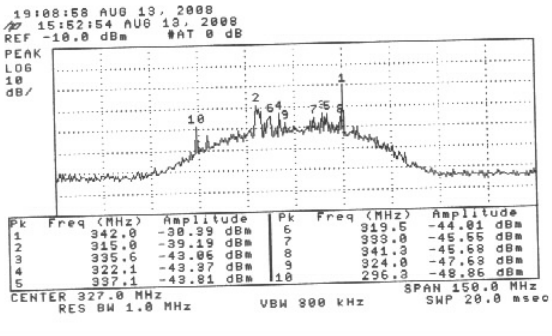

Figure 9.1.19: **Channel-1 327 MHz IF**

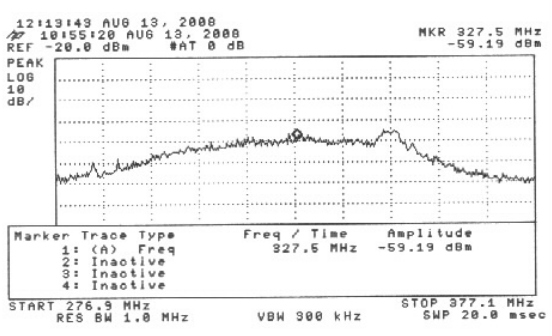

Figure 9.1.20: **Channel-1 327 MHz ORx**

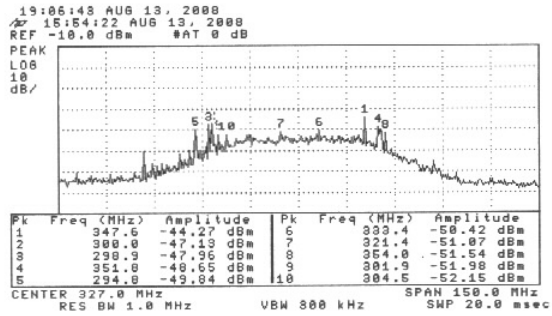

Figure 9.1.21: **Channel-2 327 MHz Front End**

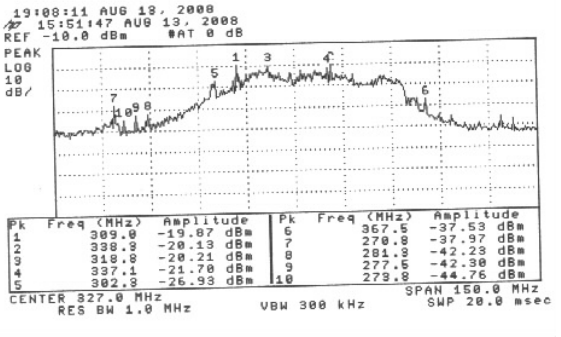

Figure 9.1.22: **Channel-2 327 MHz OTx**

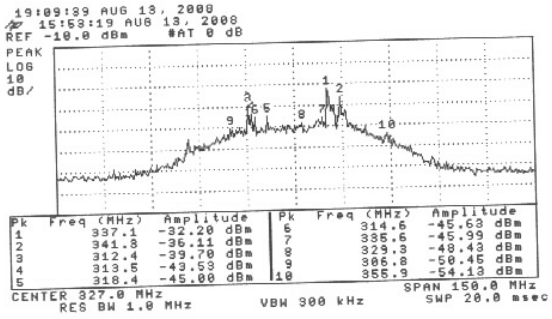

Figure 9.1.23: **Channel-2 327 MHz IF**

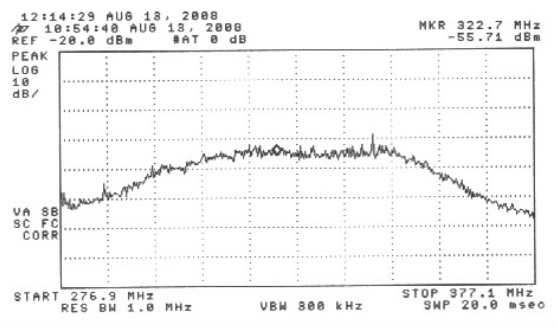

Figure 9.1.24: **Channel-2 327 MHz ORx**

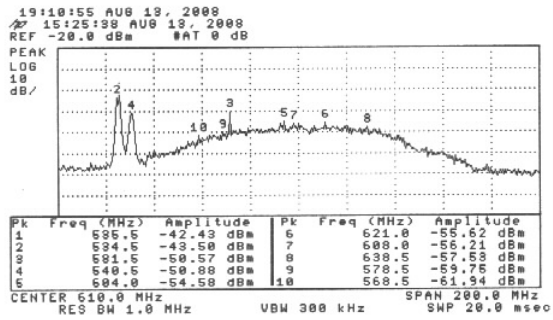

Figure 9.1.25: **Channel-1 610 MHz Front End**

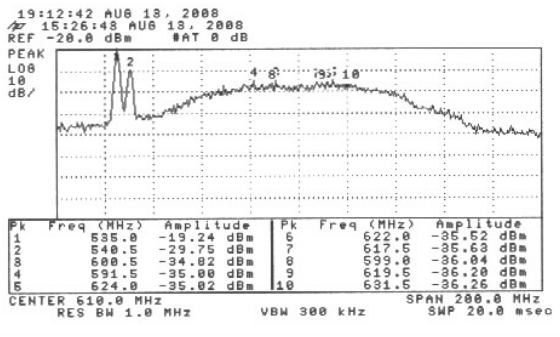

Figure 9.1.26: **Channel-1 610 MHz OTx**

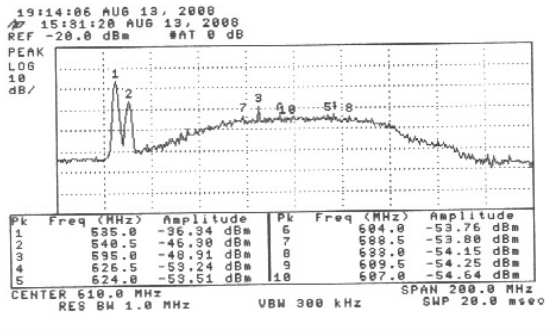

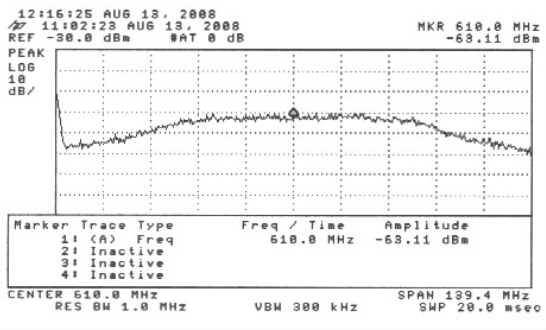

Figure 9.1.27: Channel-1 610 MHz IF

Figure 9.1.28: Channel-1 610 MHz ORx

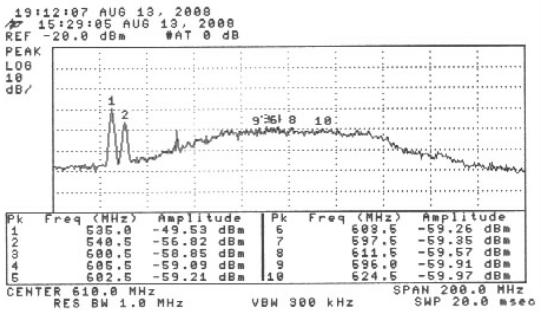

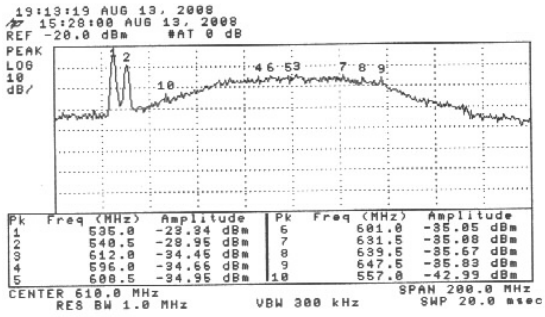

Figure 9.1.29: Channel-2 610 MHz Front End

Figure 9.1.30: Channel-2 610 MHz OTx

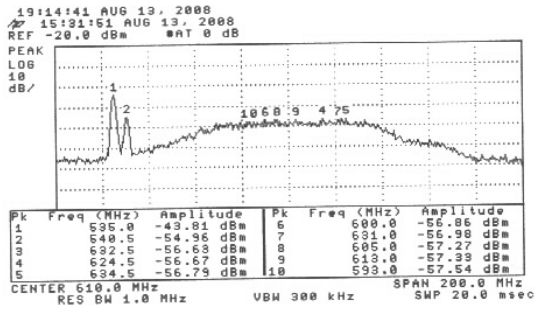

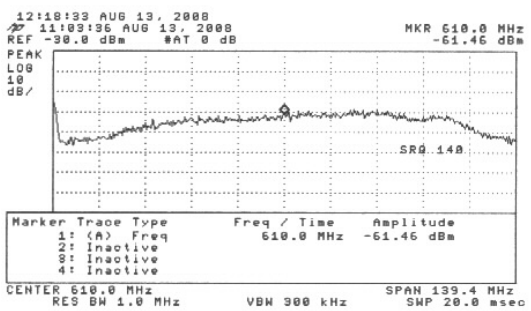

Figure 9.1.31: Channel-2 610 MHz IF

Figure 9.1.32: Channel-2 610 MHz ORx

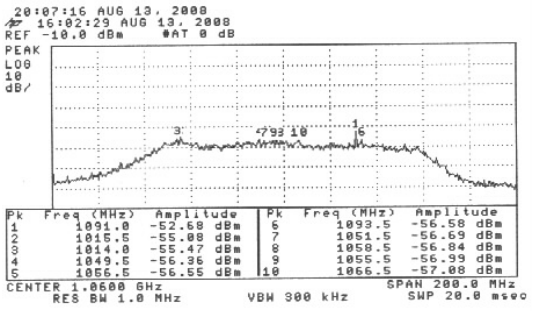

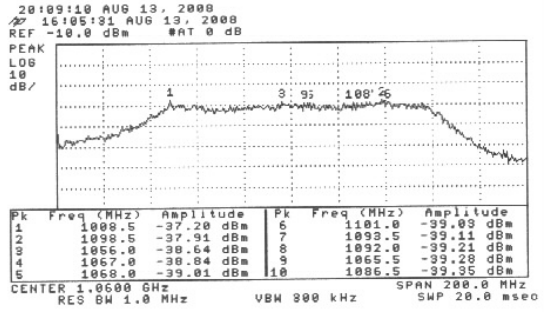

Figure 9.1.33: Channel-1 1060 MHz Front End

Figure 9.1.34: Channel-1 1060 MHz OTx

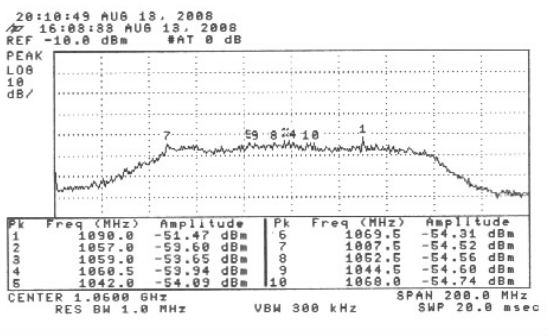

Figure 9.1.35: Channel-1 1060 MHz IF

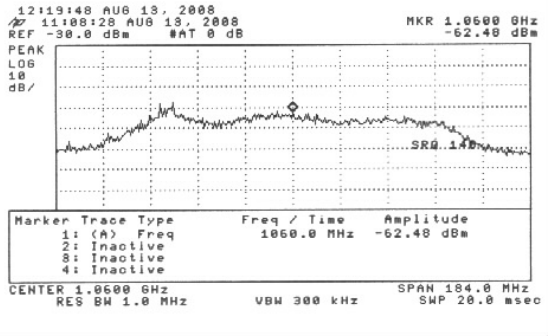

Figure 9.1.36: Channel-1 1060 MHz ORx

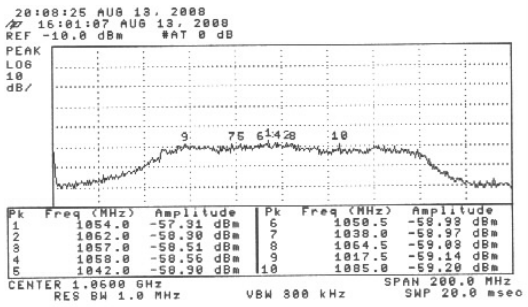

Figure 9.1.37: Channel-1 1060 MHz Front End

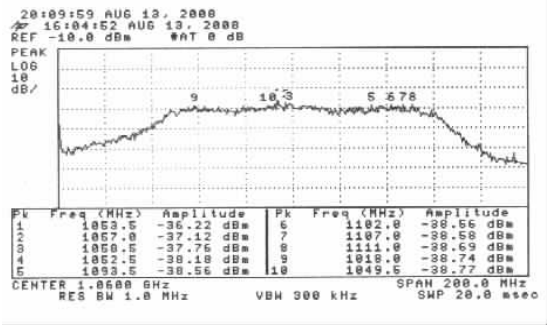

Figure 9.1.38: Channel-2 1060 MHz OTx

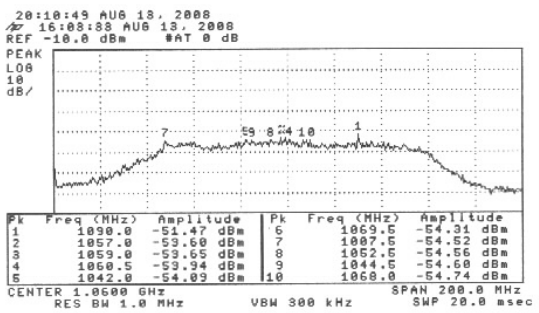

Figure 9.1.39: Channel-2 1060 MHz IF

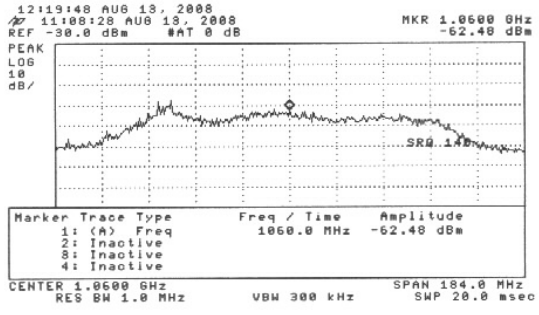

Figure 9.1.40: Channel-2 1060 MHz ORx

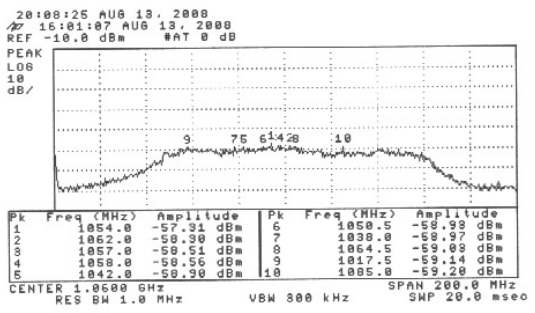

Figure 9.1.41: Channel-1 1170 MHz Front End

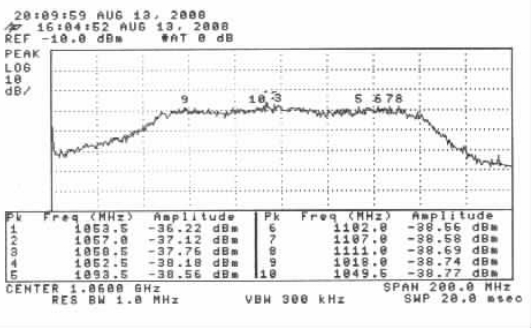

Figure 9.1.42: Channel-1 1170 MHz OTx

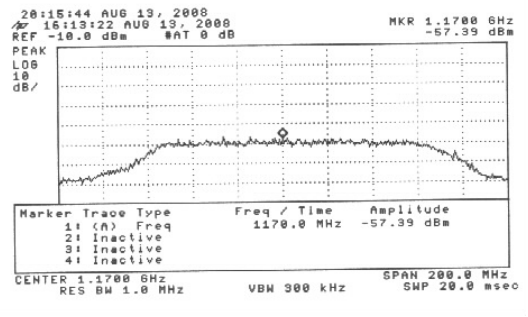

Figure 9.1.43: Channel-1 1170 MHz IF

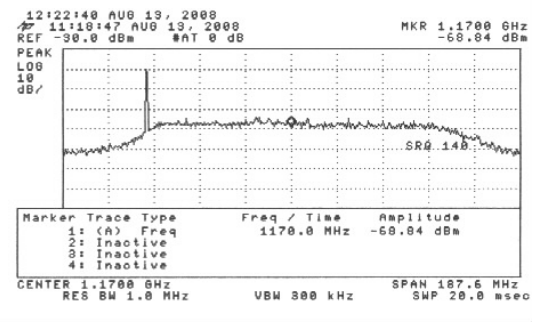

Figure 9.1.44: Channel-1 1170 MHz ORx

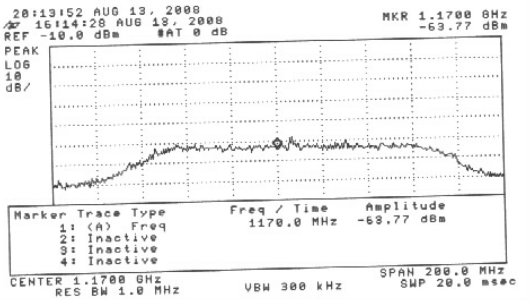

Figure 9.1.45: Channel-2 1170 MHz Front End

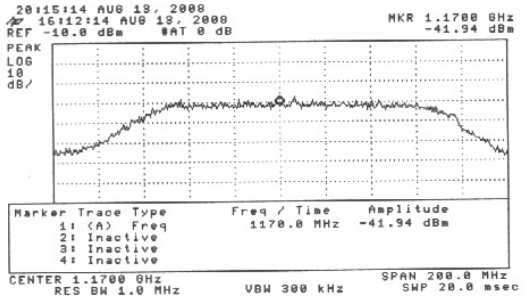

Figure 9.1.46: Channel-2 1170 MHz OTx

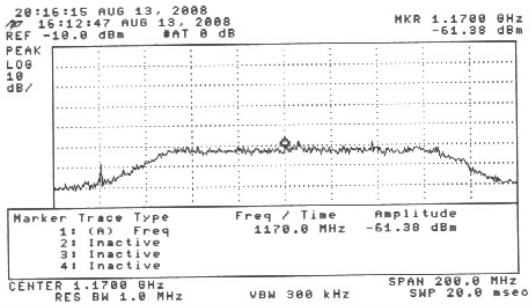

Figure 9.1.47: Channel-2 1170 MHz IF

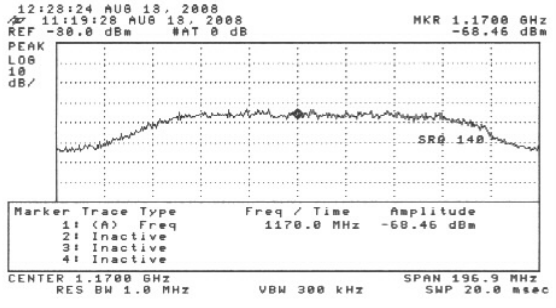

Figure 9.1.48: Channel-2 1170 MHz ORx

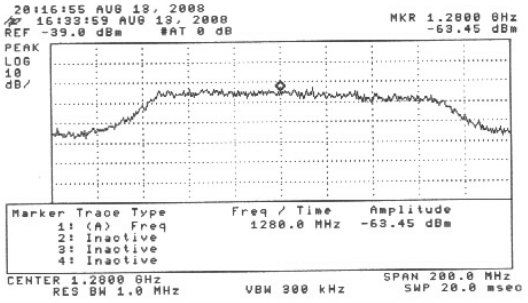

Figure 9.1.49: Channel-1 1280 MHz Front End

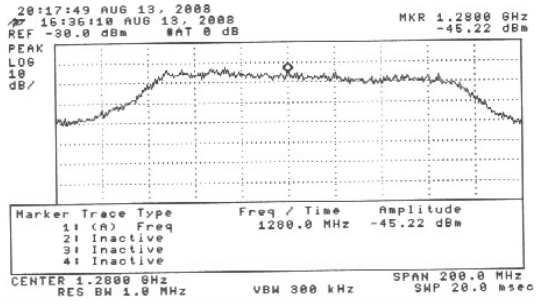

Figure 9.1.50: Channel-1 1280 MHz OTx

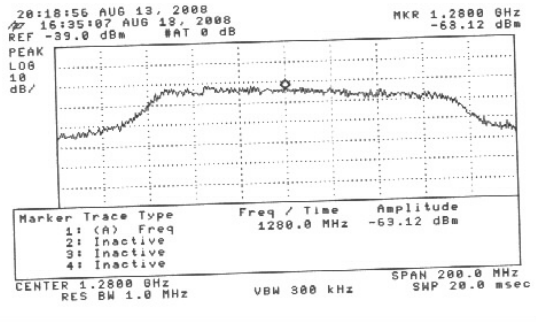

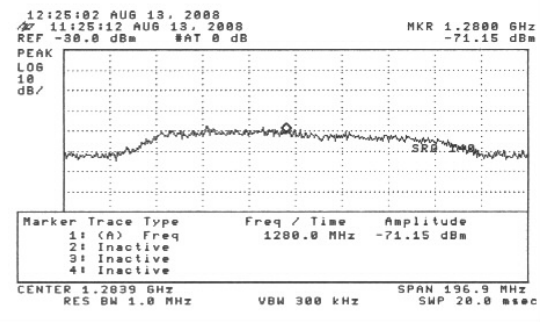

Figure 9.1.51: Channel-1 1280 MHz IF

Figure 9.1.52: Channel-1 1280 MHz ORx

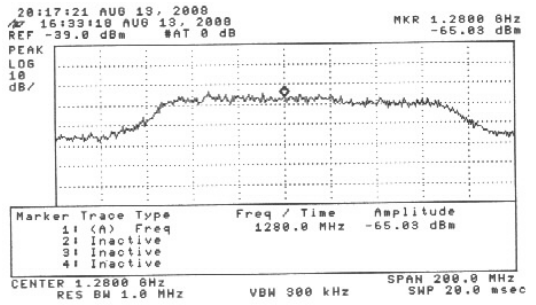

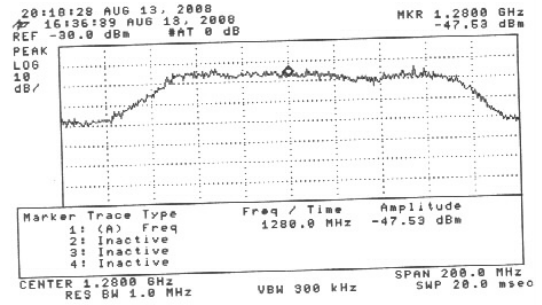

Figure 9.1.53: Channel-2 1280 MHz Front End

Figure 9.1.54: Channel-2 1280 MHz OTx

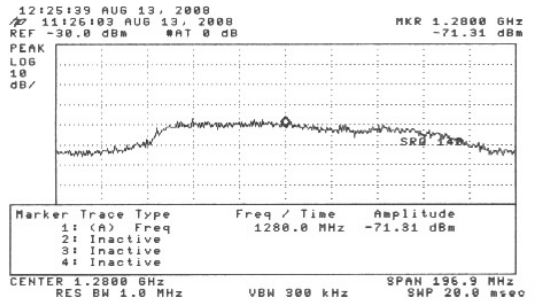

Figure 9.1.55: Channel-2 1280 MHz ORx

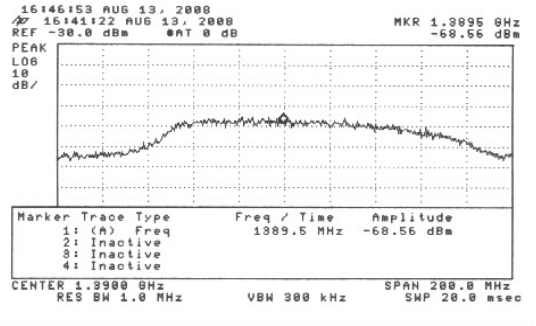

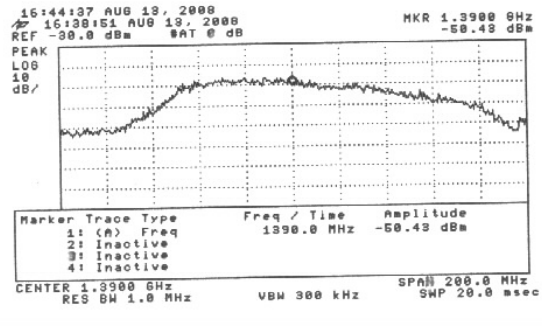

Figure 9.1.56: Channel-1 1390 MHz Front End

Figure 9.1.57: Channel-1 1390 MHz OTx

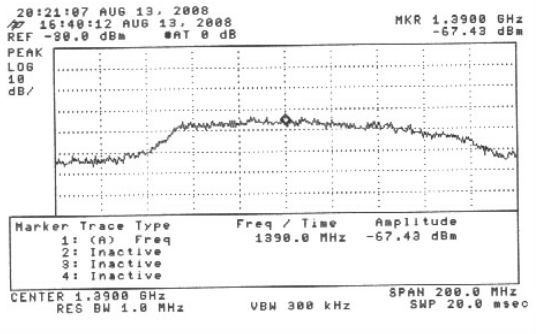

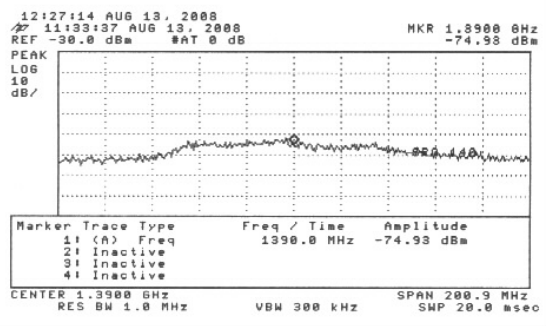

Figure 9.1.58: **Channel-1 1390 MHz IF**

Figure 9.1.59: **Channel-1 1390 MHz ORx**

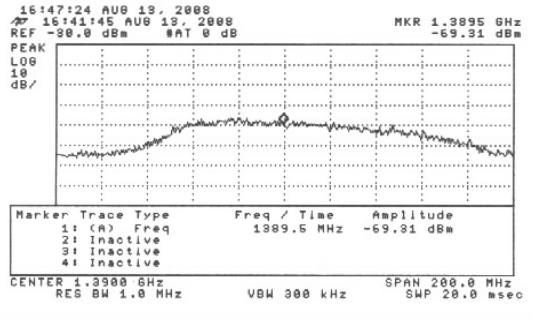

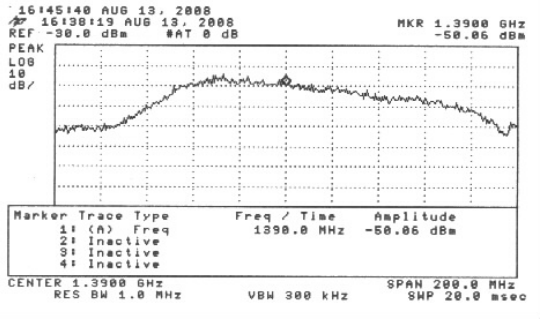

Figure 9.1.60: **Channel-2 1390 MHz Front End**

Figure 9.1.61: **Channel-2 1390 MHz OTx**

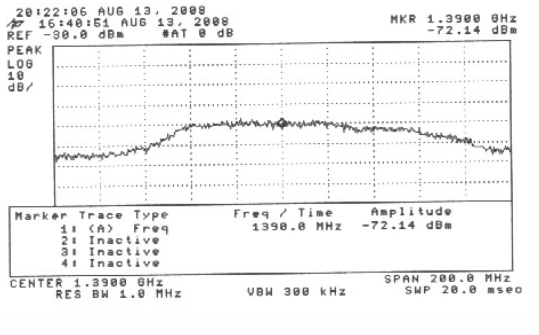

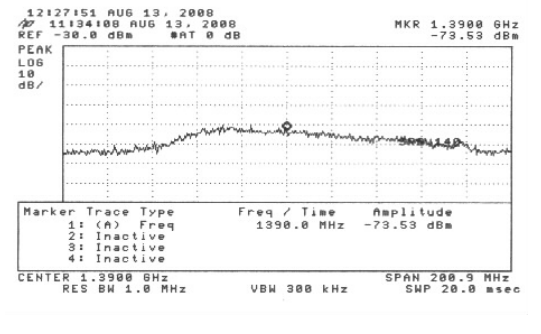

Figure 9.1.62: **Channel-2 1390 MHz IF**

Figure 9.1.63: **Channel-2 1390 MHz ORx**

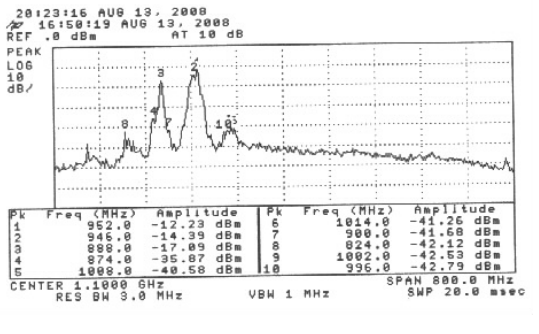

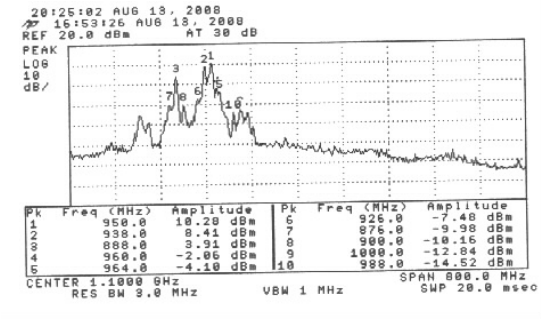

Figure 9.1.64: **Channel-1 1420 MHz Front End**

Figure 9.1.65: **Channel-1 1420 MHz OTx**

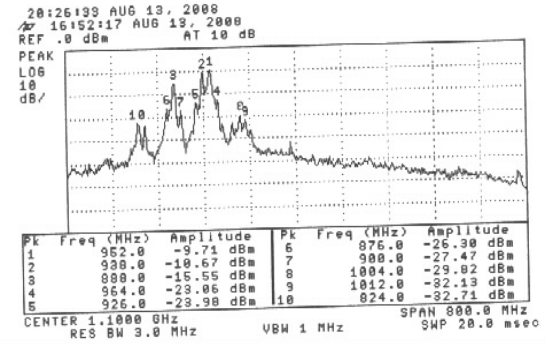

Figure 9.1.66: **Channel-1 1420 MHz IF**

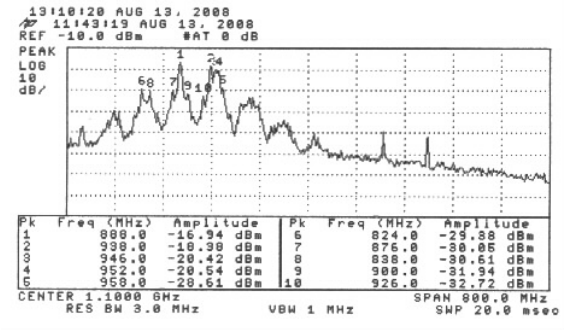

Figure 9.1.67: **Channel-1 1420 MHz ORx**

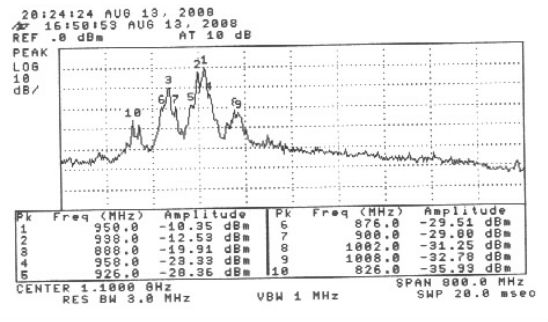

Figure 9.1.68: **Channel-2 1420 MHz Front End**

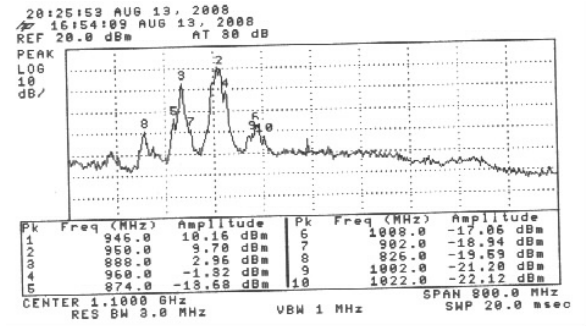

Figure 9.1.69: **Channel-2 1420 MHz OTx**

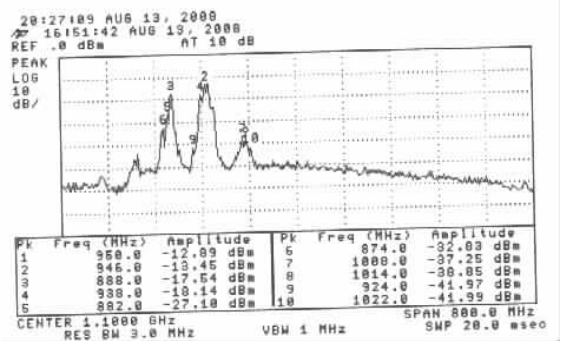

Figure 9.1.70: **Channel-2 1420 MHz IF**

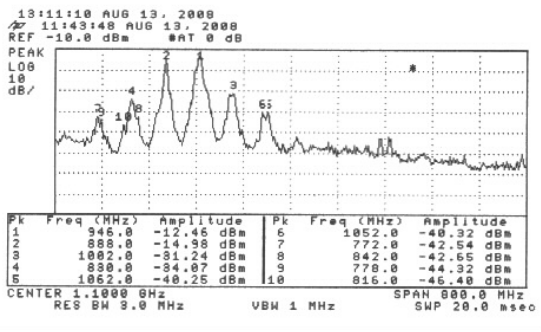

Figure 9.1.71: **Channel-2 1420 MHz ORx**

The same characterizations have been done for C-11 antenna. But, for this antenna, it has been found that the channel-1 is not performing satisfactorily after 610 MHz. So, the characterization is done for only one channel i.e., channel-2. The power levels at the every point of different stages (Front End Output, OTx Input, IF Input and ORx Output) are noticed and tabulated in table 9.2. The spectrums at these different stages for all the operating frequencies of GMRT are shown in figure 9.2.

Table 9.2

(C-11 Antenna)

Operating Frequency	Power in Channel 2 (dBm)			
(MHz)	Front End	OTx Input	IF Output	ORx Output
150	-60	-37	-57	-57
233	-68	-40	-63	-52
327	-57	-36	-55	-56
610	-66	-42	-62	-61
1060	-65	-43	-62	-64
1170	-70	-45	-68	-67
1280	-69	-49	-69	-68
1390	-75	-57	-72	-74
1420 (Full L-Band)	-62	-38	-58	-55

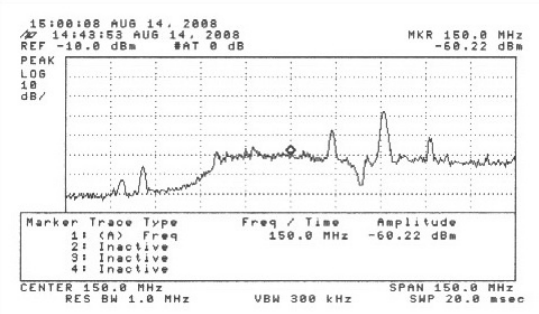

Figure 9.2.1: Channel-2 150 MHz Front End

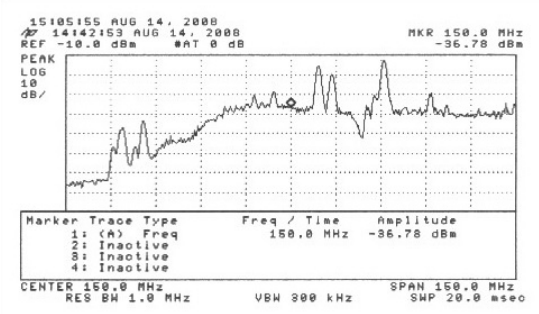

Figure 9.2.2: Channel-2 150 MHz OTx

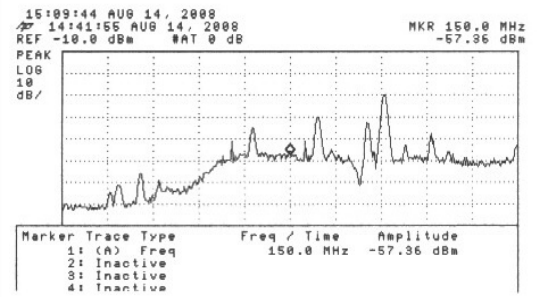

Figure 9.2.3: Channel-2 150 MHz IF

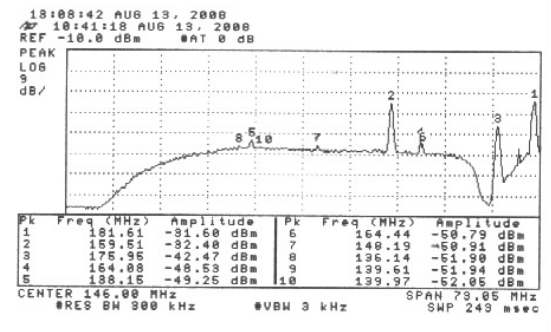

Figure 9.2.4: Channel-2 150 MHz ORx

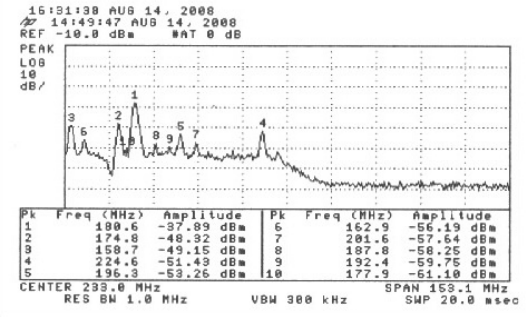

Figure 9.2.5: Channel-2 233 MHz Front End

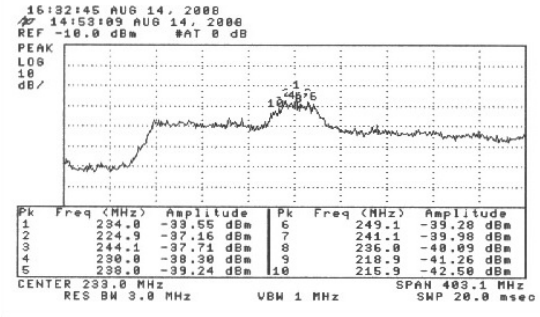

Figure 9.2.6: Channel-2 233 MHz OTx

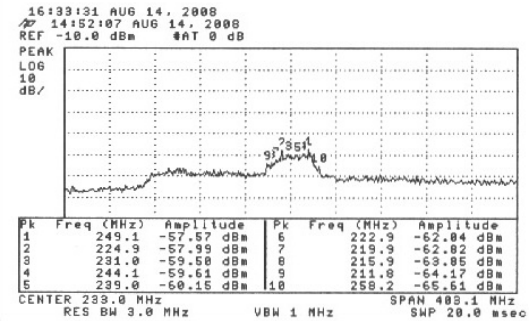

Figure 9.2.7: Channel-2 233 MHz IF

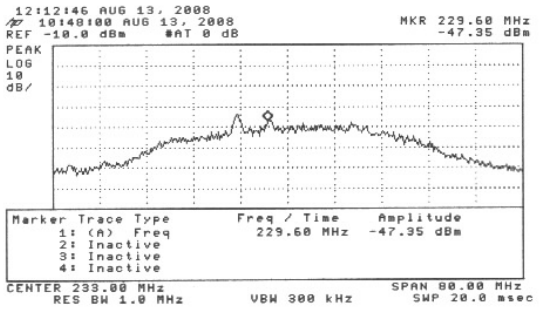

Figure 9.2.8: Channel-2 233 MHz ORx

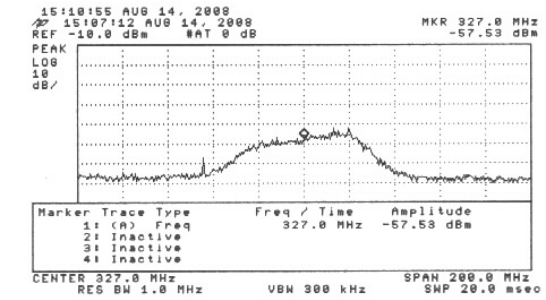

Figure 9.2.9: Channel-2 327 MHz Front End

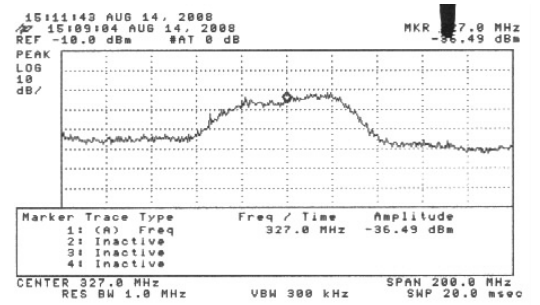

Figure 9.2.6: Channel-2 327 MHz OTx

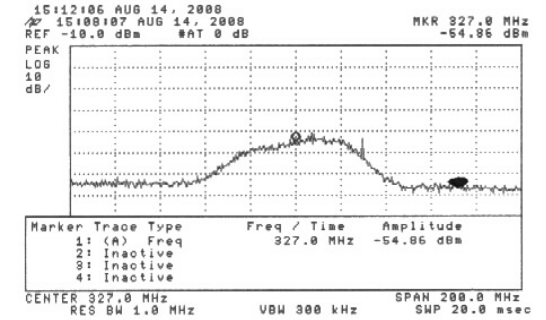

Figure 9.2.11: Channel-2 233 MHz IF

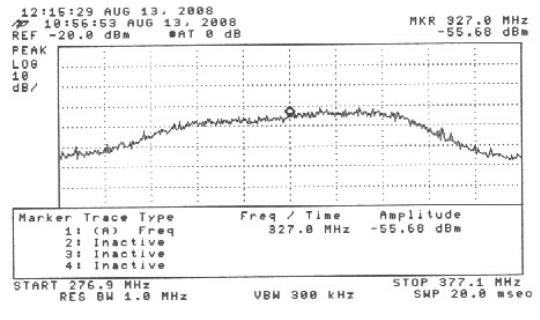

Figure 9.2.12: Channel-2 233 MHz ORx

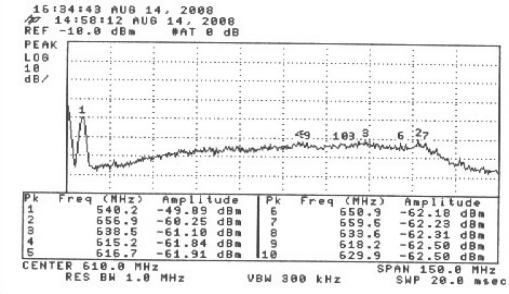

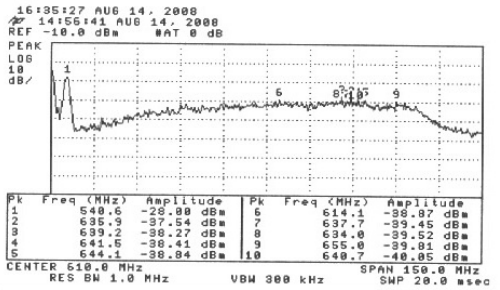

Figure 9.2.13: Channel-2 610 MHz Front End **Figure 9.2.14: Channel-2 610 MHz OTx**

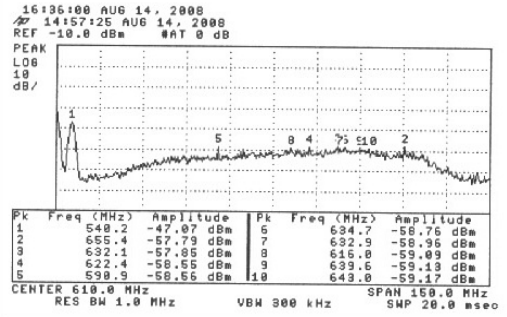

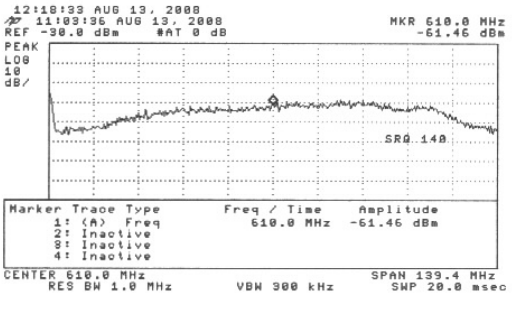

Figure 9.2.15: Channel-2 610 MHz IF **Figure 9.2.16: Channel-2 610 MHz ORx**

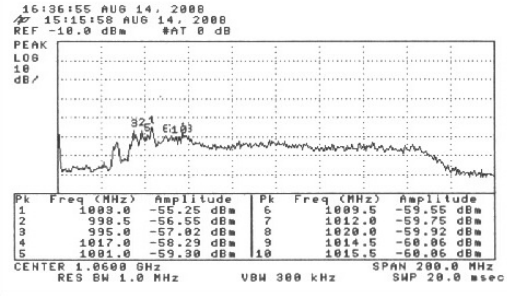

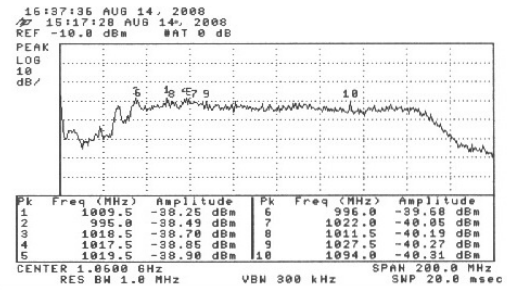

Figure 9.2.17: Channel-2 1060 MHz Front End **Figure 9.2.18: Channel-2 1060 MHz OTx**

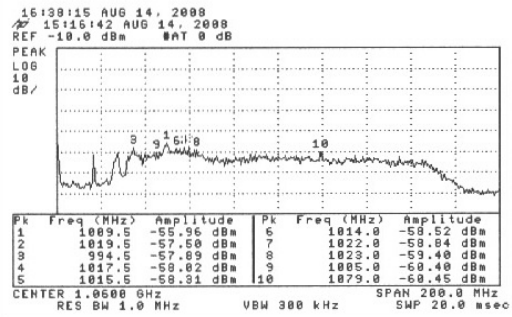

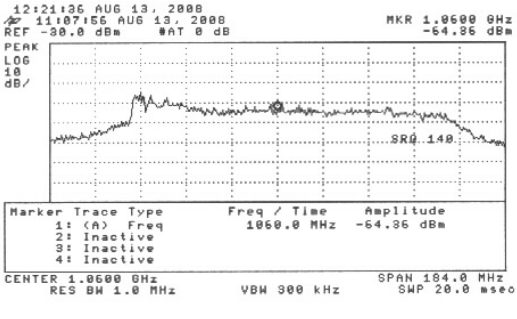

Figure 9.2.19: Channel-2 1060 MHz IF **Figure 9.2.20: Channel-2 1060 MHz ORx**

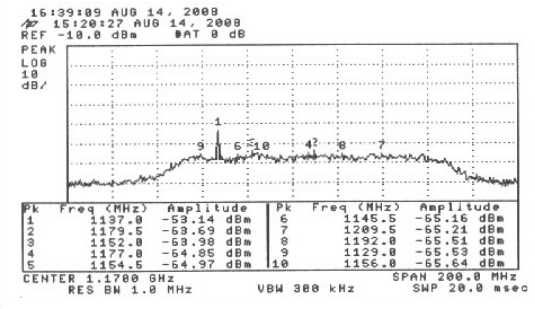

Figure 9.2.21: Channel-2 1170 MHz Front End

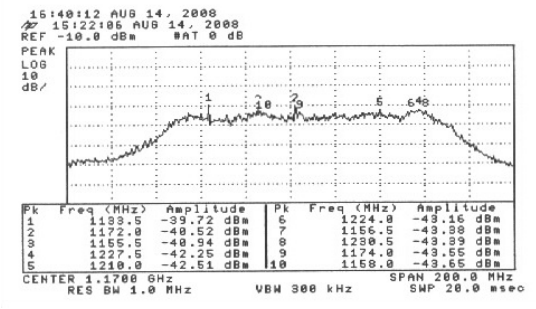

Figure 9.2.21: Channel-2 1170 MHz OTx

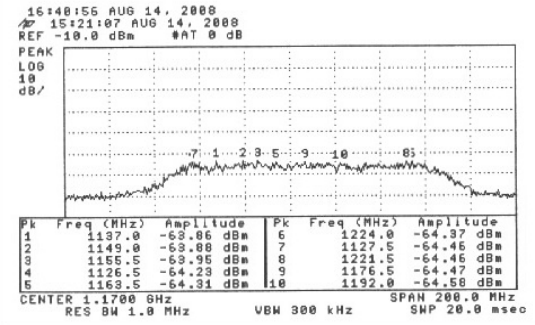

Figure 9.2.23: Channel-2 1170 MHz IF

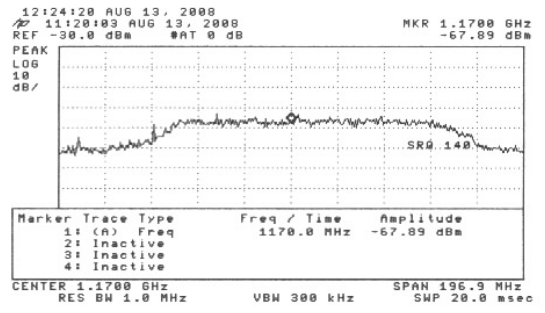

Figure 9.2.24: Channel-2 1170 MHz ORx

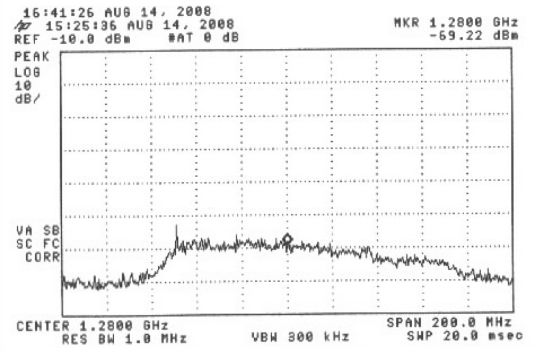

Figure 9.2.25: Channel-2 1280 MHz Front End

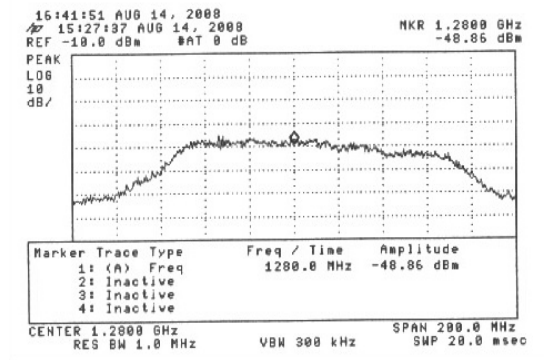

Figure 9.2.26: Channel-2 1280 MHz OTx

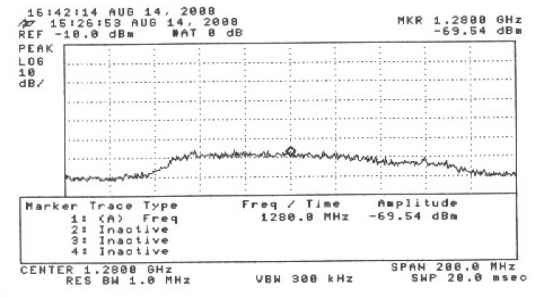

Figure 9.2.27: Channel-2 1280 MHz IF

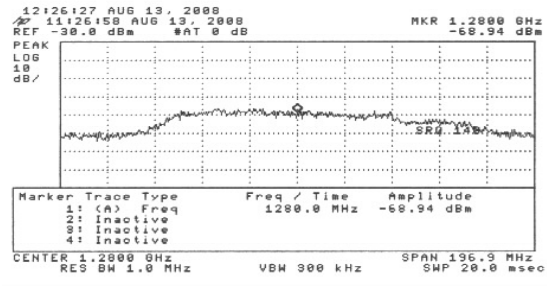

Figure 9.2.28: Channel-2 1280 MHz ORx

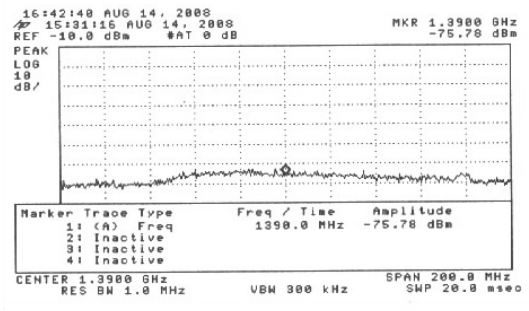

Figure 9.2.29: Channel-2 1390 MHz Front End

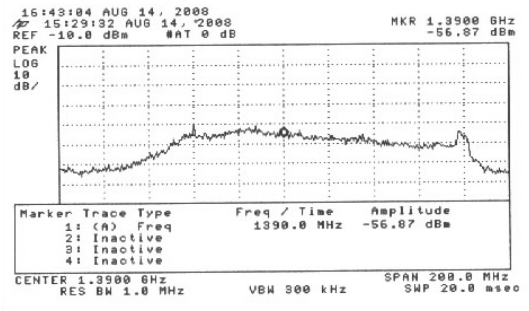

Figure 9.2.30: Channel-2 1390 MHz OTx

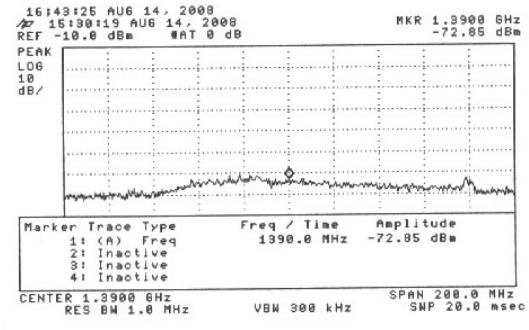

Figure 9.2.31: Channel-2 1390 MHz IF

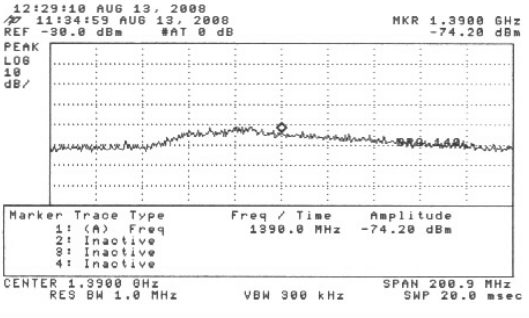

Figure 9.2.32: Channel-2 1390 MHz ORx

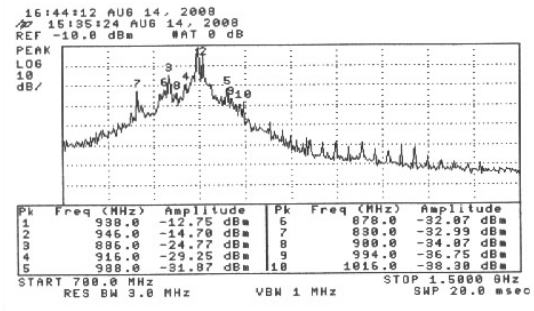

Figure 9.2.33: Channel-2 1420 MHz Front End

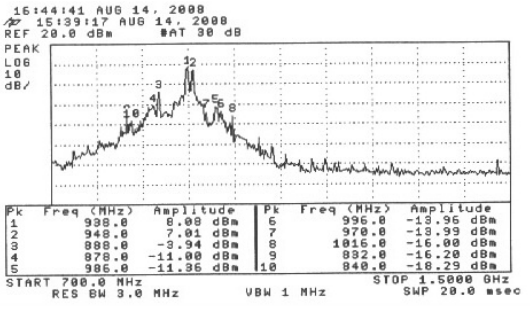

Figure 9.2.34: Channel-2 1420 MHz OTx

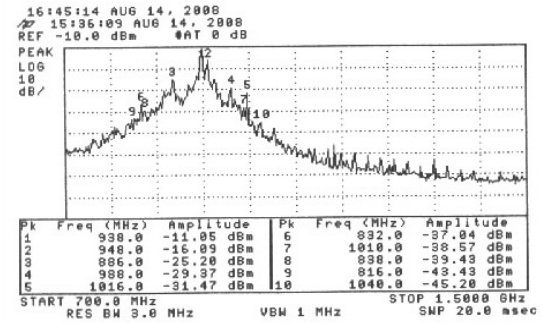

Figure 9.2.35: Channel-2 1420 MHz IF

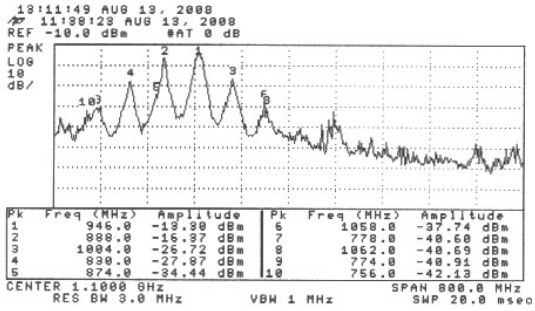

Figure 9.2.36: Channel-2 1420 MHz ORx

The spectrums of front end and the receiver system (ORx) have been taken for W-4 antenna. The corresponding power levels at the front end and receiver end are noted and tabulated in table 9.3 and the spectrums are shown in figure 9.3. The measurements of power have been done for all GMRT bands.

Table 9.3

(W-4 Antenna)

Operating Frequency	Power in Channel 1 (dBm)		Power in Channel 2 (dBm)	
(MHz)	Front End	ORx Output	Front End	ORx Output
150	-52	-37	-52	-35
233	-52	-40	-53	-37
327	-62	-50	-63	-46
610	-65	-52	-68	-50
1060	-62	-50	-65	-50
1170	-63	-51	-68	-48
1280	-69	-55	-71	-55
1390	-72	-62	-74	-60

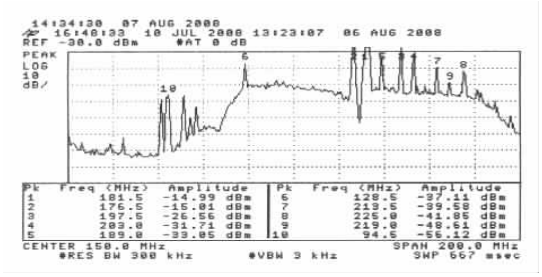

Figure 9.3.1: Channel-1 150 MHz Front End

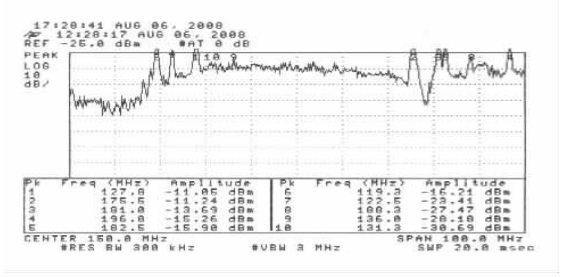

Figure 9.3.2: Channel-1 150 MHz ORx

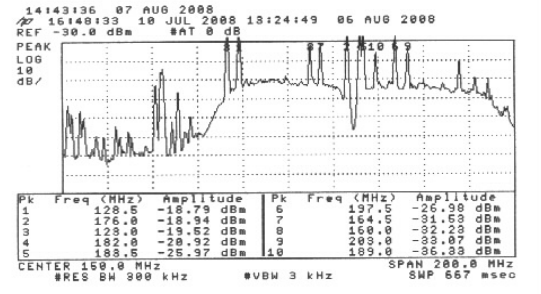

Figure 9.3.3: Channel-2 150 MHz Front End

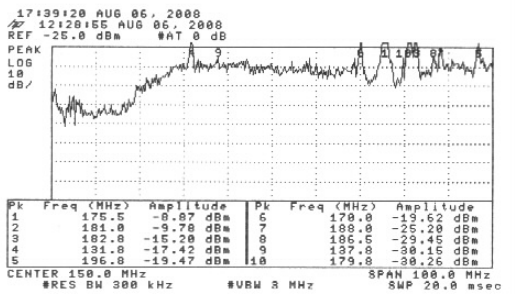

Figure 9.3.4: Channel-2 150 MHz ORx

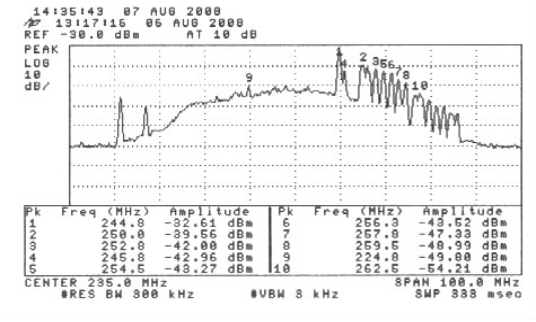

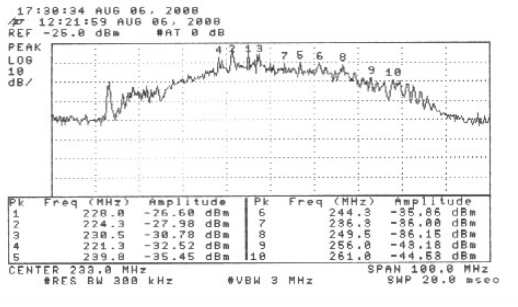

Figure 9.3.5: **Channel-1 233 MHz Front End** **Figure 9.3.6:** **Channel-1 233 MHz ORx**

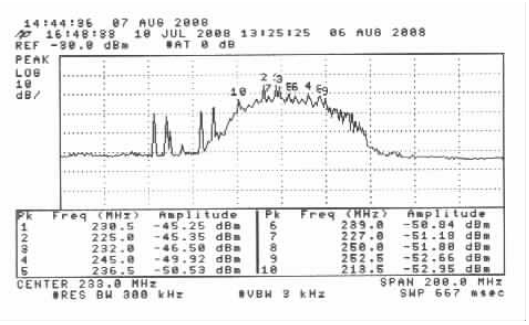

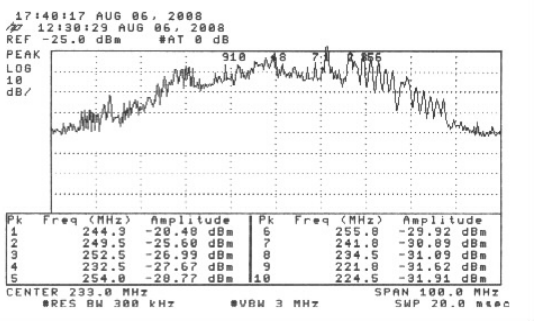

Figure 9.3.7: **Channel-2 233 MHz Front End** **Figure 9.3.8:** **Channel-2 233 MHz ORx**

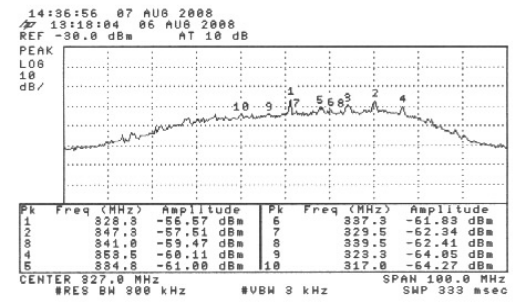

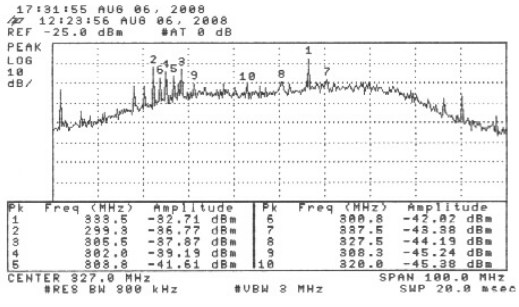

Figure 9.3.9: **Channel-1 327 MHz Front End** **Figure 9.3.10:** **Channel-1 327 MHz ORx**

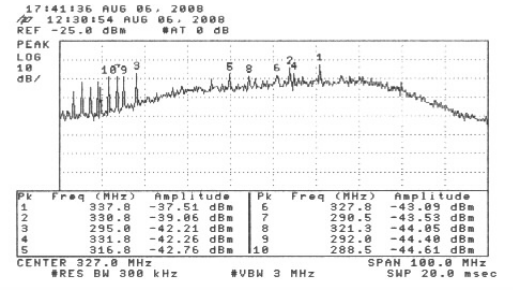

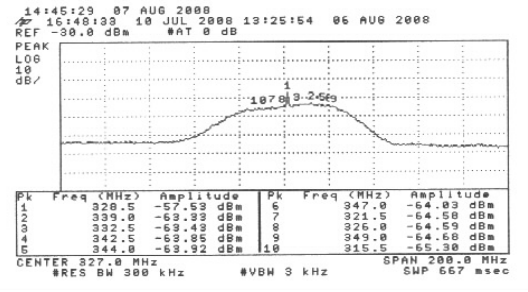

Figure 9.3.11: **Channel-2 327 MHz Front End** **Figure 9.3.12:** **Channel-2 327 MHz ORx**

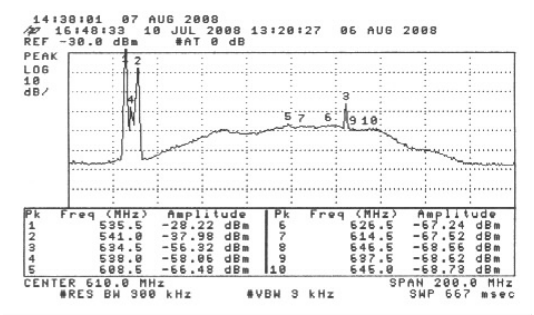

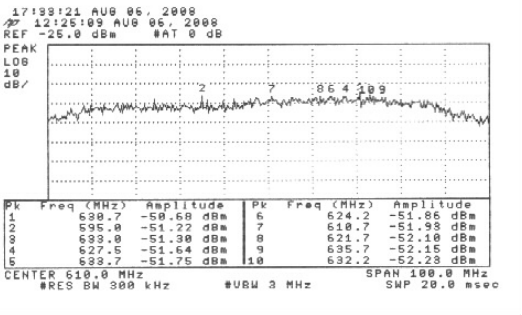

Figure 9.3.13: Channel-1 610 MHz Front End **Figure 9.3.14:** Channel-1 610 MHz ORx

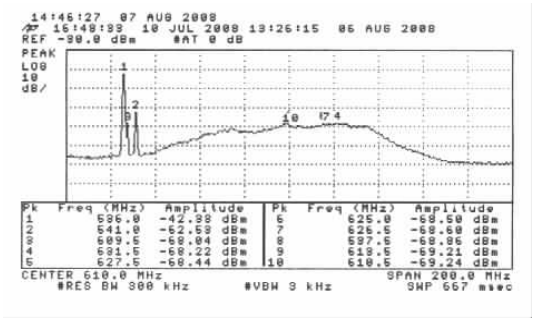

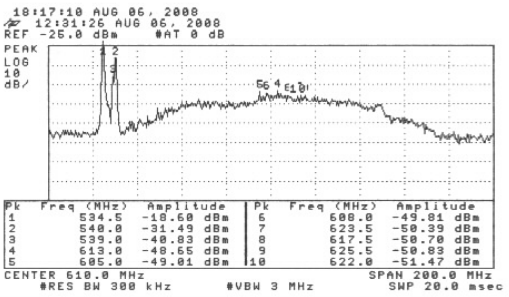

Figure 9.3.15: Channel-2 610 MHz Front End **Figure 9.3.16:** Channel-2 610 MHz ORx

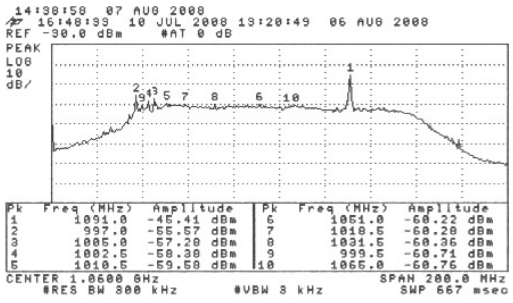

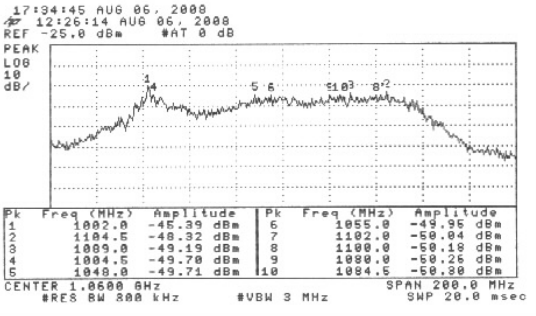

Figure 9.3.17: Channel-1 1060 MHz Front End **Figure 9.3.18:** Channel-1 1060 MHz ORx

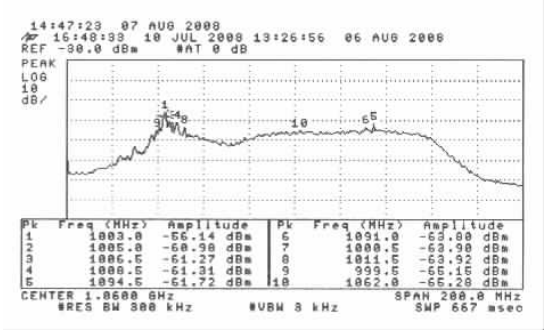

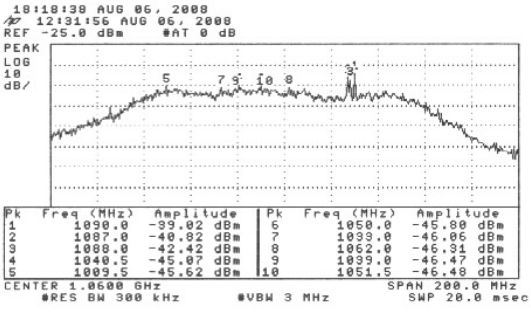

Figure 9.3.19: Channel-2 1060 MHz Front End **Figure 9.3.20:** Channel-2 1060 MHz ORx

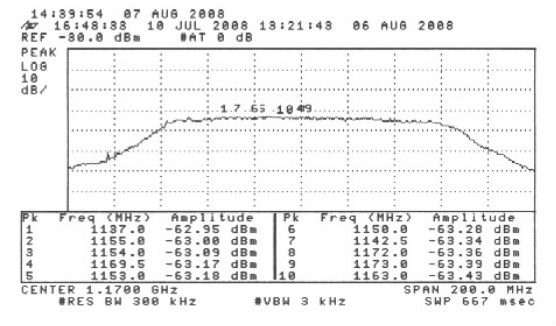

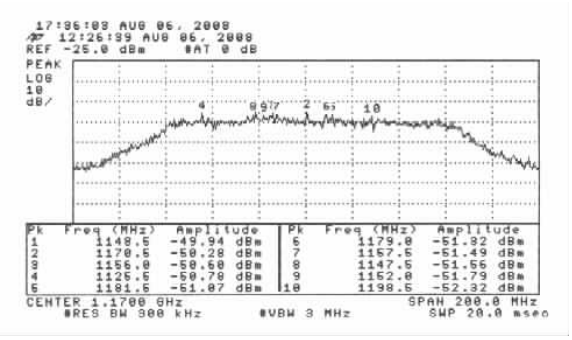

Figure 9.3.21: Channel-1 1170 MHz Front End **Figure 9.3.22: Channel-1 1170 MHz ORx**

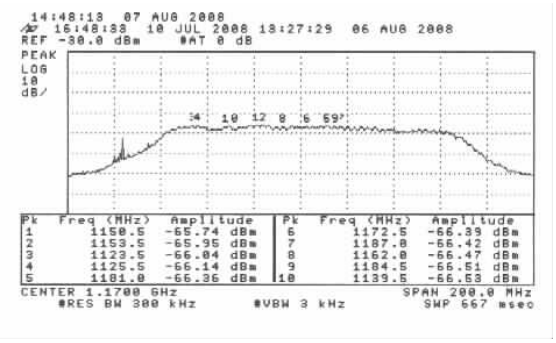

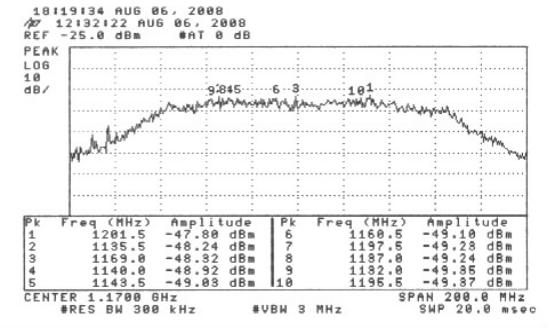

Figure 9.3.23: Channel-2 1170 MHz Front End **Figure 9.3.24: Channel-2 1170 MHz ORx**

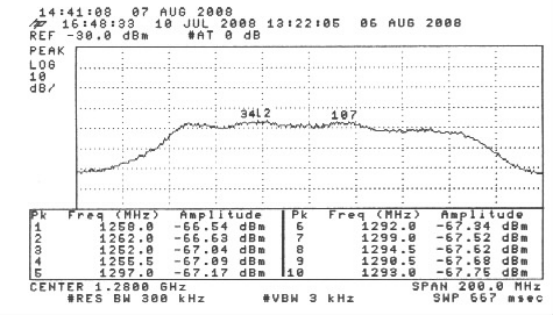

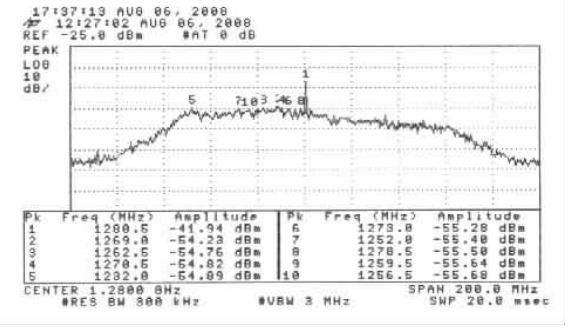

Figure 9.3.25: Channel-1 1280 MHz Front End **Figure 9.3.26: Channel-1 1280 MHz ORx**

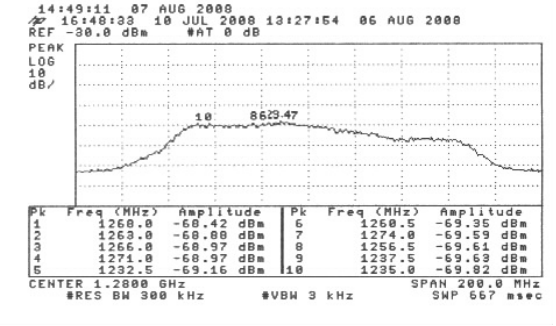

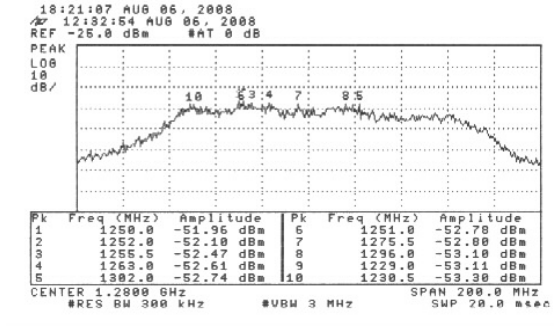

Figure 9.3.27: Channel-2 1280 MHz Front End **Figure 9.3.28: Channel-2 1280 MHz ORx**

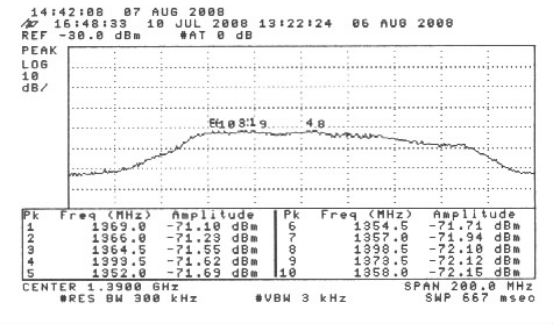

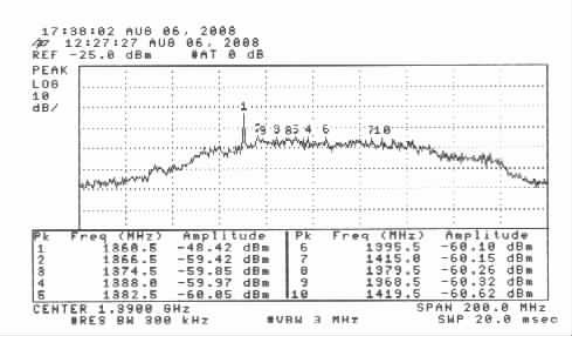

Figure 9.3.29: Channel-1 1390 MHz Front End **Figure 9.3.30:** Channel-1 1390 MHz ORx

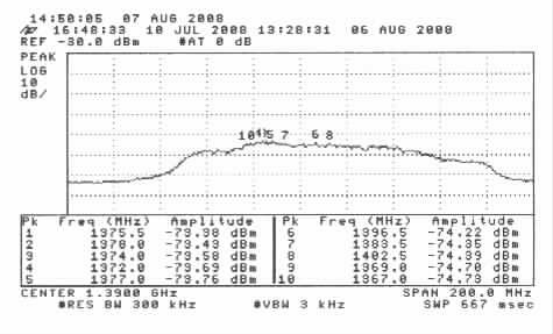

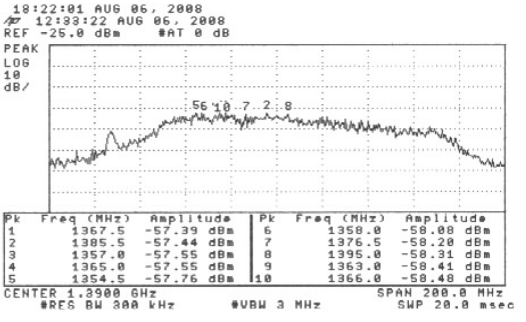

Figure 9.3.31: Channel-2 1390 MHz Front End **Figure 9.3.32:** Channel-2 1390 MHz ORx

The signal-to-noise ratio (SNR) is measured for the RF signals fed into these three antennas. To measure the signal-to-noise ratio, the RF signal of amplitude 0 dBm is fed into the input of the amplifier MSA. The signal suffers gain and losses at successive stages and thereafter, the signal is received at the receiver room, the power of which is measured with respect to a noise floor level. Thus, the signal-to-noise ratio has been calculated. This process has been implemented in three antennas. But, the channel-1 of C-11 gives some erroneous result. The spectrums of the received signal at RF of frequency 500 MHz are shown in figure 9.4.

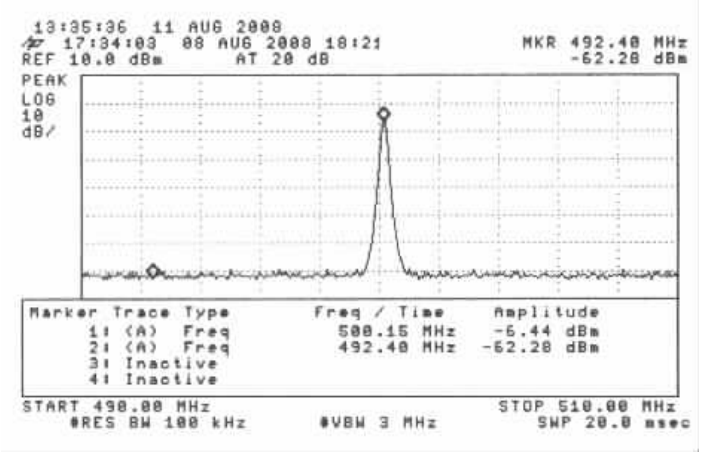

Figure 9.4.1: Channel-1 500 MHz ORx of C5

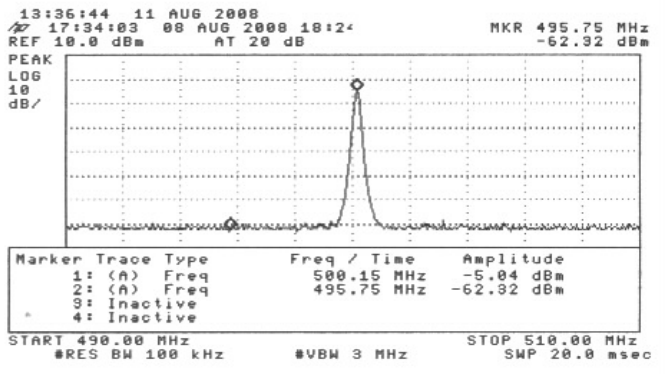

Figure 9.4.2: Channel-2 500 MHz ORx of C5

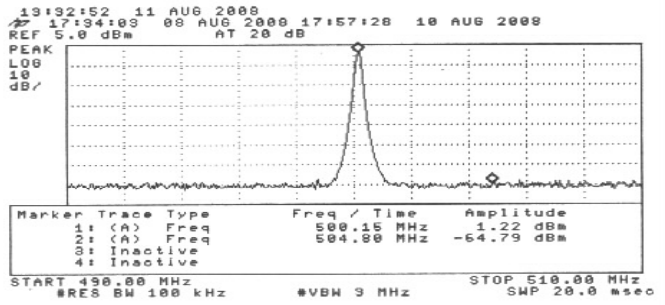

Figure 9.4.3: Channel-2 500 MHz ORx of C11

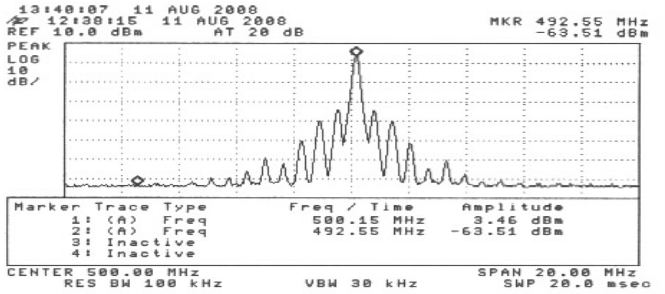

Figure 9.4.4: Channel-1 500 MHz ORx of W4

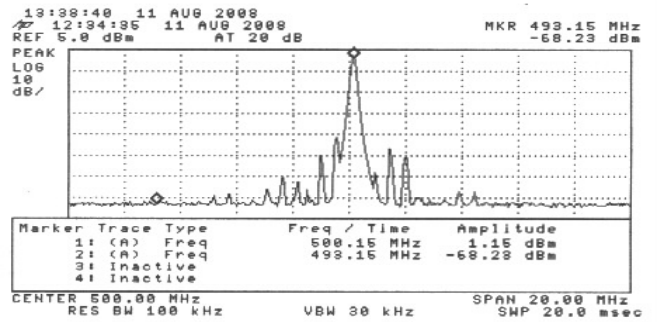

Figure 9.4.5: Channel-2 500 MHz ORx of W4

The SNR measured at the receiver room for the three antennas are calculated from the plots of figure 9.4 and the net SNR has been calculated per unit bandwidth and then compared with the theoretical value of SNR per unit bandwidth obtained in figure 6.1(e). The budget of the SNR measurement details are shown in table 9.4.

Table 9.4

(Budget for SNR)

Parameters in Concern	Antenna				
	C-5		C-11	W-4	
	Channel-1	Channel-2	Channel-2	Channel-1	Channel-2
Signal Power (dBm)	-6.44	-5.04	1.22	2.3	-1.7
Noise Power (dBm)	-62.28	-62.32	-64.79	-63.51	-68.28
Signal-To-Noise Ratio (dB)	55.84	57.28	66.01	65.81	
Attenuation	20	20	20	20	20
Optical Attenuator (dB) (if any)	-	-	4	-	-
RF Attenuation (dB)	-	-	8	-	-
Optical Connector Loss (dB)	0.5	0.5	0.5	0.5	0.5
RF Loss (dB)	1	1	1	1	1
Distance (km)	0.969	0.969	1.219	11.425	11.425
Optical Loss (dB)	0.24	0.24	0.31	2.86	2.86
RF Loss (dB)	0.48	0.48	0.62	5.71	5.71
Resolution Bandwidth (KHz)	100	100	100	100	100
Total SNR (dB/Hz)	127.32	128.76	145.63	142.52	143.29
Theoretical SNR (dB/Hz) (vide figure 6.1(e))	134.0*	134.0*	141.0	140.5	140.5

*In C-5 Antenna, GALI52 amplifier is used whose typical gain is 15 dB. So, SNR is less.

The power levels at different stages of the DWDM-based broadband link and WDM bidirectional link as shown in figure 5.8 and figure 5.9 are measured and tabulated in table 9.5.

Table 9.5

(Optical Power Budget)

Power measured at		Antenna		
		C-5 (dBm)	C-11 (dBm)	W-4 (dBm)
Antenna Base	Optical Transmitter 1 (OTx 1) Output	+6.8	+6.5	+5.7
	Optical Transmitter 2 (OTx 2) Output	+6.9	+8.2	+7.8
	DWDM MUX Output	+9.1	+9.4	+8.3
Receiver Room	DWDM DEMUX Input	+8.4	+7.2	+1.2
	Optical Receiver 1 (ORx 1) Input Optical	-2.6	+2.3	-2.8
	Receiver 2 (ORx 2) Input	-2.4	+4.1	-1.8
Antenna Base	1310 nm Input	-6.7	-0.2	-3.3
	1550 nm Output	+2.5	+4.1	-3.1
	Common Output	+4.0	+4.1	-2.9
Receiver Room	Common Output	+3.5	-3.6	+5.2
	1310 nm Output	-8.0	-1.9	-10.0
	1550 nm Input	+5.4	+5.0	+5.5

The received signal at the ABR of W-4 is measured for the forward link of the bidirectional WDM coupler making the 1550 nm signal out at the antenna base, as shown in figure 5.9. Different signals (Telemetry, Local Oscillator, and Reference Signal for Amplitude Modulation) are measured with their corresponding power along with noise floor level for the forward link. Similarly, for the return link, the telemetry signals and local oscillator signals are measured with respect to the noise floor level both at the ABR and at the receiver room at CEB. The different power levels are tabulated in the table 9.6. The Noise Floor for the Forward Link and the Return Link is at -65 dBm and -78 dBm respectively.

Table 9.6

(RF Power Budget for the Fiber-Optic Link at W-4)

Link Concerned	Measurement done at	Frequency (MHz)	Description	RF Power Level (dBm)
Forward Link	Antenna Base	17	Telemetry	-12
		19	Telemetry	-14
		97.5	Carrier for AM	-19
		106	Local Oscillator	-11
		201	Local Oscillator	-13
Return Link	Antenna Base	204.5	Telemetry	-19
		206.5	Telemetry	-19
		200	Local Oscillator	-25
		105	Local Oscillator	-25
Forward Link	Receiver Room	204.5	Telemetry	-33
		206.5	Telemetry	-35
		200	Local Oscillator	-39
		105	Local Oscillator	-39

The spectrum for the local oscillators at both the antenna base (ABR) and the receiver room at CEB have taken along with the carrier signal for AM. The spectrum of the telemetry signal of the return link is also taken, which is shown in figure 9.5.

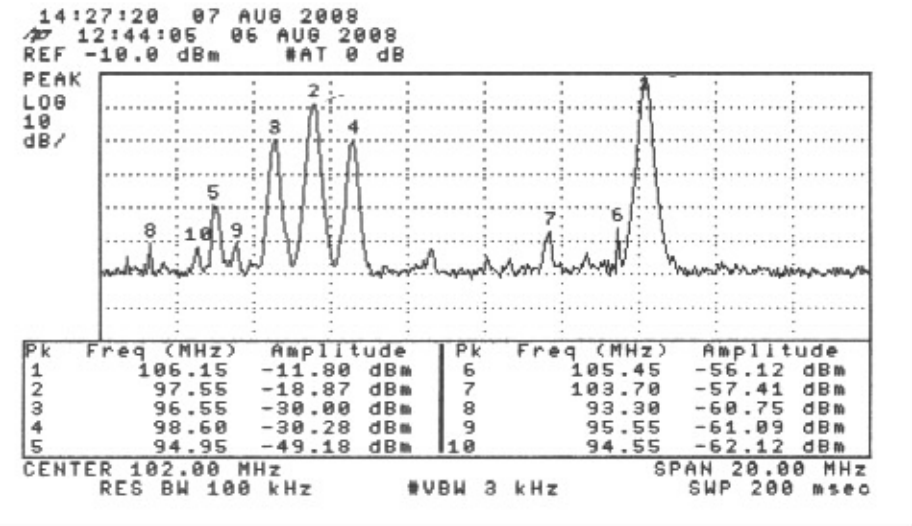

Figure 9.5.1: Spectrum of Carrier of the AM signal with two Local Oscillators In Forward Link

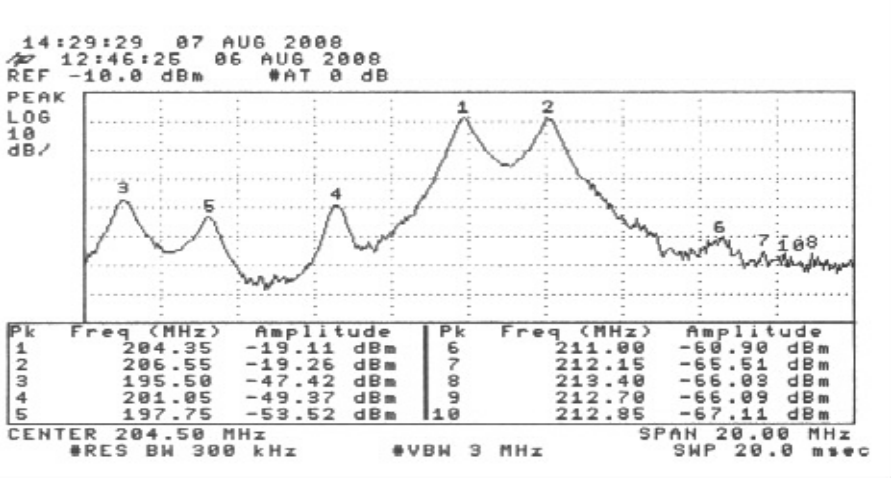

Pk	Freq (MHz)	Amplitude	Pk	Freq (MHz)	Amplitude
1	204.35	-19.11 dBm	6	211.00	-60.90 dBm
2	206.55	-19.26 dBm	7	212.15	-65.51 dBm
3	195.50	-47.42 dBm	8	213.40	-66.03 dBm
4	201.05	-49.37 dBm	9	212.70	-66.09 dBm
5	197.75	-53.52 dBm	10	212.85	-67.11 dBm

Figure 9.5.2: Spectrum of two Telemetry Signals in Return Link

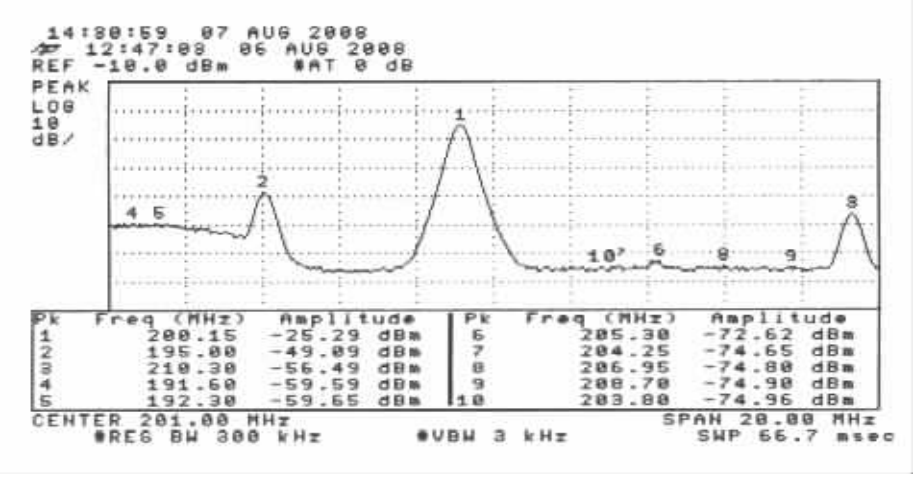

Pk	Freq (MHz)	Amplitude	Pk	Freq (MHz)	Amplitude
1	200.15	-25.29 dBm	6	205.30	-72.62 dBm
2	195.00	-49.09 dBm	7	204.25	-74.65 dBm
3	210.30	-56.49 dBm	8	206.95	-74.80 dBm
4	191.60	-59.59 dBm	9	208.70	-74.90 dBm
5	192.30	-59.65 dBm	10	203.80	-74.96 dBm

Figure 9.5.3: Spectrum of Local Oscillator Signal centred at 200 MHz in Return Link

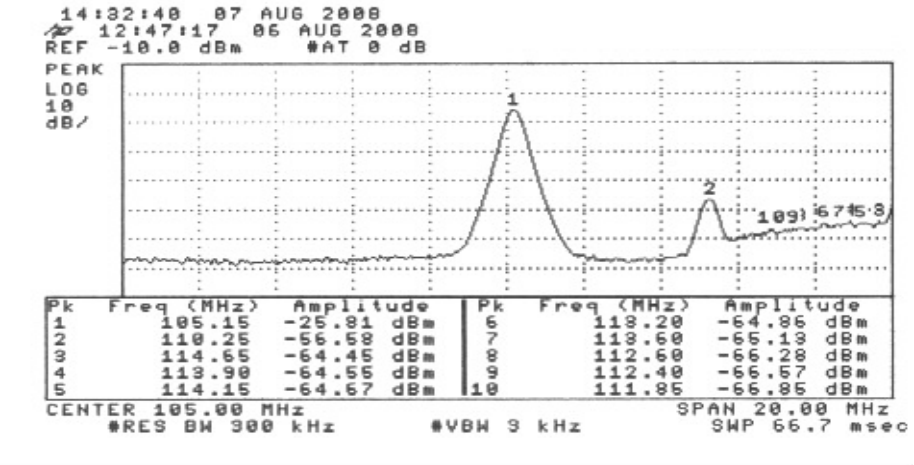

Pk	Freq (MHz)	Amplitude	Pk	Freq (MHz)	Amplitude
1	105.15	-25.81 dBm	6	118.20	-64.86 dBm
2	110.25	-56.58 dBm	7	118.60	-65.13 dBm
3	114.65	-64.45 dBm	8	112.60	-66.28 dBm
4	113.90	-64.55 dBm	9	112.40	-66.57 dBm
5	114.15	-64.67 dBm	10	111.85	-66.85 dBm

Figure 9.5.4: Spectrum of Local Oscillator Signal centred at 105 MHz in Return Link

Chapter 10

Conclusion and Future Scope of the Project

10.1. Conclusion:

The DFB-Uncooled laser has been tested and characterized by its stability in optical power and bias and its RF part. Here, the DWDM system has been developed by utilizing the advantages of taking the whole RF over the fibre-optic link.

- As per as the bias and optical power stability is concerned, it has been done by both LabView and environmental test chamber. From figure 7.5 and figure 7.6, it can be concluded that the system behaves expectedly between the temperature range of 15^{o}C and 25^{o}C for both the transmitters. However, it is also found that the second transmitter is more stable than the first one.
- From the RF characterization plot as shown in figure 7.8, the return loss is good (<-10 dB) below 450 MHz for having a VSWR within its accepted value. VSWR has a minimum value of 1. But, VSWR upto 1.5 is accepted for a practical system.
- Good return loss can be verified from the plot of impedance matching in Smith Chart as shown in figure 7.9. Here, it is shown that the system has better impedance matching at a frequency of 70 MHz compared to 450 MHz and 834.347 MHz. At 70 MHz, the impedance is nearly 51 ohms, which is within 2% of deviation of line impedance of 50 ohms. So, the return loss is the best for the overall frequency response.
- By using this new technology, it is found that there will be more Spurious-Free Dynamic Range (SFDR). Thus, one can go for higher input power so that no saturation occurs. The DFB-Uncooled laser which is tested has more 1-dB Compression Point, Third-order Intercept Point, and hence more SFDR.
- Also, the analog fibre-optic link is used instead of the digital fibre-optic link to take care of its advantages as mentioned in sections 4.4 and 4.5.
- The direct modulation is done rather than the external modulation as mentioned in the section 3.5.
- Determination of the 1-dB Compression Point, Third-order Intercept point, and the Signal-to-Noise ratio has been performed experimentally. From the experimental results, it is clear that the theoretical and experimental plot of signal-to-noise ratio for different input optical powers in the optical fibre connecting the transmitter and receiver are in good matching and differ by 1 dB. This has been taken care of some system losses, which have not been taken care of.
- From the noise performances of the link using the DFB-Uncooled laser and the MQW-DFB laser, it has been found that the Signal-To-Noise ratio is better in both DFB-Uncooled laser and MQW-DFB laser for the DWDM-based system. The SNR is nearly 20 dB more compared to existing link of GMRT. Also, the Noise Figure is less in both the links which is practically determined by the first stage of the link i.e., the noise figure of MSA0520. The comparisons with existing GMRT link are shown in figure 6.2 and figure 6.4 respectively.
- The DWDM-based link has a provision to support the existing GMRT link by using the WDM coupler, which is a bi-directional link as shown in figure 5.8.
- The SNR measured in C-5, C-11 and W-4 is compared with than the theoretical plot mentioning the different values of SNR for different optical losses. The difference of the two values of SNR is within 2 dB, which is accepted. However, it cannot be done for one of the channels of C-11 antenna as it is defective. Also, the SNR in C-5 is somewhat less

than that expected in C-11 and W-4 due to the fact that in C-5, Gali74 is used rather than Gali52 which has a gain of 7-dB lesser than that of Gali52.

- By using the DWDM-based system, the broadband nature of the link can be realized. This makes the system to work with more bandwidth. Also, since one of the fibres is now used, the second fibre can be used for some different purpose. In the upgraded DWDM-based broadband link, signals with both polarizations are coupled via the DWDM MUX and allowed to travel along the optical fibre cable to the CEB, where it is demultiplexed via the DWDM DEMUX.

10.2. Future scope of the Work:

The DWDM-based fibre-optic link along with its provision to support the existing broadband link has been established in three antennas only. These are C-5, C-11 and W-4. It should be installed in other antenna bases. Thereafter, some radio-astronomical observation can be carried out to study any phenomenon. Since the obtained SNR is more compared to the existing GMRT link, it can be helpful for observations of extraterrestrial objects. One of the channels of the fibre-optic link which is not performing expectedly should be studied thoroughly. The measurement of 1-dB Compression point, third-order intercept point and the SFDR can be performed for the MQW-DFB laser to have its complete superiority over the existing GMRT link. Once, the links are established in all antennas, this can be used replacing the existing GMRT link.

Appendix A

MATLAB Programs to study the performance using MQW-DFB Laser and DFB-Uncooled Laser

A.1. Program to study the system performance of the MQW-DFB Laser and its Comparison with existing GMRT link:

```
L=linspace(0,25,26);  %Constructing a 25-km long Fiber
a=0.25.*L;          % Calculating optical loss in dB
alphaDWDM=0.5+a;        % Calculating total loss in dB

I_ThDWDM=(20)*(10^(-3));
I_OpDWDM=(63)*(10^(-3));
P_ThDWDM=(0.1)*(10^(-3));
P_OpDWDM=(7.4131)*(10^(-3));
etaDWDM=((P_OpDWDM-P_ThDWDM)/(I_OpDWDM-I_ThDWDM));
RDWDM=0.8;
R_L=50;
lossDWDM=10.^(-alphaDWDM./10);
RIN=-140;
I_PhDWDM=((I_OpDWDM-I_ThDWDM)*etaDWDM*RDWDM).*lossDWDM;
ADWDM=((I_PhDWDM./2).^2)*R_L;
BDWDM=10.*log10(ADWDM);
P_laserDWDM=RIN+BDWDM+30;

e=1.6*(10^(-19));
I_dDWDM=10*(10^(-9));
P_shotDWDM=(10.*log10((e*R_L).*(I_PhDWDM+I_dDWDM)))+30;

NFDWDM=10^(0.3);
k=(1.38)*(10^(-23));
T=290;
RL=500;
DDWDM=((4*k*T*NFDWDM)/RL);
P_ThermalDWDM=((10*log10(DDWDM))+30).*(ones(1,26));

P_LDWDM=10.^(P_laserDWDM./10);
P_SDWDM=10.^(P_shotDWDM./10);
P_TDWDM=10.^(P_ThermalDWDM./10);
P_toDWDM=P_LDWDM+P_SDWDM+P_TDWDM;
P_TotalDWDM=10.*log10(P_toDWDM);

GDWDM=((((etaDWDM*RDWDM).*(lossDWDM))./2).^2);
G_linkDWDM=(10.*log10(GDWDM))+20;
GlinkDWDM=10.^(G_linkDWDM./10);

EIN_linkDWDM=P_TotalDWDM-G_linkDWDM;  % Calculating Effective Input Noise

NF_linkDWDM=EIN_linkDWDM+174;     % Calculating Noise Figure
NFlinkDWDM=10.^(NF_linkDWDM./10);  % Noise Figure of link in numerics

F1=10^(0.65);
G1=10^(0.85);
L1=10^(0.3);
```

```
T_phys=298;
F2=1+(((L1-1)*T_phys)/T);
G2=10^(-0.3);
F3=10^(0.27);
G3=10^(2.18);
G4=(G1*G2*G3).*(GlinkDWDM);
NF_ConstDWDM=F1+((F2-1)/G1)+((F3-1)/(G1*G2));
NFtotalDWDM=NF_ConstDWDM+((NFlinkDWDM-1)/(G1*G2*G3));
NF_totalDWDM=10.*log10(NFtotalDWDM);

F4=10^(0.3);
NFPostDWDM=NFlinkDWDM+((F4-1)./(GlinkDWDM));
NF_PostDWDM=10.*log10(NFPostDWDM);

NFNetDWDM=NFtotalDWDM+((F4-1)./(G4));
NF_NetDWDM=10.*log10(NFNetDWDM);

SNR_ThermalDWDM= G_linkDWDM-P_ThermalDWDM; % Calculating Thermal-noise limited SNR in dB
SNR_laserDWDM= G_linkDWDM-P_laserDWDM;     % Calculating Laser-noise limited SNR in dB
SNR_shotDWDM= G_linkDWDM-P_shotDWDM;       % Calculating Shot-noise limited SNR in dB
SNR_TotalDWDM= G_linkDWDM-P_TotalDWDM;     % Calculating Total-noise limited SNR in dB

figure(1);

plot(alphaDWDM,G_linkDWDM);
xlabel('Optical Loss (dB) -->');
ylabel('Conversion Loss (dB)');
title('Variation of Conversion Loss with Link Distance For the DWDM DFB Transmitter and Discovery
Semiconductor Receiver');
grid on;

figure(2);

plot(alphaDWDM,P_laserDWDM,'b',alphaDWDM,P_shotDWDM,'r',alphaDWDM,P_ThermalDWDM,'y',alpha
DWDM,P_TotalDWDM,'k');
xlabel('Optical Loss (dB) -->');
ylabel('Noise Power (dB/Hz) -->');
title('Variation of Noise Power with Link Distance For the DWDM DFB Transmitter and Discovery
Semiconductor Receiver');
legend('RIN Noise','Shot Noise','Thermal Noise','Total Noise',-1);
grid on;

figure(3);

plot(alphaDWDM,EIN_linkDWDM);
xlabel('Optical Loss (dB) -->');
ylabel('EIN (dB/Hz) -->');
title('Variation of Equivalent Input Noise with Link Distance For the DWDM DFB Transmitter and Discovery
Semiconductor Receiver');
grid on;
```

```
figure(4);

plot(alphaDWDM,NF_linkDWDM,'b',alphaDWDM,NF_totalDWDM,'c',alphaDWDM,NF_PostDWDM,'r',alphaD
WDM,NF_NetDWDM,'k');
xlabel('Optical Loss (dB) -->');
ylabel('Noise Figure (dB) -->');
title('Variation of Noise Figure with Link Distance For the DWDM DFB Transmitter and Discovery
Semiconductor Receiver');
legend('Noise Figure without Pre-Amplifier','Noise Figure with Pre-Amplifiers','Noise Figure with Post-
Amplifiers','Noise Figure of the Total Link', -1);
grid on;

figure(5);

plot(alphaDWDM,SNR_ThermalDWDM,'y',alphaDWDM,SNR_laserDWDM,'b',alphaDWDM,SNR_shotDWD
M,'r',alphaDWDM,SNR_TotalDWDM,'k');
xlabel('Optical Loss (dB) -->');
ylabel('SNR (dB/Hz) -->');
title('Variation of Signal to Noise Ratio with Link Distance For the DWDM DFB Transmitter and Discovery
Semiconductor Receiver');
legend('Thermal Noise limited SNR','Laser Noise Limited SNR','Shot Noise Limited SNR','Total SNR',-1);
grid on;

lossGMRT=0.3:0.1:8.7;
alphaGMRT=10.^(-lossGMRT./10);
I_biasGMRT=(51)*(10^(-3));
I_ThGMRT=(28)*(10^(-3));
etaGMRT=0.047;
RGMRT=0.8;
I_PhGMRT=((I_biasGMRT-I_ThGMRT)*etaGMRT*RGMRT).*(alphaGMRT);
AGMRT=((I_PhGMRT./2).^2).*(50);
BGMRT=10.*log10(AGMRT);
CGMRT=BGMRT+30;
P_laserGMRT=-137+CGMRT;       % Calculating Laser Noise

e=1.6*(10^(-19));
I_dGMRT=5*(10^(-9));
DGMRT=(e*50).*(I_PhGMRT+I_dGMRT);
P_shotGMRT=10.*log10(DGMRT)+30;

k=1.38*(10^(-23));
T=290;
P_Th=k*T;
P_ThermalGMRT=((10.*log10(P_Th))+30).*(ones(1,85));  % Calculating Thermal Noise

P_lGMRT=10.^(P_laserGMRT./10);
P_sGMRT=10.^(P_shotGMRT./10);
P_TGMRT=10.^(P_ThermalGMRT/10);
P_toGMRT=P_lGMRT+P_sGMRT+P_TGMRT;
P_totalGMRT=10.*log10(P_toGMRT);  % Calculating Total Noise
```

```
GGMRT=((etaGMRT*(RGMRT/2)).*(alphaGMRT)).^2;
G_linkGMRT=10.*log10(GGMRT);

EIN_linkGMRT=P_totalGMRT-G_linkGMRT;  % Calculating Effective Input Noise
NF_linkGMRT=EIN_linkGMRT+174;     % Calculating Noise Figure
NFlinkGMRT=10.^(NF_linkGMRT./10);
FGMRT=10.^(0.2);
NF_ampGMRT=NFlinkGMRT+((FGMRT-1)./GGMRT);
NF_PostGMRT=10.*log10(NF_ampGMRT);

SNR_totalGMRT= G_linkGMRT-P_totalGMRT; % Calculating Total SNR in dB
SNR_laserGMRT= G_linkGMRT-P_laserGMRT; % Calculating Laser-noise limited SNR in dB
SNR_shotGMRT= G_linkGMRT-P_shotGMRT;   % Calculating Shot-noise limited SNR in dB
SNR_ThermalGMRT= G_linkGMRT-P_ThermalGMRT; % Calculating Thermal-noise limited SNR in dB

figure(6);

plot(lossGMRT,G_linkGMRT);
xlabel('Optical Loss (dB) -->');
ylabel('Gain (dB)');
title('Variation of Gain with Optical Loss For the existing GMRT Fiber Optic Link');
grid on;

figure(7);

plot(lossGMRT,P_laserGMRT,'b',lossGMRT,P_shotGMRT,'r',lossGMRT,P_ThermalGMRT,'c',lossGMRT,P_t
otalGMRT,'k');
xlabel('Optical Loss (dB) -->');
ylabel('Noise Power (dBm) -->');
legend('RIN Noise Power','Shot Noise Power','Thermal Noise Power','Total Noise Power',-1);
title('Variation of Noise Power with Optical Loss for the existing GMRT Fiber Optic Link');
grid on;

figure(8);

plot(lossGMRT,EIN_linkGMRT);
xlabel('Optical Loss (dB) -->');
ylabel('EIN (dBm/Hz) -->');
title('Variation of Equivalent Input Noise with Optical Loss for the existing GMRT Fiber Optic Link');
grid on;

figure(9);

plot(lossGMRT,NF_linkGMRT,'b',lossGMRT,NF_PostGMRT,'k');
xlabel('Optical Loss (dB) -->');
ylabel('Noise Figure (dB) -->');
title('Variation of Noise Figure with Optical Loss for the existing GMRT Fiber Optic Link');
legend('Noise Figure without Post-Amplifier','Noise Figure with Post-Amplifiers', -1);
grid on;
```

```
figure(10);

plot(lossGMRT,SNR_laserGMRT,'b',lossGMRT,SNR_shotGMRT,'r',lossGMRT,SNR_ThermalGMRT,'c',loss
GMRT,SNR_totalGMRT,'k');
xlabel('Optical Loss (dB) -->');
ylabel('SNR (dB/Hz) -->');
title('Variation of Signal to Noise Ratio with Optical Loss for the existing GMRT Fiber Optic Link');
legend('Laser Noise Limited SNR','Shot Noise Limited SNR','Thermal Noise Limited SNR','Total SNR',-1);
grid on;

figure(11);

plot(alphaDWDM,G_linkDWDM,'b',lossGMRT,G_linkGMRT,'k');
xlabel('Optical Loss (dB) -->');
ylabel('Conversion Loss (dB) -->');
title('Variation of Conversion Loss with Optical Loss');
legend('DWDM-Based Broadband Link','GMRT link', -1);
grid on;

figure(12);

plot(alphaDWDM,P_TotalDWDM,'b',lossGMRT,P_totalGMRT,'k');
xlabel('Optical Loss (dB) -->');
ylabel('Noise Power (dBm/Hz) -->');
title('Variation of Noise Power with Optical Loss');
legend('DWDM-Based Broadband Link','GMRT link', -1);
grid on;

figure(13);

plot(alphaDWDM,EIN_linkDWDM,'b',lossGMRT,EIN_linkGMRT,'k');
xlabel('Optical Loss (dB) -->');
ylabel('Effective Input Noise (dBm/Hz) -->');
title('Variation of EIN with Optical Loss');
legend('DWDM-Based Broadband Link','GMRT link', -1);
grid on;

figure(14);

plot(alphaDWDM,NF_linkDWDM,'b',lossGMRT,NF_linkGMRT,'k');
xlabel('Optical Loss (dB) -->');
ylabel('Noise Figure (dB) -->');
title('Variation of Noise Figure with Optical Loss');
legend('DWDM-Based Broadband Link','GMRT link', -1);
grid on;
```

```
figure(15);

plot(alphaDWDM,NF_NetDWDM,'b',lossGMRT,NF_PostGMRT,'k');
xlabel('Optical Loss (dB) -->');
ylabel('Noise Figure (dB) -->');
title('Variation of Noise Figure with Optical Loss');
legend('DWDM-Based Broadband Link','GMRT link', -1);
grid on;

figure(16);

plot(alphaDWDM,SNR_TotalDWDM,'b',lossGMRT,SNR_totalGMRT,'k');
xlabel('Optical Loss (dB) -->');
ylabel('SNR (dB/Hz) -->');
title('Variation of SNR with Optical Loss');
legend('DWDM-Based Broadband Link','GMRT link');
grid on;

figure(17);

subplot(1,2,1);
plot(alphaDWDM,G_linkDWDM,'b',lossGMRT,G_linkGMRT,'k');
xlabel('Optical Loss (dB) -->');
ylabel('Conversion Loss (dB) -->');
title('Conversion Loss');
legend('DWDM-Based Broadband Link','GMRT link');
grid on;

subplot(1,2,2);
plot(alphaDWDM,SNR_TotalDWDM,'b',lossGMRT,SNR_totalGMRT,'k');
xlabel('Optical Loss (dB) -->');
ylabel('SNR (dB/Hz) -->');
title('Variation of SNR with Optical Loss');
legend('DWDM-Based Broadband Link','GMRT link');
grid on;
```

A.2. Program to study the system performance of the DFB-Uncooled Laser:

```
close all;
clear all;
L=linspace(0,25,26);  %Constructing a 25-km long Fiber
a=0.25.*L;          % Calculating optical loss in dB
alphaDFB=4.5+a;         % Calculating total loss in dB

IDFB=7.1364*(10^(-4));
lossDFB=10.^(-alphaDFB/10);
I_PhDFB=IDFB.*lossDFB;        % Photocurrent

ADFB=((I_PhDFB./2).^2).*50;
BDFB=10.*log10(ADFB);
CDFB=BDFB+30;
P_laserDFB=-155+CDFB;       % Calculating Laser Noise

DDFB=3.2*50*(10^(-19));
P_shDFB=DDFB.*(I_PhDFB./2);
P_shotDFB=10.*log10(P_shDFB)+30; % Calculating Shot Noise

k=1.38*(10^(-23));
T=290;
P_Th=k*T;
P_Thermal=((10.*log10(P_Th))+30).*(ones(1,26));  % Calculating Thermal Noise

P_lDFB=10.^(P_laserDFB./10);
P_sDFB=10.^(P_shotDFB./10);
P_T=10.^(P_Thermal/10);

P_toDFB=P_lDFB+P_sDFB+P_T;
P_totalDFB=10.*log10(P_toDFB);  % Calculating Total Noise



FDFB=3.8*(10^(-2));
GDFB=(FDFB.*lossDFB).^2;
G_linkDFB=(10.*log10(GDFB))+20; % Calculating Link Gain

EIN_linkDFB=P_totalDFB-G_linkDFB;  % Calculating Effective Input Noise
NF_linkDFB=EIN_linkDFB+174;     % Calculating Noise Figure
F1=10^(0.65);                % Noise Figure of MSA
G1=10^(0.85);                % Gain of MSA
L1=10^(0.3);
T_phys=298;
F2=1+(((L1-1)*T_phys)/T);       % Noise Figure of Power Divider
G2=10^(-0.3);                % Gan of Power Divider
F3=10^(0.27);                % Noise Figure of Gali
G3=10^(2.18);                % Gain of Gali
NF_ConstDFB=F1+((F2-1)/G1)+((F3-1)/(G1*G2));  % Evaluating Constant part of Noise Figure
```

```
NFlinkDFB=10.^(NF_linkDFB/10);  % Noise Figure of link in numerics
NFtotalDFB=NF_ConstDFB+((NFlinkDFB-1)/(G1*G2*G3));
NF_totalDFB=10.*log10(NFtotalDFB);

SNR_totalDFB= G_linkDFB-P_totalDFB; % Calculating Total SNR in dB
SNR_laserDFB= G_linkDFB-P_laserDFB; % Calculating Laser-noise limited SNR in dB
SNR_shotDFB= G_linkDFB-P_shotDFB;   % Calculating Shot-noise limited SNR in dB
SNR_ThermalDFB= G_linkDFB-P_Thermal; % Calculating Thermal-noise limited SNR in dB
IP3DFB= 30.1;
SFDR_DFB= (2/3).*(IP3DFB+174-NF_totalDFB);



figure(1);

plot(alphaDFB,G_linkDFB);
xlabel('Optical Loss (dB) -->');
ylabel('Conversion Loss (dB) -->');
title('Variation of Conversion Loss with Optical Loss For the DFB Uncooled Fiber Optic Link');
grid on;

figure(2);

plot(alphaDFB,P_laserDFB,'b',alphaDFB,P_shotDFB,'r',alphaDFB,P_Thermal,'g',alphaDFB,P_totalDFB,'k');
xlabel('Optical Loss (dB) -->');
ylabel('Noise Power (dBm/Hz) -->');
legend('RIN Noise Power','Shot Noise Power','Thermal Noise Power','Total Noise Power',-1);
title('Variation of Noise Power with Optical Loss For the DFB Uncooled Fiber Optic Link');
grid on;

figure(3);

plot(alphaDFB,EIN_linkDFB);
xlabel('Optical Loss (dB) -->');
ylabel('EIN (dBm/Hz) -->');
title('Variation of Equivalent Input Noise with Optical Loss For the DFB Uncooled Fiber Optic Link');
grid on;

figure(4);

plot(alphaDFB,NF_linkDFB,'b',alphaDFB,NF_totalDFB,'k');
xlabel('Optical Loss (dB) -->');
ylabel('Noise Figure (dB) -->');
title('Variation of Noise Figure with Optical Loss For the DFB Uncooled Fiber Optic Link');
legend('Noise Figure without Pre-Amplifier','Noise Figure with Pre-Amplifiers', -1);
grid on;
```

```
figure(5);

plot(alphaDFB,SNR_laserDFB,'b',alphaDFB,SNR_shotDFB,'r',alphaDFB,SNR_ThermalDFB,'g',alphaDFB,S
NR_totalDFB,'k');
xlabel('Optical Loss (dB) -->');
ylabel('SNR (dB/Hz) -->');
title('Variation of Signal to Noise Ratio with Optical Loss For the DFB Uncooled Fiber Optic Link');
legend('Laser Noise Limited SNR','Shot Noise Limited SNR','Thermal Noise Limited SNR','Total SNR',-1);
grid on;

figure (6);

plot(alphaDFB,SFDR_DFB);
xlabel('Optical Loss (dB)');
ylabel('SFDR (dB/Hz)');
title('Variation of Spurious Free Dynamic Range with Optical Loss For the DFB Uncooled Fiber Optic Link');
grid on;
axis([4 11 130 132]);
```

A.3. Program to compare the system performance of the DFB-Uncooled Laser with Existing GMRT link:

```
L=linspace(0,25,26);  %Constructing a 25-km long Fiber
a=0.25.*L;          % Calculating optical loss in dB
alphaDFB=4.5+a;         % Calculating total loss in dB for DFB

IDFB=7.1364*(10^(-4));
lossDFB=10.^(-alphaDFB/10);
I_PhDFB=IDFB.*lossDFB;        % Photocurrent

ADFB=((I_PhDFB./2).^2).*50;
BDFB=10.*log10(ADFB);
CDFB=BDFB+30;
P_laserDFB=-155+CDFB;       % Calculating Laser Noise

D=3.2*50*(10^(-19));
P_shDFB=D.*(I_PhDFB./2);
P_shotDFB=10.*log10(P_shDFB)+30; % Calculating Shot Noise

k=1.38*(10^(-23));
T=290;
P_Th=k*T;
P_Thermal=((10.*log10(P_Th))+30).*(ones(1,26));  % Calculating Thermal Noise

P_lDFB=10.^(P_laserDFB/10);
P_sDFB=10.^(P_shotDFB/10);
P_T=10.^(P_Thermal/10);

P_toDFB=P_lDFB+P_sDFB+P_T;
P_totalDFB=10.*log10(P_toDFB);


FDFB=3.8*(10^(-2));
GDFB=(FDFB.*lossDFB).^2;
G_linkDFB=(10.*log10(GDFB))+20; % Calculating Link Gain

EIN_linkDFB=P_totalDFB-G_linkDFB;  % Calculating Effective Input Noise
NF_linkDFB=EIN_linkDFB+174;     % Calculating Noise Figure
F1=10^(0.65);                % Noise Figure of MSA
G1=10^(0.85);                % Gain of MSA
L1=10^(0.3);
T_phys=298;
F2=1+(((L1-1)*T_phys)/T);       % Noise Figure of Power Divider
G2=10^(-0.3);                % Gan of Power Divider
F3=10^(0.27);                % Noise Figure of Gali
G3=10^(2.18);                % Gain of Gali
NF_ConstDFB=F1+((F2-1)/G1)+((F3-1)/(G1*G2));  % Evaluating Constant part of Noise Figure
NFlinkDFB=10.^(NF_linkDFB/10);  % Noise Figure of link in numerics
NFtotalDFB=NF_ConstDFB+((NFlinkDFB-1)/(G1*G2*G3));
```

```
NF_totalDFB=10.*log10(NFtotalDFB);

SNR_totalDFB= G_linkDFB-P_totalDFB; % Calculating Total SNR in dB
SNR_laserDFB= G_linkDFB-P_laserDFB; % Calculating Laser-noise limited SNR in dB
SNR_shotDFB= G_linkDFB-P_shotDFB;   % Calculating Shot-noise limited SNR in dB
SNR_ThermalDFB= G_linkDFB-P_Thermal; % Calculating Thermal-noise limited SNR in dB

IP3_DFB= 30.1;
SFDR_DFB= (2/3).*(IP3_DFB+174-NF_totalDFB);

lossGMRT=0.3:0.1:8.7;
alphaGMRT=10.^(-lossGMRT./10);
I_biasGMRT=(51)*(10^(-3));
I_ThGMRT=(28)*(10^(-3));
etaGMRT=0.047;
RGMRT=0.8;
I_PhGMRT=((I_biasGMRT-I_ThGMRT)*etaGMRT*RGMRT).*(alphaGMRT);
AGMRT=((I_PhGMRT./2).^2).*(50);
BGMRT=10.*log10(AGMRT);
CGMRT=BGMRT+30;
P_laserGMRT=-137+CGMRT;       % Calculating Laser Noise

e=1.6*(10^(-19));
I_dGMRT=5*(10^(-9));
DGMRT=(e*50).*(I_PhGMRT+I_dGMRT);
P_shotGMRT=10.*log10(DGMRT)+30;

k=1.38*(10^(-23));
T=290;
P_Th=k*T;
P_ThermalGMRT=((10.*log10(P_Th))+30).*(ones(1,85));  % Calculating Thermal Noise

P_lGMRT=10.^(P_laserGMRT./10);
P_sGMRT=10.^(P_shotGMRT./10);
P_TGMRT=10.^(P_ThermalGMRT/10);
P_toGMRT=P_lGMRT+P_sGMRT+P_TGMRT;
P_totalGMRT=10.*log10(P_toGMRT);  % Calculating Total Noise

GGMRT=((etaGMRT*(RGMRT/2)).*(alphaGMRT)).^2;
G_linkGMRT=10.*log10(GGMRT);

EIN_linkGMRT=P_totalGMRT-G_linkGMRT;  % Calculating Effective Input Noise
NF_linkGMRT=EIN_linkGMRT+174;     % Calculating Noise Figure
NFlinkGMRT=10.^(NF_linkGMRT./10);
FGMRT=10.^(0.2);
NFampGMRT=NF_linkGMRT+((FGMRT-1)./GGMRT);
NF_ampGMRT=10.*(log10(NFampGMRT));

SNR_totalGMRT= G_linkGMRT-P_totalGMRT; % Calculating Total SNR in dB
SNR_laserGMRT= G_linkGMRT-P_laserGMRT; % Calculating Laser-noise limited SNR in dB
SNR_shotGMRT= G_linkGMRT-P_shotGMRT;   % Calculating Shot-noise limited SNR in dB
```

```
SNR_ThermalGMRT= G_linkGMRT-P_ThermalGMRT; % Calculating Thermal-noise limited SNR in dB

IP3_GMRT= 20.1;
SFDR_GMRT= (2/3).*(IP3_GMRT+174-NF_linkGMRT);


figure(1);

plot(alphaDFB,G_linkDFB,'b',lossGMRT,G_linkGMRT,'k');
xlabel('Optical Loss(dB) -->');
ylabel('Conversion Loss (dB) -->');
legend('Conversion Loss using DFB Uncooled Laser','Conversion Loss using GMRT link',-1);
title('Variation of Conversion Loss with Optical Loss');
grid on;

figure(2);

plot(alphaDFB,EIN_linkDFB,'b',lossGMRT,EIN_linkGMRT,'k');
xlabel('Optical Loss(dB) -->');
ylabel('EIN (dBm/Hz) -->');
legend('EIN using DFB Uncooled Laser','EIN using GMRT',-1);
title('Variation of Equivalent Input Noise with Optical Loss');
grid on;

figure(3);

plot(alphaDFB,NF_totalDFB,'b',lossGMRT,NF_ampGMRT,'k');
xlabel('Optical Loss(dB) -->');
ylabel('Noise Figure (dB) -->');
legend('Noise Figure using DFB Uncooled Laser with amplifier','Noise Figure using GMRT link with
amplifier',-1);
title('Variation of Noise Figure with Optical Loss');
grid on;

figure(4);

plot(alphaDFB,NF_linkDFB,'b',lossGMRT,NF_linkGMRT,'k');
xlabel('Optical Loss(dB) -->');
ylabel('Noise Figure (dB) -->');
legend('Noise Figure using DFB Uncooled Laser without Pre-amplifier','Noise Figure using GMRT link
without Post-amplifier',-1);
title('Variation of Noise Figure with Optical Loss');
grid on;
```

```
figure(5);

plot(alphaDFB,P_totalDFB,'b',lossGMRT,P_totalGMRT,'k');
xlabel('Optical Loss(dB) -->');
ylabel('Noise Power (dBm/Hz) -->');
legend('Total Noise in DFB Uncooled Laser', 'Total Noise in GMRT',-1);
title('Variation of total Noise Power with Optical Loss');
grid on;

figure(6);

plot(alphaDFB,SNR_totalDFB,'b',lossGMRT,SNR_totalGMRT,'k');
xlabel('Optical Loss(dB) -->');
ylabel('SNR (dB/Hz) -->');
legend('SNR in DFB Uncooled Laser', 'SNR in GMRT',-1);
title('Variation of SNR with Optical Loss');
grid on;

figure(7);

plot(alphaDFB,SFDR_DFB,'b',lossGMRT,SFDR_GMRT,'k');
xlabel('Optical Loss(dB) -->');
ylabel('SFDR (dB/Hz) -->');
legend('SFDR in DFB Uncooled Laser', 'SFDR in GMRT',-1);
title('Variation of Spurious Free Dynamic Range with Optical Loss');
grid on;
```

Appendix B

MATLAB Program to determine the RF Parameters of the link using DFB-Uncooled Laser

B.1. Program to determine the bias and Optical Power of the transceiver using DFB-Uncooled Laser for increasing temperatures:

```
temp=linspace(9,31,23);
bias1 = [1.865 1.868 1.873 1.856 1.878 1.894 1.895 1.927 1.927 1.953 1.966 1.989 1.991 2.001 2.016
2.025 2.017 2.023 2.061 2.05 2.094 2.088 2.115 ];
pwr1 = [4.7 4.8 4.8 4.8 4.8 4.8 4.8 4.9 4.9 4.9 4.9 4.9 4.9 4.9 4.9 4.9 4.9 4.9 4.9 4.9 4.9 4.9 4.9 ];
bias2 = [1.781 1.78 1.785 1.789 1.808 1.823 1.842 1.851 1.870 1.891 1.903 1.916 1.930 1.94 1.95 1.954
1.96 1.982 1.991 2.018 2.033 2.056 2.09 ];
pwr2 = [4.7 4.6 4.6 4.6 4.6 4.6 4.6 4.6 4.6 4.6 4.6 4.6 4.6 4.6 4.6 4.6 4.6 4.6 4.6 4.6 4.6 4.5 4.5 ];
cur1=bias1./33;
cur2=bias2./33;
curr1=1000.*cur1;
curr2=1000.*cur2;

figure(1);

subplot(1,2,1);
plot(temp,curr1);
xlabel('Temperature (Celcius) -->');
ylabel('Current (mA)  -->');
axis([9 33 50 70]);

subplot(1,2,2);
plot(temp,pwr1,'k');
xlabel('Temperature (Celcius) -->');
ylabel('Power (dBm)  -->');
axis([9 33 4 5.5]);
title(' Temperature Stability of First Transmitter');

figure(2);

subplot(1,2,1);
plot(temp,curr2);
xlabel('Temperature (Celcius) -->');
ylabel('Current (mA)  -->');
axis([9 33 50 70]);

subplot(1,2,2);
plot(temp,pwr2,'k');
xlabel('Temperature (Celcius) -->');
ylabel('Power (dBm)  -->');
axis([9 33 4 5.5]);

title(' Temperature Stability of Second Transmitter' ) ;
```

B.2. Program to determine the bias and Optical Power of the transceiver using DFB-Uncooled Laser for decreasing temperatures:

```
temp=linspace(5,32,28);
bias1 = [1.843 1.86 1.855 1.901 1.877 1.926 1.912 1.964 1.965 1.993 1.998 2.028 2.049 2.064 2.095 2.101
2.095 2.116 2.117 2.116 2.114 2.113 2.113 2.112 2.111 2.11 2.109 2.109];
pwr1 = [4.7 4.9 4.9 4.9 4.9 4.9 4.9 4.9 4.9 4.9 4.9 4.9 4.9 4.9 4.9 4.9 4.9 4.9 4.9 4.9 4.8 4.8 4.8 4.7 4.7
4.7 4.6];
bias2 = [1.75 1.78 1.79 1.813 1.835 1.847 1.862 1.887 1.901 1.911 1.936 1.949 1.958 1.98 1.995 2.023
2.033 2.049 2.064 2.092 2.077 2.092 2.091 2.09 2.088 2.087 2.087 2.081];
pwr2 = [4.7 4.7 4.6 4.6 4.6 4.6 4.6 4.6 4.6 4.6 4.6 4.6 4.6 4.6 4.6 4.6 4.6 4.6 4.6 4.5 4.5 4.5 4.4 4.4 4.3 4.2 4.2
4.2 4.1];
cur1=bias1./33;
cur2=bias2./33;
curr1=1000.*cur1;
curr2=1000.*cur2;

figure(1);

subplot(1,2,1);
plot(temp,curr1);
xlabel('Temperature (Celcius) -->');
ylabel('Current (mA) -->');
title(' Temperature Stability of First Transmitter');
axis([0 40 50 70]);

subplot(1,2,2);
plot(temp,pwr1);
xlabel('Temperature (Celcius) -->');
ylabel('Power (dBm) -->');
axis([0 40 4.5 5]);

figure(2);

subplot(1,2,1);
plot(temp,curr2);
xlabel('Temperature (Celcius) -->');
ylabel('Current (mA) -->');
title(' Temperature Stability of Second Transmitter');
axis([0 40 50 70]);

subplot(1,2,2);
plot(temp,pwr2);
xlabel('Temperature (Celcius) -->');
ylabel('Power (dBm) -->');
axis([0 40 4 5]);
```

B.3. Program to determine the VSWR of the transceiver using DFB-Uncooled Laser:

```
frequency = [ 10 20 30 40 50 60 70 80 90 100 150 200 250 300 350 400 450 500 550 600 650 700 750 800
850 900 950 1000];
S11 = [ -9.9 -16.2 -20.66 -24.66 -28.77 -33.42 -36.36 -33.8 -30.43 -27.87 -21.41 -18.21 -16.05 -14.11 -12.66
-11.21 -10.16 -9.04 -7.93 -6.83 -6 -5.48 -4.4 -3.9 -3.89 -4.51 -5.8 -7.77];
conversion_loss = [ -37.42 -36.83 -36.92 -36.92 -36.91 -36.94 -36.95 -36.95 -36.96 -36.95 -37 -36.95 -37.04
-37 -36.85 -36.77 -36.45 -36.43 -36.04 -35.68 -35.5 -35.28 -35 -34.24 -34.19 -34.96 -35.88 -38.03];

figure(1);
plot(frequency,S11,'b',frequency,conversion_loss,'k');
xlabel('Frequency (MHz) -->');
ylabel('Amplitude (dB) -->');
title('Network Analyzer Data showing Return Loss and Conversion Loss');
legend('S11','S21', -1);

return_loss=S11;
ret_loss=10.^(return_loss/10);
figure(2);
plot(frequency,ret_loss);
xlabel('Frequency (MHz) -->');
ylabel('Return Loss -->');
title('Variation of Return Loss with Frequency');

vswr=(1+ret_loss)./(1-ret_loss);
figure(3);
plot(frequency,vswr);
xlabel('Frequency (MHz) -->');
ylabel('VSWR -->');
title('Variation of VSWR with Frequency');

vswrdB=10.*log10(vswr);
figure(4);
plot(frequency,vswrdB);
xlabel('Frequency (MHz) -->');
ylabel('VSWR (dB) -->');
title('Variation of VSWR in dB with Frequency');

figure(5);
plot(frequency,conversion_loss);
xlabel('Frequency (MHz) -->');
ylabel('Conversion Loss (dB) -->');
title('Network Analyzer Data showing Conversion Loss');
```

B.4. Program to determine the 1-dB Compression Point of the link using DFB-Uncooled Laser:

```
inp_pwr= [-10 -9 -8 -7 -6 -5 -4 -3 -2 -1 0 1 2 3 4 5 6 7 8 9 10 11 12 13 14 15 16 17 18 19 20 21 ];
out_pwr= [-46.85 -45.88 -44.89 -43.90 -42.93 -41.55 -40.56 -39.56 -38.56 -37.57 -36.57 -35.56 -34.56 -
33.57 -32.58 -31.6 -30.6 -29.6 -28.6 -27.6 -26.6 -25.6 -24.56 -23.54 -22.52 -21.48 -20.44 -19.50 -18.57 -
17.86 -17.30 -17.02 ];
inppwr=linspace(18,30,13);
outexpt=linspace(-18.6,-6.6,13);
ip=linspace(21,30,10);
outpwr=[-17 -16.8 -16.7 -16.65 -16.52 -16.4 -16.3 -16.25 -16.25 -16.25];

figure (1);
plot(inp_pwr,out_pwr,'b',inppwr,outexpt,'b--',ip,outpwr,'b');
xlabel('Input RF Power (dBm) -->');
ylabel('Output RF Power (dBm) -->');
title('Determination of 1-dB Compression Point by variation of Input RF Power');
grid on;
text(0,-15,'Input 1-dB Compression Point = 21 dBm');
```

B.5. Program to determine the Third-Order Intercept Point of the link using DFB-Uncooled Laser:

```
inp_pwr = [1 1.5 2 2.5 3 3.5 4 4.5 5 ];
fund_pwr = [-41.42 -40.87 -40.37 -39.83 -39.36 -38.77 -38.31 -37.76 -37.19 ];
imd_pwr = [-94.9 -94.4 -93.9 -92 -90.9 -89.5 -88.6 -87.3 -85.7 ];

inppwr = linspace(5,35,31);
extimd_pwr = [-85.7 -82.7 -79.7 -76.7 -73.7 -70.7 -67.7 -64.7 -61.7 -58.7 -55.7 -52.7 -49.7 -46.7 -43.7 -40.7 -
37.7 -34.7 -31.7 -28.7 -25.7 -22.7 -19.7 -16.7 -13.7 -10.7 -7.7 -4.7 -1.7 1.3 4.3 ];
fundpwr = linspace (-37.2,-5.2,31);

figure(1);
plot(inp_pwr,fund_pwr,'b',inppwr,fundpwr,'b--',inp_pwr,imd_pwr,'k',inppwr,extimd_pwr,'k--');

axis([-2 40 -100 5]);
grid on;
xlabel('Input Power (dBm) -->');
ylabel('Output Power (dBm) -->');
legend('Fundamental Power (Measured)','Fundamental Power (Expecteded)','Intermodulated Power
(Measured)','Intermodulated Power (Expected)',-1);
title('Plot determining IP3 Point');
text(0,-10,'Input IP3 Point = 30.1 dBm');
```

B.6. Program to determine the variation of the SNR of the link with Input Optical Power using DFB-Uncooled Laser:

```
opt_pwr=linspace(-18,4,23);
SNR=[53.1 55 56.2 58 61 62.7 64.6 66.5 68.6 71.1 73 75 77.1 78.8 80.5 82.8 84.8 86.6 88.4 90.5 92 94.3
96];

figure(1);
plot(opt_pwr,SNR);
xlabel('Input Optical Power (dBm)-->');
ylabel('Signal-to-Noise Ratio per Hz(dB/Hz) -->');
title('Variation of SNR per Hertz with Optical Power');
text(-15,90,'RF Power=0 dBm (Constant)');
grid on;
```

B.7. Program to compare the variation of the SNR of the link with Input Optical Power using DFB-Uncooled Laser:

```
inp_pwr=linspace(-18,4,23);
conv_loss=-37;
i_p=-(2.*inp_pwr);
sig=conv_loss+i_p;
SNR=-sig;
SNR_Hz=[53.1 55 56.2 58 61 62.7 64.6 66.5 68.6 71.1 73 75 77.1 78.8 80.5 82.8 84.8 86.6 88.4 90.5 92
94.3 96];
SNR_Th=SNR+50;

figure(1);
plot(inp_pwr,SNR_Th,'b',inp_pwr,SNR_Hz,'k');
xlabel('Input Power (dBm) -->');
ylabel('SNR per Hertz (dB/Hz) -->');
legend('Theoretical','Experimental',-1);
title('Variation of SNR with Input Optical Power');
grid on;

loss=4.5-inp_pwr;

figure(2);
plot(loss,SNR_Th,'b',loss,SNR_Hz,'k');
xlabel('Optical Loss (dB) -->');
ylabel('SNR per Hertz (dB/Hz) -->');
legend('Theoretical','Experimental',-1);
title('Variation of SNR with Optical Loss');
grid on;
```